May 2015

Flux-tunable superconducting transmons for quantum information processing

Matthew Ware
Syracuse University

Recommended Citation

Ware, Matthew, "Flux-tunable superconducting transmons for quantum information processing" (2015). *Dissertations - ALL*. 249.
https://surface.syr.edu/etd/249

Abstract

In this dissertation, I describe a series of experiments using flux-tunable transmon qubits for quantum information processing. These qubits are designed with different levels of Josephson junction asymmetry. The first two chapters of this dissertation will introduce the reader to superconducting qubits and circuit quantum electrodynamics. I will present experiments using the cQED architecture to implement fast photon swapping between an asymmetric qubit and a superconducting resonator using flux-driven sidebands. This is the first experimental observation of flux-driven sidebands in a superconducting system. This process also allows photon swaps between qubit and resonator to first order in the qubit-resonator coupling strength. I will detail an experiment to study and optimize an all-microwave two-qubit gate using the cross-resonance effect. This work constitutes the first experimental study of the cross-resonance effect vs. frequency and confirms effects from the higher energy levels of the transmon in the effective coupling during a cross-resonant drive. Lastly, I will outline a theoretical analysis and initial experiments to study the coherence properties of asymmetric transmons.

Flux-tunable superconducting transmons for quantum information processing

by

Matthew Elliott Ware

B.S., University of Alabama 2009

Submitted to the Department of Physics
in partial fulfillment of the requirements for the degree of

Doctor of Philosophy in Physics

at

SYRACUSE UNIVERSITY

May 2015

Acknowledgments

I would like to foremost thank my advisor Prof. Britton Plourde who helped guide me through tumultuous waters of graduate school and patiently answered any question I had about physics. He also tirlessly read and re-read this dissertation offering corrections and revisions from very early stages. I would also like to thank my fellow graduate student Michael DeFeo and post-docs Joel Strand, Bo Xia, Pradeep Bhupathi, Matthew Hutchings and Daniela Bogorin for showing me how to do everything in the lab.

To my family and friends, without you this dissertation would not have been possible. William and Donna Ware, thank you for giving the best opportunities you could and encouraging me to pursue my interests.

A major thank you is due my collaborators at Raytheon-BBN Technologies Tom Ohki, Blake Johnson and Colm Ryan. These guys are amazing and provided extensive material and technical expertise to several sections of this dissertation.

Acknowledgements could not be complete without Steve Jones for an amazing amount of fabrication guidance and assistance. It will be my task to pass on the dark arts of nano-fabrication to the next generation. Good luck at Google, Steve!

A large sum of my early days in graduate school were spent in the machine shop where I tried to learn as much as possible from Phil Arnold, Charlie Brown, Lou Buda and Lester Shmutzler. It was from these craftsman that I learned the equally dark arts of fly cutting, the lathe, and advanced endmill techniques. When people ask if I learned anything useful durning my PhD, I will probably think of these first.

I would also like to thank the open source community who have shared their work with the world so we can all stand on their giant shoulders. This dissertation and the data collected within would never have existed without their contribution. Portions of this dissertation were construed using open sourced templates from MIT [3] and Lev Bishop [14]. They have my eternal gratitude.

Last but not least I would like to thank my girlfriend, Gillian Herbert, who suffered the most during the writing of this dissertation.

Contents

List of Figures

List of Tables

Chapter 1

Introduction

From its beginnings in the early 1900s, quantum mechanics has proven to be one of the most experimentally successful theories of all time. The predictive power of quantum mechanics covers a broad range of system energies and scales. Its effect on experimental physics is possibly more noticeable today than in the golden age of nearly a century ago thanks in part to the advance of experimental techniques. An exciting new set of tools, developed in the last ten or fifteen years, has allowed physicists to probe some of the more basic properties of quantum mechanics. Starting in the 1990s scientists began experimentally studying the interactions between atoms and photon modes inside optical cavities. Termed cavity quantum electrodynamics (CQED), these systems highlight the basic interactions of light with matter [41]. In 2012, Serge Haroche and David Wineland shared the Nobel Prize in Physics for their work on CQED creating Schrödinger photon cat states and providing the first time-resolved look at the decoherence process in a quantum system [83, 20, 36]. Building on ground-breaking experiments with atoms in cavities, there has been a renaissance in translating these atomic systems into macroscopic devices on a chip. These devices are made of many billions of atoms yet still exhibit quantum behavior. This "quantumness" is not only manifested in the microscopic degrees of freedom, but also in collective low-dimensional and experimentally observable quantities of the circuit.

Measurement of these quantum effects is now possible thanks to a coalescing of technology from a variety of fields including superconductivity, microwave engineering, computer science, information theory, silicon processing and quantum foundations. This direct descendant of CQED is called circuit quantum electrodynamics (cQED) and makes it possible to explore parts of parameter space not accessible using naturally occurring quantum systems [124]. Using existing thin-film processing and low-temperature measurement techniques, these "quantum optics on a chip" systems have achieved amazing experimental results including synthesizing arbitrary quantum states in a resonator [54], cooling a mechanical resonator to its quantum mechanical ground state [91] and allowed tracking of individual quantum trajectories [86, 127] using a weak measurement framework [64].

In the experiments listed above, the role of the atom in CQED was replaced with a superconducting qubit. This qubit functions as a two-level system, the same way valence electron states in an excited atom form a two-level system in CQED. A critical component of these cQED qubits is the Josephson junction, which will be described in Chapter 2. It provides a nonlinear element that makes the qubit energy level spacing anharmonic and allows individual states to be addressed. The quantum coherent properties of the Josephson junction were observed in the early 1980s [75, 76] and have become an important part of a variety of superconducting devices including qubits. The first experiments with superconducting qubits were done in the early 2000s [78, 23, 88]. In the intervening years, these quantum machines have evolved into an exciting testbed for observing quantum behavior in electrical circuits.

In the field of computation, these qubits are the basic building blocks for a quantum computer. Like a classical bit, a qubit has two states, 0 and 1, but unlike a classical bit, it can be in an arbitrary superposition of these two states $\alpha|0\rangle + \beta|1\rangle$. A quantum computer can use this superposition principle to speed up certain key algorithms. One of the most well known quantum algorithms is Lov Grover's algorithm [48] for searching an unsorted list. This algorithm provides a square root speed up for searching compared to classical algorithms. Peter Shor's factoring algorithm [115] for factoring an n-bit integer runs exponentially faster than the best known classical algorithm, the general field number-sieve. To date, only modest implementations of these have been achieved [120] on a quantum computer, though rapid progress is being made. While these particular algorithms might not seem all that interesting, they were some of the first glimpses that quantum computers might have computing power beyond that of classical computers. Additionally, most modern public-key cryptography is based on the fact that multiplication and discrete log are computationally easy but the inverse operations are computationally hard. A quantum computer could then pose a threat to modern cryptographic systems [104].

On top of these specific uses, a quantum computer could be used to simulate quantum systems providing a new tool for researchers in biology and physical chemistry. A working quantum computer would also have consequences for some of the foundational aspects of quantum mechanics, though none of these topics will be explored here. In this work we will study in detail the superconducting transmon qubit and a slight variant called the asymmetric transmon. In particular, we will look at how the flux degree of freedom can be used in a few cases to engineer interactions, explore qubit parameter space, and possibly reduce the susceptibility of these qubits to flux noise.

1.1 Thesis outline

This dissertation will document the study and exploration of two separate types of interactions in superconducting systems. In preparation for this I will review some of the basic ideas of circuit quantum electrodynamics (cQED) in Chapter 2. I will also introduce the superconducting qubit inside the cQED framework. In particular, I will focus on the transmon-type qubit which is currently a promising type of qubit for quantum information processing. In addition, the Jaynes-Cummings Hamiltonian will be described, as it nicely captures the coupling of a superconducting qubit and an electromagnetic cavity. A quick review of qubit gates and measurement can be found at the end of the chapter, and a section on time domain measurements is included for the interested reader.

Chapter 3 will introduce sideband interactions in superconducting qubits induced via an ac flux drive. This type of parametric interaction allows real photon swaps between a qubit and cavity at rates up to 85 MHz. This is significantly faster than a more traditional voltage drive. I'll explain how a fast two-qubit CNOT gate can be constructed using this type of interaction.

In Chapter 4, I describe a systematic study of the cross resonance two-qubit effect vs. qubit-qubit detuning Δ. The cross resonance (CR) effect can be turned on by driving one qubit at another qubit's frequency where the two are coupled together by a common superconducting cavity. I'll show some recent results using a flux-tunable transmon qubit to vary this detuning and test a theory of the CR interaction strength J_{eff} including the effects of qubit energy levels outside the computation subspace $\{|0\rangle, |1\rangle\}$.

Chapter 5 will present a brief analysis of *asymmetric* transmons made with two Josephson junctions with different critical currents. This has the effect of removing a divergence and flattening out the frequency modulation curves vs. flux. In theory, this could lead to a reduced sensitivity to magnetic flux noise for this type of qubit. I'll present plans for a study of coherence times vs. the degree of junction asymmetry with an end goal of highlighting the tradeoff between flux tunability and reduced magnetic flux noise. This type of transmon could work well in systems that need some degree of tunability but not as much as a traditional, symmetric transmon.

Chapter 2

Circuit Quantum Electrodynamics

The theoretical framework for this dissertation is termed circuit quantum electrodynamics (cQED). The foundations of it are grounded in the basic interactions between light and matter. This is the realm of atomic physics. The predecessor to cQED is called cavity QED and entails just that: a single atoms interacting with a confined electromagnetic field. Here I will outline some basics of cavity QED and how it directly relates to the circuit analog. Superconductivity will also so be presented as it applies to superconducting resonators and devices. An important part of many superconducting devices is the Josephson junction that forms an important nonlinear inductive element. Artificial atoms can be made out of circuit elements and their time-domain dynamics characterized. Finally, how these artificial atoms can be used for quantum information processing will be outlined quickly.

2.1 QED with cavities

Quantum electrodynamics (QED) is the study of fundamental interactions between atoms and photons of electromagnetic (EM) radiation [41, 40]. Typically the interactions between atoms and photons are relatively weak, as they are not strongly coupled to each other in free space. The situation changes, though, if the EM field is confined to a small space, such as a high finesse cavity. This is a key concept of cavity QED:

increase the coupling by confining the EM field to a small mode volume in which the atom is located. The quality of a cavity is quantified by the ratio of its resonant frequency ω_0 and the FWHM κ of the peak in frequency space:

$$Q = \frac{\omega_0}{\kappa}. \tag{2.1}$$

If the cavity were made of two mirrors in vacuum, this quality factor Q would quantify how reflective those mirrors are and the sparseness of decay channels for the photon(s) to escape the cavity. The peak width κ, quantifies the number of times a photon will bounce back and forth between the mirrors before escaping the cavity. In optical systems this quantity is called the cavity finesse. A larger κ means a broader resonance peak. Thus, a low κ, high Q cavity increases the strength of photon interactions with an atom having a resonant transition inside the cavity by confining the photon for a relatively long amount of time compared with free space.

In practical experiments, the atom is a highly excited Rydberg atom that can be effectively modeled as a two-level system composed by its valance electron energy and angular momentum states. Such an atom has a large electric dipole d that couples it to the field mode. Electronic transitions in these Rydberg atoms are typically on the order of hundreds of GHz, which matches supported microwave frequency modes [52]. Pioneering work in this field has been by completed by several groups around the world. The Nobel Prize in 2012 was awarded to Serge Haroche and David Wineland for their work using these systems to study the fundamental quantum nature of both light and the two-level systems confined in high-Q cavities [82, 83, 20, 36]. Strange as it may seem, this atom-cavity system maps directly onto superconducting circuits on a two-dimensional chip.

2.2 Superconductivity

The phenomenon of superconductivity was discovered by H. Kamerlingh Onnes in 1911 [118] and has remained an active area of research ever since. For superconducting qubits, a thorough understanding of superconductivity is necessary to design and build them. Several properties are of immediate importance, including the loss of electrical resistance, flux quantization, and the Josephson effect. Though all superconductors have a characteristic loss of electrical resistance at a critical temperature T_c, there is a wide variety of materials and types of superconductors. For most of our purposes we can restrict ourselves to conventional elemental superconducting thin films. These metals have a transition temperature T_c, a screening of magnetic fields from the bulk called the Meissner effect, and microscopic dynamics that are well described by BCS theory [7]. BCS theory was developed in 1957 by Bardeen, Cooper and Schrieffer and it successfully captures the microscopic dynamics of superconductivity. It describes the process at T_c where a phonon-mediated attractive force between the conduction electrons causes the Fermi sea to become unstable. This interaction allows a lower energy bound state between two electrons of opposite spin to form with a characteristic energy 2Δ around the Fermi surface, called the superconducting gap. This gap is an individual material property of metals used in this dissertation and directly related to the critical temperature by

$$2\Delta = 3.5 k_B T_c. \tag{2.2}$$

This pair of bound electrons, called a Cooper pair, now obeys Bose statistics. Well below the transition temperature T_c, all the conduction electrons have formed Cooper pairs and are condensed into a single, macroscopic ground-state wave function with long range coherence. The wavefunction of this ground state is no longer localized

Metal	T_c (K)	$2\Delta(0)(meV)$
Niobium	9.3	3.05
Aluminum	1.18	0.34
Niobium Nitride	15.7	4.6

Table 2.1: Properties of superconducting metals Superconducting metals used in this dissertation as well as other common thin-film superconductors [65].

and spreads throughout the superconductor. It can be written as

$$\Psi(\mathbf{r}, t) = |\Psi(\mathbf{r}, t)|e^{-i\phi(\mathbf{r},t)}, \tag{2.3}$$

highlighting the superconducting phase, which will be important later in the context of the Josephson junction. This phase varies continuously over the extent of the superconductor. The density of Cooper pairs is given by $n_s = |\Psi(\mathbf{r})|^2$. A table of commonly used superconductors is given in Table 2.1. Most of these materials can be easily deposited and etched using standard semiconducting processing techniques.

Despite the vanishing of dc electrical resistance below T_c, superconductors can experience loss and dissipation at microwave frequency drives. The superconductor can have material defects on its surface or in the bulk of the material. The breaking of Cooper pairs is another common loss channel observed in these systems. For $T \ll T_c$, the density of unpaired conduction electrons falls off exponentially with temperature T. Therefore, at temperatures well below T_c, the density of these single electrons, called quasiparticles in a superconducting context, should be exponentially small. One must take care though to properly shield a sample from radiation of energy $E_g(0) > 2\Delta(0)$ that can break Cooper pairs. This process is actually how superconducting photodetectors work. Experimental work is ongoing in our lab [90] to engineer systems that induce quasiparticle recombination and lower their density inside the superconductor. These loss mechanisms are important to identify and minimize when making qubit systems [80].

Clearly, superconducting materials can be used for a variety of other devices besides qubits. Superconducting photon counters [79], rapid single flux quanta (RSFQ) classical digital computation [53], and high T_c power transmission lines are just a few of the other practical uses of superconductors. The RSFQ approach to classical computation has gained attention over the last several years as way to use Josephson junctions and superconducting loops to push the speed of computation close to ~ 300 GHz and with ultra-fast interconnects [19].

2.2.1 Josephson junctions

A critical part of any superconducting qubit is the Josephson junction [60]. Junctions can be formed by small insulating barriers (on the order of 1 nm thick) between superconducting electrodes (SIS junction), normal metal barriers between superconducting electrodes (SNS), or small constrictions of continuous superconductor (SsS) [118, 70, 38]. The most common type of junction used for making qubits is the SIS-type junction. The constriction-style junction can be challenging to fabricate, while normal-metal-style junctions tend to be lossy for qubits due to dissipation in the normal metal layer.

The defining feature of a Josephson junction is the ability of Cooper pairs to tunnel coherently through the junction without dissipation. Additionally, the zero-voltage relation between the Cooper pair current flowing through the junction and the superconducting phase difference between the superconductors on either side of the junction is given by [118]

$$I = I_0 \sin(\phi_1 - \phi_2), \tag{2.4}$$

where I_0 is the maximum current the junction can support and still maintain zero voltage across its leads; $\phi_{1,2}$ are the phases of the superconductor on either side of the junction. The value of I_0 is set by the superconducting gap of the material and the normal (non-superconducting) state resistance of the junction [118]. The I_0 of

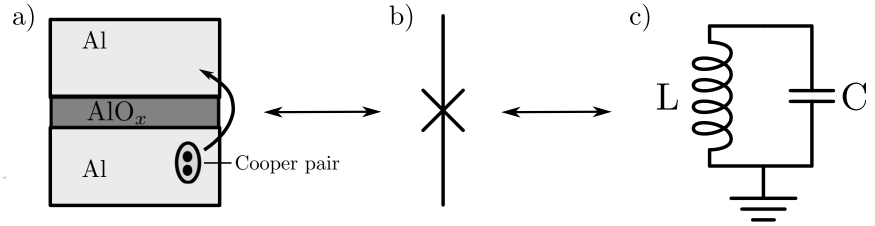

Figure 2-1: Qubit Effective Circuit. Diagram of an $Al/AlO_x/Al$ Josephson junction. **(a)** depicts the AlO_x barrier through which the Cooper pairs tunnel. **(b)** the circuit symbol for a Josephson junction indicated by an X through a superconducting lead. **(c)** the effective circuit of a junction with lumped element components representing its self-capacitance and effective inductance. The junction is non-linear and depends on the amount of current flowing through it. Figure adapted from [31].

a Josephson junction can be measured at room temperature using the Ambegaokar-Baratoff formula [5]

$$I_0 R_n = \pi\Delta(0)/2e, \tag{2.5}$$

where R_n is the measured normal-state resistance of the junction and Δ_0 is the value of the superconducting gap at $T = 0$. These properties are really quite remarkable. The fact that Cooper pairs are able to coherently tunnel through this barrier without dissipation is not at all obvious. This Josephson junction circuit element will be the critical, non-linear element that allows these system to be used as qubits. An SEM micrograph of a Josephson junction fabricated in our lab is shown in Figure 2-2. If the current through the junction exceeds the critical current I_0, a non-zero voltage develops across the junction. This voltage is proportional to the time derivative of the difference in superconducting phase $\delta = \phi_1 - \phi_2$:

$$\frac{\partial\delta}{\partial t} = \frac{2eV}{\hbar} = \frac{2\pi V}{\Phi_0}, \tag{2.6}$$

where Φ_0 is the superconducting flux quantum $\Phi_0 = h/2e \approx 2.07 \times 10^{-15}$ Wb. The Josephson junction will form a non-linear inductor that is critical to qubit anhar-

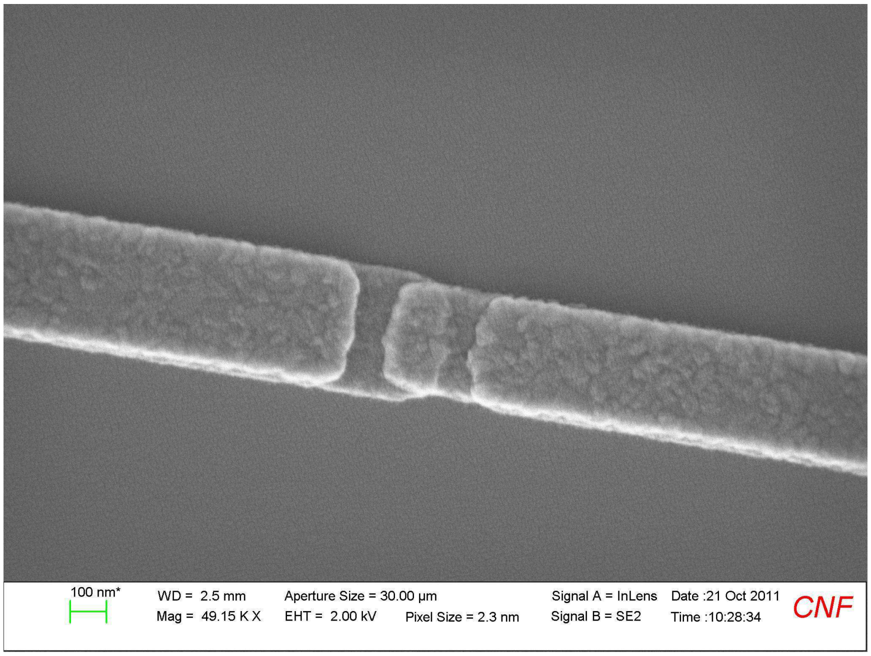

Figure 2-2: Picture of a Josephson junction. An Al-AlxO-Al tunnel junction deposited on a sapphire substrate. This junction in particular is part of a 3D transmon qubit system with a junction area of ∼250 nm x 150 nm. This image was taken at the Cornell Nanoscale Facility (CNF) with a scanning electron microscope.

monicity. The junction inductance can be found using Faraday's law

$$L_J = \frac{V}{\dot{I}}. \tag{2.7}$$

The voltage from Eq. (2.6) can be substituted into Eq. (2.7) along with the derivative of (2.4) to give

$$L_J = \frac{\Phi_0}{2\pi\sqrt{I_B^2 - I_0^2}}, \tag{2.8}$$

where I_B is the current bias through the junction. L_J is called the Josephson inductance and it clearly shows the nonlinearity of the inductance. There is a capacitance associated with a Josephson junction as well. This capacitance could be the junction self-capacitance of the barrier or the junction could be shunted by explicit capacitors. Plugging L_J and this capacitance C into the expression for an LC oscillator $\omega_J(I_B) = (L_J(I_B)C)^{-1/2}$, describes a non-linear oscillator with a frequency that depends on the current flowing through the junction.

The potential energy landscape of a current-biased junction forms a "tilted washboard" of the form [118]

$$U(\delta) = -\frac{\Phi_0 I_0}{2\pi}\left(\cos\delta + \frac{I_B}{I_0}\delta\right), \tag{2.9}$$

for a certain current bias I_B. The state of the junction can be described by the dynamics of a fictitious phase particle of mass $(\hbar/2e)^2 C$ (see Figure 2-3). The prefactor on the cosine term $E_J = \Phi_0 I_0/2\pi$ is called the Josephson energy and sets the barrier height between local minima. While the phase particle is inside one of these local minima, it oscillates at ω_J with zero dc voltage across the junction in this case since the state is localized and $\langle\dot{\delta}\rangle = 0$. As the bias is increased, the phase particle can be thermally activated over the barrier or can tunnel through the barrier, producing a non-zero dc voltage state. For a bias I_0, the minima disappear and the potential only forms inflection points on a downward slope. I_0 denotes the vanishing of local minima and I_c represents the critical current measured in experiments. I_c

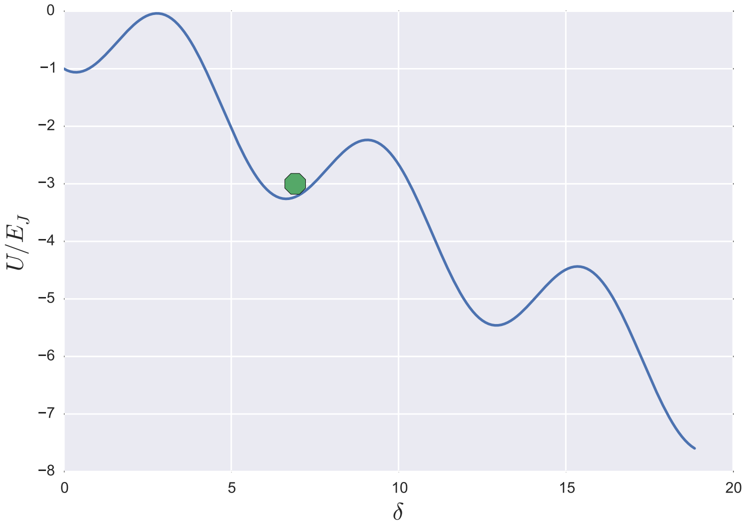

Figure 2-3: Josephson junction potential. The tilted washboard for a current biased-junction. The green dot represents the position of the phase particle, corresponding to the state of the Josephson junction and the blue line is Eq. (2.9). Local minima form at multiples of $\delta = 2\pi$ when $I_B = 0$ and shift when a bias is applied. Data is plotted for $I_B = 0.35 I_0$ and $E_J = (\Phi_0 I_c/2e)$ is the Josephson energy.

will be lower than I_0 due to thermally assisted escape and quantum tunneling. The first measurements of coherent properties in Josephson junctions observed quantum tunneling out to this voltage state [76]. Shortly after, quantization of the energy levels[1] inside the minima were observed [75] and later Rabi oscillations were driven between these quantized levels [78]. These experiments clearly show the quantum nature of a collective macroscopic variable [67] and were important step towards the development of superconducting qubit.

The Josephson junction will allow the construction of quantum two-level systems in superconducting circuits. As described in the next section, these artificial atoms will take the place of actual atoms in cavity QED.

---

[1] These are the energy levels of a phase qubit which consists of the two lowest energy states in one of the potential minima.

2.3 Intro to cQED

In the translation between cavity QED and circuit QED (cQED), the atom will be replaced by an anharmonic oscillator made with Josephson junctions, which forms a quantum two-level system. The cavity will be replaced by a one-dimensional coplanar waveguide (CPW) cavity made with strips of thin superconducting material on a dielectric substrate [15]. In this section I'll work through the properties of this cQED formalism that will be important in the remaining chapters. The quantization of the superconducting cavity will be presented briefly, along with the physics of the coupling between such a cavity and a two-level system. The superconducting qubit will be built using the Josephson junction from the previous section. There are several types of qubits one can make with Josephson junctions, including the phase, flux, and charge qubit. The basic properties of these circuits will be discussed with an emphasis on a variant of the charge qubit, called the transmon, that will be used in the experiments described in this dissertation. With the two important systems, the cavity and the qubit, and their coupling in place the process of measuring the quantum state of these qubits is described. A major portion of the data presented in the remaining chapters will be time-domain measurements that characterize the coherence of the qubit or its interaction with other qubits. As a primer, a detailed section on these types of measurements in superconducting systems is provided. Finally, a discussion of quantum gates and how they are assessed is included at the end of this chapter as a reference for later chapters.

In cQED, the CPW cavities are patterned from thin films of superconductor, typically on the order of ∼100 nm thick. The CPW dimensions are chosen to provide a matching microwave impedance throughout the device and measurement lines. The dimension with the longest length sets the fundamental frequencies. This cavity resonance will depend on several factors, including the total effective capacitance of the resonator, the kinetic and geometric inductance of the superconductor at microwave frequencies and the state of the qubit. Kinetic inductance [81] appears in supercon-

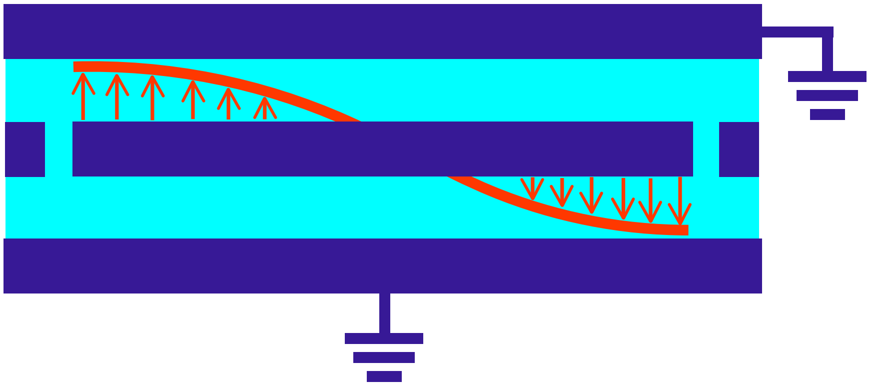

Figure 2-4: Coplanar waveguide resonator. Sketch of a coplanar waveguide. Blue areas represent superconductor and the red lines show the fundamental voltage mode. The center width and separation from ground are chosen to match a characteristic impedance of 50 Ω. The fundamental frequency is set by the length of the resonator along with material parameters and the geometry of the CPW.

ductors as a consequence of the loss of electrical resistance. Without this resistance the electrons in Cooper pairs acquire an appreciable amount of kinetic energy. The inertia of the electron response appears as an additional inductance. Figure 2-4 shows a rough sketch of such a CPW resonator and the mode structure of the fundamental voltage oscillation in the cavity. This configuration drastically reduces the mode volume ($\sim 100\,\text{nm} \times 5\,\mu\text{m} \times 10\,\text{mm}$). This decrease in mode volume is accompanied by an increase in the root-mean-square electric field E_{rms} in the resonator. This increases the strength of the electric field coupling to systems like qubits [15].

The superconducting resonator can be analysed starting from basic circuit principles following the derivation of Devoret [37]. Branch voltages and currents can be defined in terms of fields in the resonator and linked to fluxes and charges in the circuit. Using these variables and Kirchoff's laws as a constraint, the Hamiltonian for any such circuit can be derived. Of particular interest, are CPW resonators and later, Josephson junction devices. In the CPW case, the effective capacitance and inductance per unit length, C_l and L_l shown in Figure 2-5 can be defined. Following

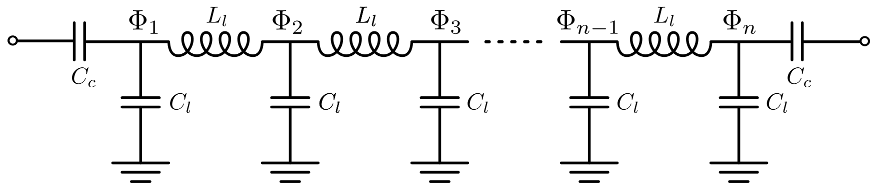

Figure 2-5: Lumped-element LC oscillator. Transmission-line resonator decomposed into lumped-element nodes made of inductors and capacitors. Each node has an effective inductance L_l and capacitance C_l. The ends of the LC chain are capped with coupling capacitors which, allow coupling of ac signals into the resonator. The smaller the C_cs the smaller the coupling to the reset of the circuit.

a standard procedure [37, 16, 111], Φ is defined as the time integral of the voltage

$$\Phi(t) = \int_{-\infty}^{t} V(\tau)\mathrm{d}\tau, \tag{2.10}$$

[37]. This Φ can be related to the potential energy in the capacitive elements $U = (1/2)C_l V^2 = (1/2)C_l\dot{\Phi}^2$ and kinetic energy in the inductive elements $T = (1/2L_l)\Phi^2$ using Faraday's law $V = L_l\dot{I} = \dot{\Phi}$. With these relations, the Lagrangian per unit length can be written as

$$\mathcal{L} = 2C_l\dot{\Phi}^2 - \frac{1}{2L_l}\Phi^2, \tag{2.11}$$

[37]. In this expression, Φ can be viewed as flux stored in the inductive elements, with a conjugate charge Q in the capacitive elements. Neglecting for now the coupling capacitors at the ends and assuming a uniform C_l and L_l, this expression can be integrated over the length of the resonator and the capacitances and inductances per unit length can be replaced with a single L and C. Further, the standard Legendre transform, with $Q = \delta\mathcal{L}/\delta\dot{\Phi} = C\dot{\Phi}$ as the conjugate to Φ [37], can be used to construct a Hamiltonian from the Lagrangian, which gives

$$H = \frac{\hat{Q}^2}{2C} + \frac{\hat{\Phi}^2}{2L}, \tag{2.12}$$

[37]. A Hamiltonian of this form corresponds precisely to the standard harmonic

oscillator. This means we can write H, Q, and Φ as quantum operators $\hat{H}$,$\hat{Q}$, and $\hat{\Phi}$ with the standard commutation relation

$$[\hat{Q}, \hat{\Phi}] = -i\hbar. \tag{2.13}$$

With this expression, we can write the $\hat{H}$ in the standard, dimensionless form

$$\hat{H} = \hbar\omega_r(a^\dagger a + 1/2), \tag{2.14}$$

where $\omega_r = 1/\sqrt{LC}$ and $\{a, a^\dagger\}$ are the traditional raising and lowering operators:

In most cases the zero-point energy of the oscillator will be shifted to remove the 1/2 term when the oscillator is represented in cQED Hamiltonians as

$$H_r = \hbar\omega_r(a^\dagger a). \tag{2.15}$$

This energy is still present in the physical system, but typically doesn't play a role in the dynamics of the system. It should be noted though that the Lamb shift from this zero-point motion can be measured in a cQED system [43]. The voltage inside the resonator can now be written in terms of a and $a^\dagger$

$$V_{LC} = V^0_{rms}(a^\dagger + a), \tag{2.16}$$

with the RMS voltage given by

$$V^0_{rms} = \sqrt{\frac{\hbar\omega_r}{2C}}, \tag{2.17}$$

where C is the total capacitance on the resonator.

2.3.1 QED with superconducting circuits

With the resonator described above, we can now introduce a two-level system with some coupling to the cavity. For this section, we will take the qubit to be a spin-1/2 particle with some energy $\hbar\omega_{ge}$ separating the ground and excited energy states of the system. I will show how this two-level qubit can be built using superconductors and Josephson junctions in the next section. In this context, the traditional Pauli spin operators $\sigma_{\{x,y.z\}}$ apply to the spin. Taking the canonical z-axis as the states on which the energy states lie–this is the same as placing the spin 1/2 particle in a magnetic field pointing the z direction; this implies the ground state is aligned with the field and the excited state is aligned opposed to the field– and setting the zero-energy point halfway between the two states, we can write the qubit Hamiltonian as

$$H_a = \frac{\hbar\omega_{ge}}{2}\sigma_z. \tag{2.18}$$

The standard raising and lowering operators $\sigma_\pm = (1/2)(\sigma_x \pm i\sigma_y)$ also apply.

The dipole moment of the qubit couples to the electric field of the cavity with a coupling strength $g = d\mathcal{E}_{\rm rms}/\hbar$. $\mathcal{E}_{\rm rms}$ can be made quite large in cQED due to the mode volume reduction and the effective d that is larger since the atom is stationary, as opposed to flying through the cavity with some time of flight t in the case of CQED. This is a key difference between cavity QED and cQED. The coupling strength g can be made larger than the photon loss rate from the cavity κ, which allows a cQED system to reach the "strong coupling limit" of QED [51]. This coupling allows the spin and electric field to exchange energy when $\omega_{ge} = \omega_r$, with the expression

$$(a + a^\dagger)\sigma_x = (a + a^\dagger)(\sigma_+ + \sigma_-). \tag{2.19}$$

For drives with frequencies on the order of the cavity resonance or the spin energy difference, the rotating wave approximation is made where terms like $a\sigma_-$ and $a^\dagger\sigma_+$ are ignored [125]. These terms represent a change in the number of excitations in the system and can be neglected in the case $\omega_r + \omega_{ge} \gg g, |\omega_r - \omega_{ge}|$. The two remaining terms are $a\sigma_+$ and $a^\dagger\sigma_-$, where a quantum of energy is swapped back and forth between the qubit and the cavity at a rate g. Combining terms, the Jaynes-Cummings Hamiltonian is defined as

$$H = \hbar\omega_r a^\dagger a + \frac{\hbar\omega_{ge}}{2}\sigma_z + \hbar g(a^\dagger\sigma_- + a\sigma_+), \tag{2.20}$$

[52]. This equation can be diagonalized exactly in the energy eigenbasis yielding eigenenergies

$$E_{\pm,n} = \hbar n\omega_r \pm \frac{\hbar}{2}\sqrt{4ng^2 + \Delta^2}, \tag{2.21}$$

where $\Delta = \omega_r - \omega_{0,1}$ is the qubit-cavity detuning and eigenstates [52]

$$\begin{aligned} \overline{|-, n\rangle} &= \cos\theta_n|g, n\rangle - \sin\theta_n|e, n-1\rangle \\ \overline{|+, n\rangle} &= \sin\theta_n|g, n\rangle + \sin\theta_n|e, n-1\rangle. \end{aligned} \tag{2.22}$$

In this case, the plus and minus signs refer to the qubit ground and excited state respectively. When the qubit system is coupled to the photon modes of the cavity, the eigenstates of the system acquire characteristics of both systems. Therefore, they exhibit both the two-state nature of the qubit and bosonic properties of the cavity photons. The degree of each is set by the mixing angle [111, 16]

$$\theta_n = \frac{1}{2}\arctan\left(\frac{2g\sqrt{n}}{\Delta}\right). \tag{2.23}$$

An avoided level crossing between the qubit and the cavity is plotted in Figure 2-7. In this case, a qubit with a tunable Josephson energy E_J is tuned through the resonance of the cavity. The splitting of the cavity resonance is twice the coupling strength $2g$.

The eigenenergies and eigenstates above represent the resonant case when $\Delta = 0$. In typical quantum information processing experiments, it is advantageous to work in the dispersive limit, where the qubit and cavity are far detuned from each other

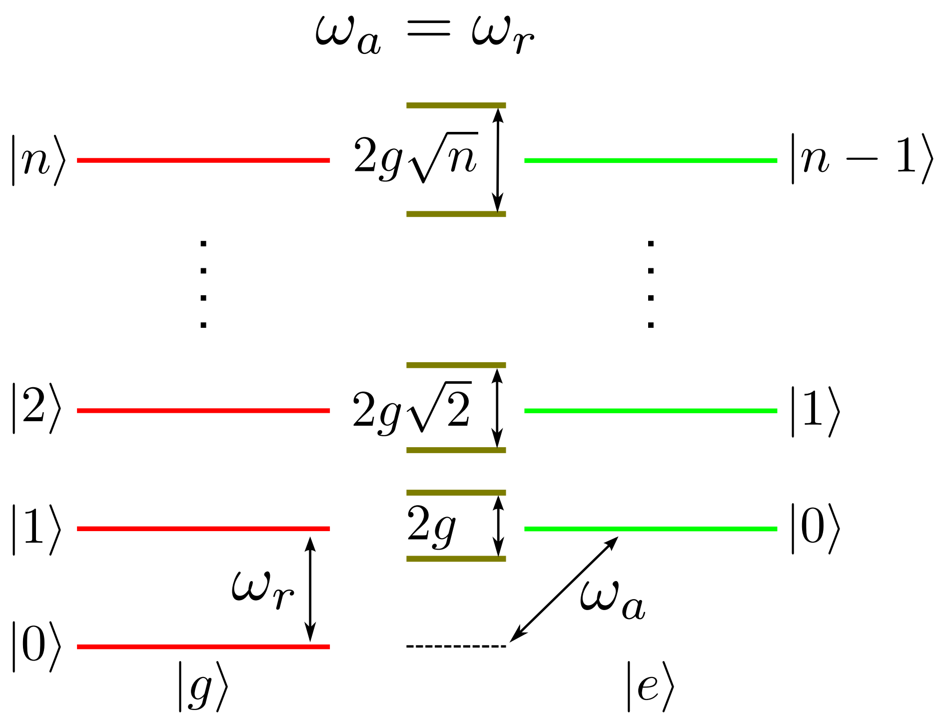

Figure 2-6: The Jaynes-Cummings ladder. An energy level diagram for the Jaynes-Cummings Hamiltonian in the resonant case . $|g\rangle$ and $|e\rangle$ represent the state of the atom or qubit in the computational basis. The number states moving up the y-axis represent photon number states in the cavity. ω_a is the transition frequency of the qubit. Figure reproduced from Fig 1. of [16]

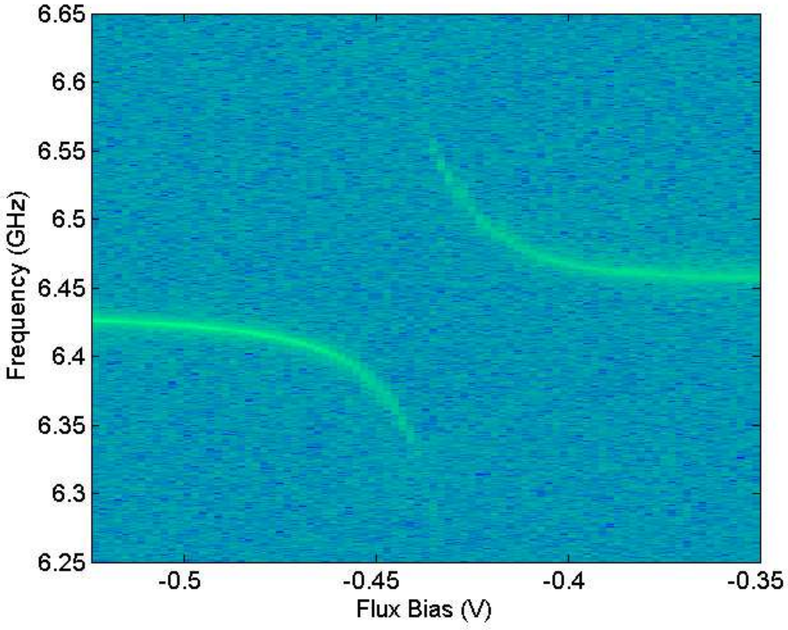

Figure 2-7: Vacuum Rabi splitting of between the qubit and cavity. Density plot showing the qubit frequency ω_{ge} crossing the cavity frequency ω_r. The distance of closest approach is equal to $2g$. This is a convenient way to measure the bare coupling g. This data was measured using a capacitively shunted flux qubit and is.

with $\Delta = |\omega_r - \omega_{ge}|$ and $g \ll \Delta$. In this case the qubit and cavity cannot exchange energy directly. The dynamics in this case become more clear by removing the direct coupling term with the dispersive transformation U given by [16].

$$U = \exp\left[\frac{g}{\Delta}(a^\dagger\sigma_- - a\sigma_+)\right], \tag{2.24}$$

with $\tilde{H} = UHU^\dagger$. Or equivalently, this result can be reached using non-degenerate perturbation theory to expand in powers of the small parameter g/Δ [16]. The transformed Hamiltonian is

$$\tilde{H} \approx \hbar\left[\omega_r + \frac{g^2}{\Delta}\sigma_z\right]a^\dagger a + \frac{\hbar}{2}\left[\omega_{ge} + \frac{g^2}{\Delta}\right]\sigma_z, \tag{2.25}$$

[16] where the qubit and cavity have been shifted by (g^2/Δ) and $(g^2/\Delta)\sigma_z$ respectively.

The eigenenergies are just a Taylor expansion of Eq. (2.21)

$$E_{\pm,n} = \hbar n\omega_r \pm \left(\Delta + \frac{\hbar}{2} n g^2\right), \tag{2.26}$$

which is valid for small $\Delta^2/4g^2$. This defines a critical number of photons that can occupy the cavity and still have the dispersive approximation hold [111]

$$n_{crit} = \frac{\Delta^2}{4g^2}. \tag{2.27}$$

To highlight the effect on the cavity in this regime, we can rearrange terms in (2.25) $\tilde{H} = \hbar(\omega_r + \chi\sigma_z)a^\dagger a + (\hbar\omega_{ge}/2)\sigma_z$ where $\chi = g^2/\Delta$ and the vacuum energy terms were dropped. In this expression, the cavity frequency acquires a shift of $\pm\chi$ dependent on the state of the qubit. This will be discussed more in the context of qubit measurement in Section 2.4.2. Terms could also be arranged to feature the effects on the qubit frequency as photons are added to the cavity through the ac Stark shift, but this will not be a major focus of this dissertation. In most cases the cavity will only be populated with photons to perform a measurement of the qubit state (see Section 2.4.2).

2.4 Superconducting Qubits

The initial implementations of superconducting qubits can be divided into three categories: flux, phase and charge [31, 133]. While all three of these are superconducting circuits and utilize Josephson junctions, they all use different degrees of freedom to form qubits. Another property distinguishing the qubits is the ratio of the relevant energy scales E_J/E_C. E_J is the Josephson energy introduced in the Section 2.2. Again, it is defined as

$$E_J = \frac{\Phi_0 I_0}{2\pi}, \tag{2.28}$$

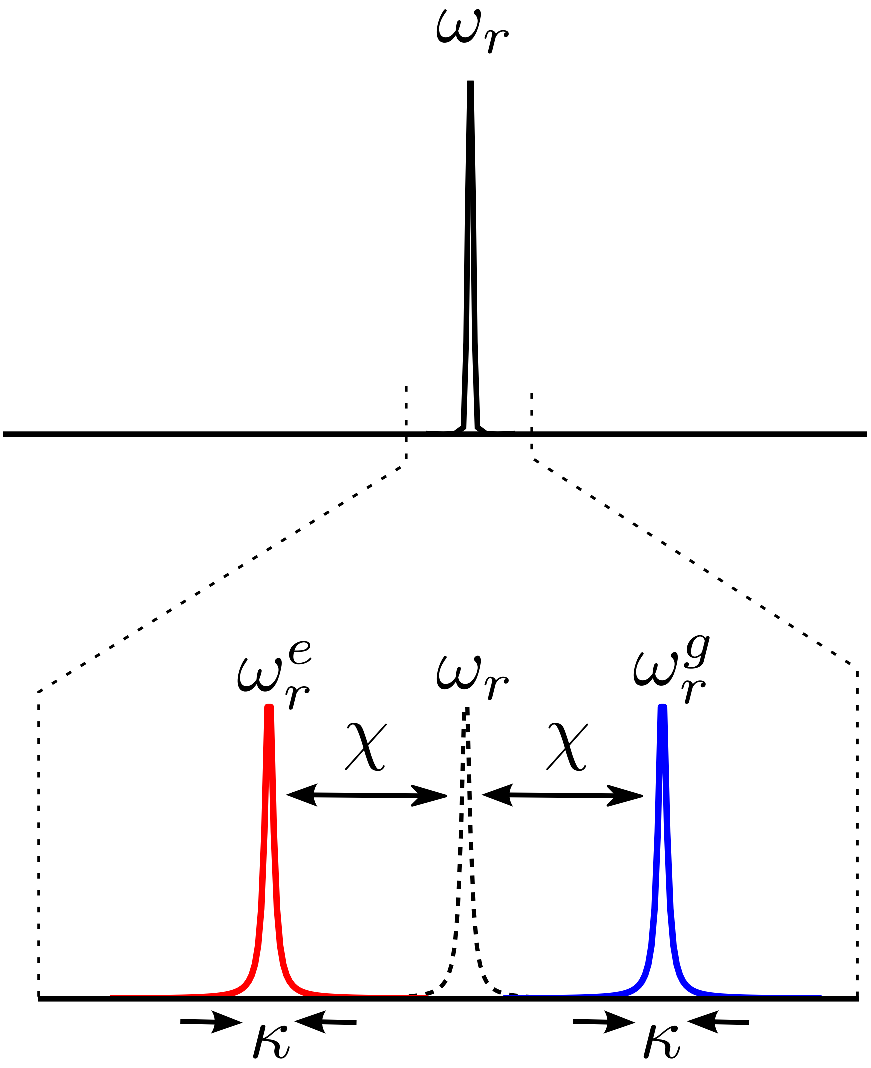

Figure 2-8: Dispersive shift of the cavity. The dispersive shifts the cavity are plotted for the qubit in the ground and excited state. In the dispersive case, the cavity bare resonance ω_r is shifted by $\pm\chi$ depending on the state of the qubit. Figure adapted from Fig 4. of [16] and from [111].

and E_C is the charging energy of the capacitance across the junction, given by

$$E_C = \frac{e^2}{2C_\Sigma}, \tag{2.29}$$

where C_Σ is the total capacitance. The E_C value represents the energy necessary to bring a charge of $2e$ onto one of the qubit electrodes from infinitely far away. The charge qubit operates in the low E_J/E_C regime where the electrostatic charging energy associated with Cooper pairs crossing the junction is large compared to the Josephson energy associated with tunneling through the junction. In this case, the number of Cooper pairs $\hat{n}$ which have tunneled across the junction is the relevant quantum variable [124]. Phase qubits operate with very large E_J/E_C ratios and are essentially current-biased single-junction devices [78]. The computational states of a phase qubit are the two lowest energy levels of a minimum in the Josephson washboard potential shown in Figure 2-3. Finally, the flux qubit operates with an $E_J/E_C \sim 50$ with computational states formed by persistent current states in a ring of superconductor interrupted by one or several Josephson junctions [84].

In this section, I will describe the properties of these qubits. In particular, the charge qubit will be outlined to motivate and put into context the next section on the transmon qubit. This type of qubit has become a popular choice for cQED experiments for a variety of reasons, including improved coherence times compared to its charge qubit ancestor. All qubits presented in this dissertation are transmon-style qubits.

The flux qubit [84, 24] is made of a loop of superconductor interrupted by a Josephson junction. The quantum states in such a system are states of supercurrent flowing clockwise and counterclockwise through the loop. In the case of the flux qubit the superconducting phase $\hat{\phi}$ is well defined and is the relevant quantum variable. Because Cooper pairs can tunnel coherently through the junction and the superconducting wavefunction can interfere with itself, superpositions of the distinct left and right circulating currents can be created with the proper biasing and control pulses. In the case of the flux qubit, the state can be read out by measuring the magnetic flux induced by the current state. This is done by coupling the qubit to a superconducting quantum interference device (SQUID). The SQUID is made of another loop interrupted by two Josephson junction with leads on both sides. With proper biasing, a current pulse can be applied to the SQUID causing it to switch into the finite voltage state with $V = 2\Delta_s/e$ dependent on the state of the qubit [24].

Phase qubits [78] are composed of a current-biased Josephson junction. This bias creates a 'tilted washboard' (see Figure 2-3) profile in the potential energy vs. phase difference across the junction. With a proper bias less than I_0, the state of the system in phase space is such that it remains in a local minimum of the washboard. The low-level states of this local minimum provide the anharmonic state space for the qubit. For readout, a fast current pulse is used to bias the junction close to its critical current I_0 and this tilts the washboard such that the phase particle has a certain probability of tunneling out of the minimum and running down the washboard. Critically, this tunneling probability depends exponentially on the energy state of the qubit. Thus, a qubit in the $|1\rangle$ state is exponentially more likely to tunnel out of the minimum than a qubit in the $|0\rangle$ state when the potential is strongly tilted with a bias current. An escape of the phase particle from the well corresponds to the junction switching into a non-zero voltage state, thus producing a voltage pulse that can be easily measured [78].

Finally, the charge qubit (also called the Cooper pair box) is made of an isolated island of superconductor connected to the superconducting ground of the circuit by two Josephson junctions [88, 18]. The quantum degree of freedom in this circuit is the number $\hat{n}$ of Cooper pairs on the island. The charging energy E_C can be made large compared to $k_B T$ by making the capacitance between the island and all other parts of the circuit small. The charge state of the qubit is traditionally measured using a single-electron transistor (SET). This device is also made of two Josephson junctions and is capacitively coupled to the charge island. A resistance measurement of the

SET is very sensitive to the charge state of the qubit. This resistance can be added in parallel with a resonant circuit and a measurement of its quality factor $Q = f/\Delta f$ is used to infer the quantum state [68, 4]. Charge qubits were also the first type of superconducting qubits measured in a cQED system [15] in several experiments in the Schoelkopf lab at Yale [109, 110, 123]. In this more modern approach, the charge qubit is controlled and measured in a cQED architecture that is identical to the transmon qubit (see section 2.4.1) and the methods discussed in Section 2.4.2.

The charge qubit is hampered by several noise sources that limit its coherence. Charge noise in particular leads to significant dephasing in this type of qubit. The transmon was the product of efforts to make the charge qubit robust against this type of noise.

2.4.1 Transmon qubits

A significant modification of the traditional charge qubit was proposed in Ref. [63] and measured in Ref. [108]. This turned out to be a significant change in course for cQED systems. This transmon qubit boasts several advantages over the original charge qubit. The first and most important difference is an exponentially reduced sensitivity to charge noise with only an algebraic reduction in anharmonicity. This means the qubit will lose its sensitivity to charge fluctuations much faster than its anharmonicity. Another significant difference compared with the charge qubit is the lack of external dc biasing circuitry. Additionally, the typically large capacitors used to fabricate transmons, which push the charging energies E_C lower, allow for large capacitive coupling to transmission lines and therefore easy integration into a cQED architecture. The transmon has become a popular choice for cQED style experiments due to its ease of fabrication and measurement compared to other qubit types. More importantly, the transmon also has excellent coherence properties due to its insensitivity to charge noise.

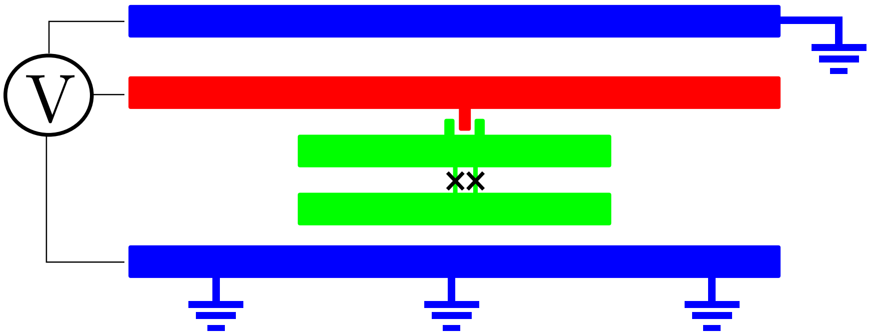

Figure 2-9: Transmon diagram. Sketch of a transmon inside a CPW resonator. The blue strips represent ground relative to the center strip of the resonator. The teal and green blocks form the capacitor making up the transmon with x's marking the locations of the Josephson junctions. Adapted from [63].

The Hamiltonian of the Cooper pair box is given by [63]

$$\hat{H} = 4E_C(\hat{n} - n_g)^2 - E_J \cos\hat{\phi}, \tag{2.30}$$

where n_g is the offset charge produced by an applied gate voltage or environmentally induced charge offset. It is significant to note that the Hamiltonian for the transmon is structurally similar to that of the Cooper-pair box charge qubit. The only difference is the ratio of the energy scales E_J/E_C. The 'transmon regime' is defined by $E_J/E_C \gg 1$. This means the first term in equation (2.30) becomes small compared to the term involving the Josephson coupling energy E_J and the role of the offset charge n_g is reduced (see Figure 2-10). Recall that these energy scales are set by the total qubit capacitance C_Σ and the sum of junction critical currents I_c. In addition, the E_J/E_C ratio can be set and fixed at the time of fabrication by using a single Josephson junction or can be tuned in situ by using two junctions to form a SQUID loop. Traditionally a split junction device is used to allow some tunability and certain types of logic gates, one of which we will discuss further in Chapter 3. In this case, the Josephson energy E_J can be tuned in the same manner as in the charge qubit case in Eq. (2.34).

The eigenenergies of Eq. (2.30) take the form

$$E_m(n_g) = E_C a_{2[n_g+k(m,n_g)]}(-E_J/E_C), \tag{2.31}$$

[63] where m is the relative energy level of the qubit; n_g is again the gate offset charge; $a_\nu(q)$ are the Mathieu characteristic values and $k(m, n_g)$ is a sorting function to arrange the eigenvalues properly for $n_g > 1$. Given these eigenenergies and a definition of the charge dispersion,

$$\begin{aligned} E_m(n_g) &\sim E_m(n_g = 1/4) - \frac{\epsilon_m}{2}\cos(2\pi n_g), \\ \epsilon_m &\equiv E_m(n_g = 1/2) - E_m(n_g = 0), \end{aligned} \tag{2.32}$$

[63] defined as the energy difference between a gate voltage at integer and half-integer values of n_g (see Figure 2-10), the asymptotics of Eq. (2.32) can be found using approximate WKB methods [32]:

$$\epsilon_m \propto \left(\frac{E_J}{2E_C}\right)^{\frac{m}{2}+\frac{3}{4}} e^{-\sqrt{8E_J/E_C}} \tag{2.33}$$

From this it is clear from Eq. (2.32) and Eq. (2.33) that the charge dispersion, defined as the variation in qubit energy splitting with gate charge n_q (Equation (2.32) and Equation (2.33)), in the transmon shrinks exponentially with E_J/E_C ratio for all energy states m. At the same time, the relative anharmonicity defined by the energy difference between successive energy level spacings, shrinks by a weak power law as $\alpha_r \simeq -(8E_J/E_C)^{-1/2}$ [63]. This scaling can be derived from the first order perturbation theory which is outlined below in Eq. (2.37) [63].

For a split-junction transmon with two junctions, the junction term becomes a sum of two terms $H_J = -E_{J1}\cos\phi_1 - E_{J2}\cos\phi_2$. The Josephson energy can now be

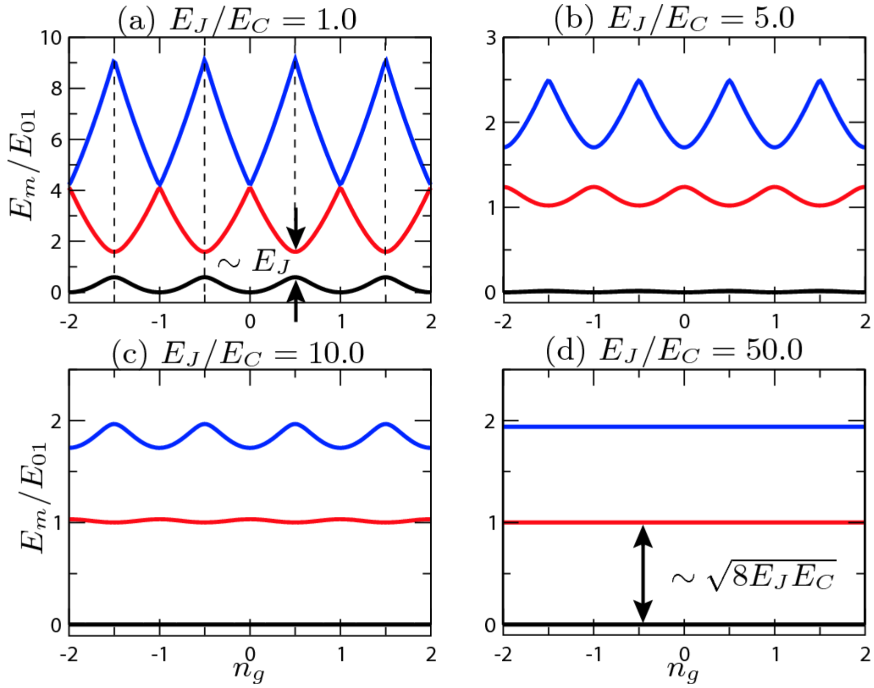

Figure 2-10: Transmon charge dispersion. The reduction in charge dispersion for four different values of E_J/E_C plotted vs. gate charge. $\sqrt{8E_JE_C}$ denotes the resonance frequency of the transmon. Taken from Koch et al. [63].

tuned with external magnetic flux Φ

$$E_J(\Phi) = E_J^{\Sigma}\cos\left(\frac{\pi\Phi}{\Phi_0}\right), \tag{2.34}$$

[63] and E_J^{Σ} is the sum of the two Josephson energies. In Eq. (2.34) it is assumed that $E_{J1} \approx E_{J2}$. This condition defines the *symmetric* transmon case. For arbitrary values of the two Josephson energies, equation (2.34) is modified

$$E_J \rightarrow E_J^{\Sigma}\cos\left(\frac{\pi\Phi}{\Phi_0}\right)\sqrt{1 + d^2\tan^2\left(\frac{\pi\Phi}{\Phi_0}\right)}, \tag{2.35}$$

[63] where $d \simeq \frac{E_{J1}-E_{J2}}{E_{J1}+E_{J2}}$. We refer to a transmon with intentional asymmetry as an asymmetric transmon, and the properties of such a device will be important in Chapter 3 and Chapter 5.

The transmon can also be understood in terms of perturbation theory, viewing the anharmonicity as a perturbation of an otherwise harmonic oscillator [63]. In this case, the cosine term in (2.30) can be expanded to third order. Following the derivation in Koch et al. [63] and grouping harmonic and anharmonic terms, the Hamiltonian becomes

$$H = \sqrt{8E_C E_J}(\hat{b}^{\dagger}\hat{b} + 1/2) - E_J - \frac{E_C}{12}(\hat{b} + \hat{b}^{\dagger})^4 \tag{2.36}$$

where $\hat{b}$ and $\hat{b}^{\dagger}$ are the standard creation and annihilation operators for a harmonic oscillator. The energy eigenstates of Eq. (4.6) are

$$E_m \simeq -E_J + \sqrt{8E_C E_J}\left(m + \frac{1}{2}\right) - \frac{E_C}{12}(6m^2 + 6m + 3), \tag{2.37}$$

[63] for energy level m. Some very useful approximations for transmon qubits are for the transmon anharmonicity $\alpha \approx -E_C$. This is the energy difference between the transition for ground to excited state vs. the transition from excited to next-excited state. The negative sign indicates the spacing between the energy levels of the transmon get smaller with increasing energy. This will be important in Chapter 4

to model the cross-resonance effect including higher energy levels. Also, the plasma oscillation frequency, $\omega_p = \sqrt{8E_J E_C}/\hbar$ is a good approximation for the ground to excited state transition in a transmon qubit.

2.4.2 Qubit measurement

All measurements of qubits in this work are done in the energy eigenbasis. As with all measurements made on qubits, the experimenter will only ever measure the $|0\rangle$ or $|1\rangle$ state. To measure any other qubit component, appropriate rotations are made to project that part of the state onto the z-axis and measure (as in quantum state tomography in Section 2.6.1). For example, to measure the $\langle X\rangle$ component of a qubit state, a rotation (gate see Section 2.5) of $\pi/2$ is applied about the y-axis to rotate that component onto the energy eigenbasis (z-axis).

For a state in a superposition of these basis states $|\Phi\rangle = \alpha|0\rangle + \beta|1\rangle$, the average of many measurements will yield the proper probability $|\alpha|^2$ for the ground state and $|\beta|^2$ for the excited state. In particular, the assumption is made that a measurement happens as an ideal Von Neumann measurement and projects the state of the qubit onto one of its eigenstates. Typical cQED experiments can be viewed this way to varying degrees based on circuit parameters and the goals of the experiment. More general measurement formalisms exist [89] but were not explored in this work.

The majority of measurements in this work were done in the low-power, dispersive regime. A high power 'bright state' [98] type measurement was also used in places and will be discussed below. The low-power type of measurement is carried out in the dressed state of the cavity by filling the cavity with some number of photons less than n_{crit} and recording the transmitted or reflected signal. To see how this process works, it helps to rewrite Eq. (2.25)

$$H = \hbar(\omega_r + \chi\sigma_z)(a^\dagger a + 1/2) + \hbar\omega_{ge}\frac{\sigma_z}{2}, \tag{2.38}$$

where $\chi = g^2/\Delta$ is the state-dependent pull on the cavity by the qubit [15]. The χ parameter is modified for a transmon system as $\chi = \chi_{ge} - \chi_{12}/2$, where the subscripts indicate the cavity pull for the respective transition [63]. When the cavity is populated with photons, a measurement is made of σ_z, revealed through the shift in cavity frequency. Therefore, the cavity will have a qubit-dependent resonance at $\omega_r' = \omega_r \pm \chi$. By setting the measurement frequency to $\omega_r - \chi$, there should be an enhancement (reduction) in transmitted (reflected) amplitude when the qubit is in the excited state and the opposite when the qubit is in the ground state. The bright-state scheme [98] works in a similar way but uses the nonlinearity of the Jaynes-Cummings system to engineer a qubit state-dependent shift in ω_r' out of the dressed state $\omega_r \pm \chi$ and back to the bare resonance ω_r. This involves photon numbers greater than n_{crit} and fine tuning the power and frequency of the measurement signal to maximize the contrast between the two states. This process can be tedious to tune up by hand, but can yield a high signal-to-noise ratio.

The measurements of Chapter 3 were done using the bright-state technique. It is also used in some of our 3D qubit [93] experiments at Syracuse where signal to noise can be low due to microwave filtering and small χ shifts. In some experiments we have observed other detrimental effects when using the bright-state readout. Due to the large number of photons, we have seen evidence of Cooper pair breaking from drives with energy greater than the superconducting gap 2Δ.

In our lab, signals leaving the device under test pass through a series of microwave isolators before being amplified with a high electron mobility transistor (HEMT). The signal then travels out of the fridge to additional amplification before being recorded. The noise added by the HEMT is an order of magnitude too high to allow the state of the system to be inferred accurately from a single measurement. In particular, the HEMT adds around 20 photons of noise at the cavity measurement frequency. This requires measurements to be averaged many times to reach an accurate measure to the system. So called 'single shot measurements' can be done using a quantum limited limited amplifier such as a Josephson bifurcation amplifier [121, 116], Josephson parametric converter [11] or a superconducting low-inductance undulating galvanometer [55]. These devices allow for high-fidelity, single-shot quantum non-demolition (QND) measurements [44]. A QND measurement means the state after measurement is not destroyed in the measurement process. Additionally, the measurement can be repeated many times returning the same result over time scales that are short compared to the qubit lifetime. QND measurements are one of the necessary building blocks for a fault-tolerant quantum computer.

2.5 Quantum gates

Single-qubit gates in superconducting systems can be achieved with microwave pulses of the proper length, frequency, amplitude and phase. These can be viewed as manipulations of a pointer state on the Bloch sphere [89]. A microwave pulse on resonance with the qubit 0-1 transition will implement a rotation about an axis in the equatorial plane of the sphere. The direction of this axis will depend on the phase of the pulse. The length and the amplitude of the pulse set how far the state is rotated on the sphere. A rotation of π around the x-axis in the equatorial plane has the effect of flipping the qubit state along the z-axis. As the z-axis is typically chosen as the basis for the qubit energy states, this rotation implements a bit flip from $|0\rangle \rightarrow |1\rangle$ if the qubit was in the ground state before the pulse. The opposite occurs if the qubit was in the excited state $|1\rangle \rightarrow |0\rangle$. In a two-dimensional state space, these operations are well described by the Pauli spin operators where $\sigma_{\{x,y,z\}}$ represent π rotations around the x, y, and z axes [89]

$$\sigma_x = \begin{pmatrix} 0 & 1 \\ 1 & 0 \end{pmatrix}, \sigma_y = \begin{pmatrix} 0 & i \\ -i & 0 \end{pmatrix}, \sigma_z = \begin{pmatrix} 1 & 0 \\ 0 & -1 \end{pmatrix}. \tag{2.39}$$

We can denote an arbitrary rotation around one of the cardinal axes by some amount θ as

$$R_J(\theta) = e^{-i\theta J/2}, \tag{2.40}$$

with J equal to one of the spin operators [89]. The rotation axes need not be restricted to the cardinal directions. The formalism can be extended to any arbitrary axis since that axis could be decomposed into its three Pauli components. In the scope of work presented here, the most common gates will be π and $\pi/2$ rotations about the x-axis. These gates are used in the time-domain experiments described earlier and will make appearances in Chapter 3 and Chapter 4. Rotations about both x and y-axes are used in quantum state tomography to project different parts of the quantum state onto the z-axis. If the qubit has a SQUID loop and a flux degree of freedom, dc current pulses that can be used to quickly tune the frequency implementing a phase gate as a rotation around the z-axis.

The case of two-qubit gates is naturally more complicated. There are a variety of ways these gates can be implemented in superconducting qubits. A controlled phase gate [77] can be executed with fast dc pulses that tune the frequencies of two qubits near each other for a set amount of time. In this case, one qubit obtains a phase dependent on the energy state of the other qubit. The cross-resonance effect [99] can be used to make a CNOT gate between two qubits with only microwave control. The CNOT gate will be of particular importance in Chapter 3 and Chapter 4.

The CNOT gate is a conditional bit flip operation on a designated target qubit based on the state of a control qubit. In the quantum case the operation can be represented with a matrix

$$\begin{pmatrix} 1 & 0 & 0 & 0 \\ 0 & 1 & 0 & 0 \\ 0 & 0 & 0 & 1 \\ 0 & 0 & 1 & 0 \end{pmatrix}, \tag{2.41}$$

written in terms of the two-qubit computational basis $\{|00\rangle, |01\rangle, |10\rangle, |11\rangle\}$ with the first qubit used as the control. This type of gate is very useful for creating entangle-

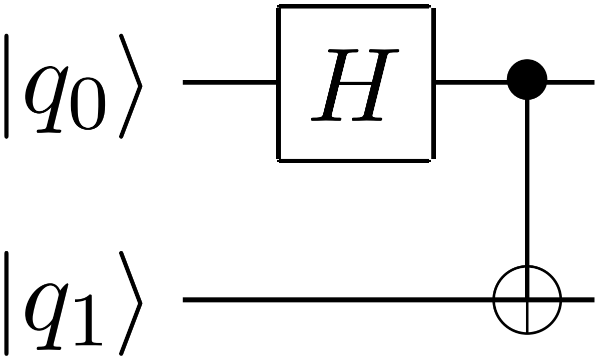

Figure 2-11: Bell state generation. The H box represents a Hadamard gate on the first qubit followed by a CNOT gate represented by a solid dot on the control qubit connected to the target qubit (cross symbol) by a solid line. The end result of the process is $|\Psi^+\rangle = (|00\rangle + |11\rangle)/2$ the two qubits q_0 and q_1 are in the ground state.

ment between qubits. A Hadamard gate and CNOT are shown in Figure 2-11. The Hadamard gate creates superpositions of the two energy eigenstates $(\alpha|0\rangle + \beta|1\rangle)$ with a matrix

$$\begin{pmatrix} 1 & 1 \\ 1 & -1 \end{pmatrix}, \tag{2.42}$$

acting on a general $[\alpha.\beta]$ state. If q_0 and q_1 are both in the ground state $|0\rangle$, the process generates a Bell state of the first kind $|\Psi^+\rangle = (|00\rangle + |11\rangle)/2$. This type of process is used in error detection and correction schemes where direct measurement of a qubit is prohibited, but an auxiliary qubit can be measured after it has been entangled with the original qubit with a CNOT gate. The ubiquitous nature of the CNOT gate make it an important gate for scaling qubit systems. The CNOT gate along with the continuum of single qubit gates is universal for quantum computing [89].

Other two-qubit gate types exist, including resonant swaps and ac-Stark shift based gates [15], all microwave gates [28] and FM sideband gates[2] [10] among others.

---

[2] Primitive two-qubit interactions for this type of gate will be the focus of Chapter 3 and Chapter 4.

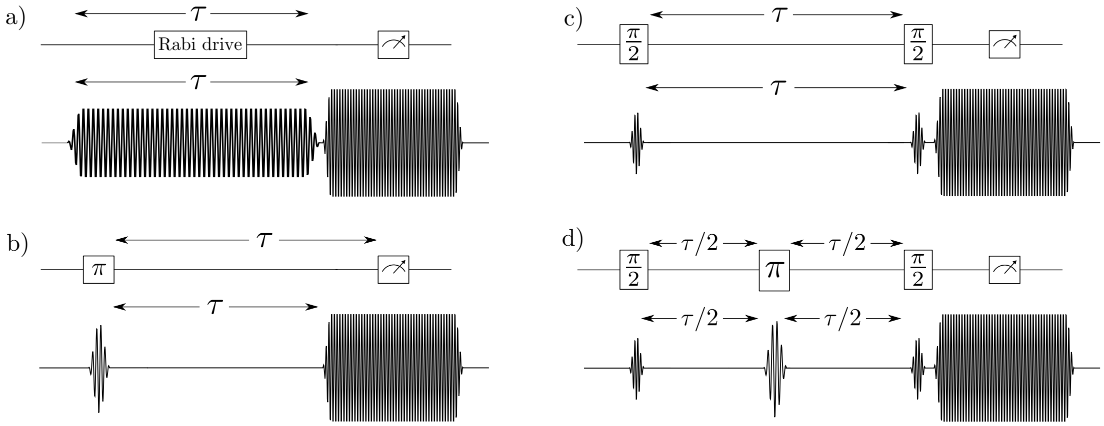

Figure 2-12: Time domain pulse schematics. Pulse schematics showing the four most common types of time-domain measurements used to quantify qubits in our lab. **(a)** Rabi oscillation experiment where the qubit is driven on or near resonance for a variable amount of time τ then read out through a measurement of the cavity state. **(b)** A T_1 or inversion recovery measurement of energy relaxation. The qubit is first prepared its $|1\rangle$ state then its excited state probability is measured as a function of the measurement delay τ. **(c)** T_2^* or Ramsey fringe measurement which is used to measure the phase coherence of the qubit. **(d)** Hahn echo sequence used to measure T_2 by inserting a refocusing pulse halfway through the measurement.

2.6 cQED time-domain measurements

To begin measuring the quality of cQED systems and their resilience to decoherence, we need to measure system dynamics in the time-domain. In general, time-domain measurements can be broken into two sections: manipulation and measurement. A state will be prepared or a drive turned on and the state is allowed to evolve for a set time. Then the state of the qubit is read out as a function of time. These control sequences are typically designed to highlight individual noise sources and decay channels.

The two broad categories of qubit decoherence are energy relaxation and the loss of phase coherence. In the case of energy relaxation the physical mechanism could be a variety of things from proximity to a superconducting resonator to spurious two-level states (TLS) on the surface or interfaces of the materials making up the circuit.

Regardless of the underlying microscopic cause, the effect on the qubit is to provide a system with which to exchange energy. Thus a qubit prepared in the excited state will decay, through some energy exchange mechanism, to its ground state with some characteristic time called T_1.

To measure this energy relaxation time, the qubit is repeatedly prepared in its first excited state and measured at some time τ later as in fig. 2-12. Where the π box corresponds to a pulse tuned in time, amplitude and frequency to drive the energy splitting between the ground and first excited state to prepare the qubit in its excited state $|1\rangle$. A T_1 measurement trace is shown in Figure 2-15. Typically this pulse is short compared to the characteristic time T_1 to allow for a quick drive to the $|1\rangle$. This increases visibility of the decay envelope. If the pulse is on the order of T_1, the qubit will undergo significant energy relaxation during the state preparation. This leads to a loss in visibility. If short pulses are not experimentally feasible, a pulse much longer that T_1 will leave the qubit excited population $P(e) = 0.5$ and this state will also decay with the same characteristic exponential decay time as a full excited state. The drawback to this method is a decrease in decay signal by one half.

Essentially, this long T_1 type measurement corresponds to a Rabi oscillation experiment where the Rabi oscillations have been completely damped. In a traditional Rabi experiment, the qubit is pulsed at its transition frequency for a variable length of time (see Figure 2-12). A Bloch sphere represnetation of a Rabi oscillation experiment is shown in Figure 2-13. For each τ, the qubit state is measured and averaged with identical state preparations. As the pulse length is increased, the qubit state population first transitions to the excited state, then continues back to the ground state. A measured Rabi oscillation is shown in Figure 2-14. This first cycle of a Rabi oscillation is useful for determining the time parameter of a π-pulse for a given drive amplitude. This oscillating behavior continues until the end of the qubit drive pulse or until system noise has completely damped them.

Dephasing for a qubit system is generally captured by considering frequency vari-

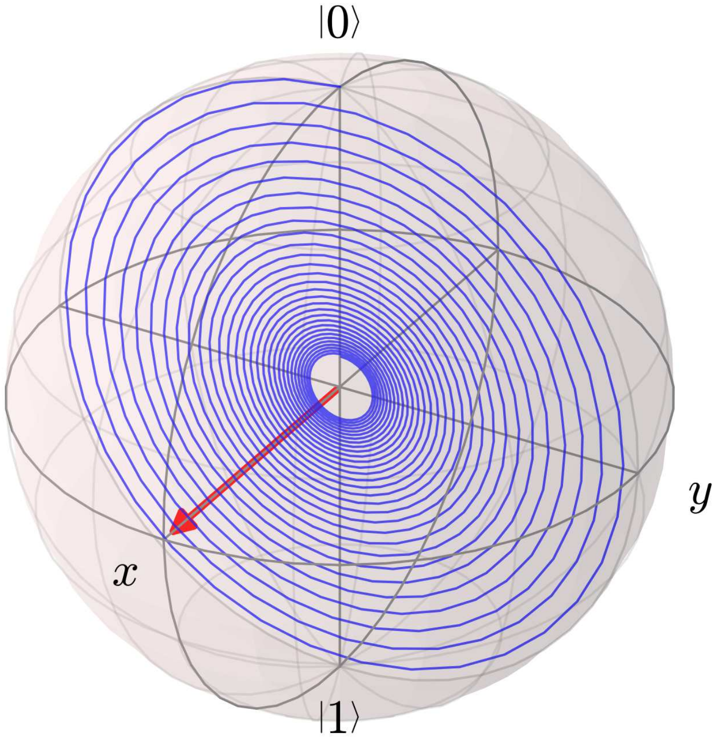

Figure 2-13: Bloch sphere representation. Rabi oscillation experiment plotted on the Bloch sphere. The blue line shows the precession of the state while being driven and the red arrow represents the axis around which the drive is being applied. In this case, the drive is applied around the x-axis. This corresponds to a Pauli σ_x operator continuously acting on the system over the time period of the drive. Plots created using Qutip [58]

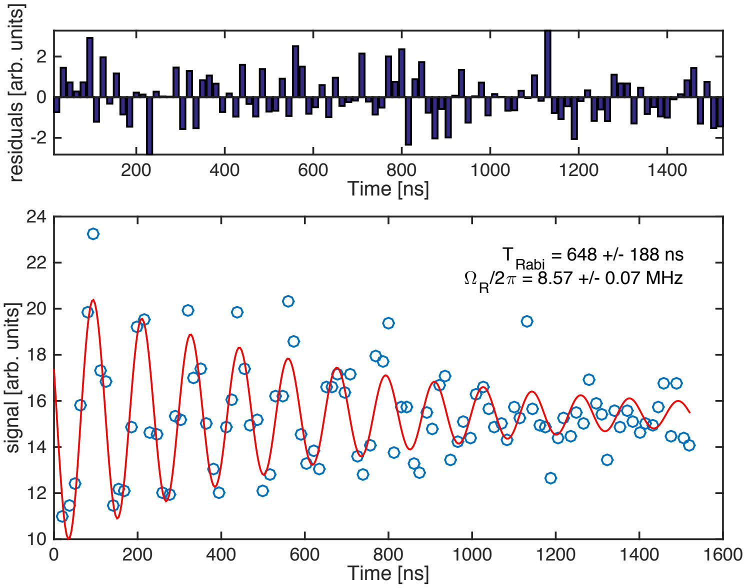

Figure 2-14: Rabi oscillation measurement. This Rabi oscillation was measured using a capacitively shunted flux qubit. To extract the oscillation parameters, the measurement trace was fit to an exponentially damped cosine with the simple least-squares method. [a]

---

[a] The MATLAB code used to produce this plot is from the Qlab package written by Blake Johnson and Colm Ryan at Raytheon-BBN Technologies. `https://github.com/BBN-Q/Qlab`

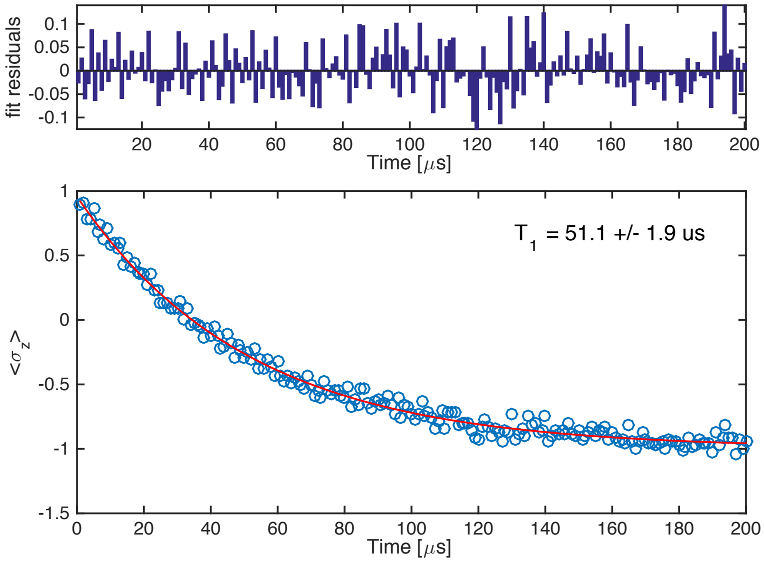

Figure 2-15: T1 measurement. A measurement of energy relaxation for one of the qubits on the chip used in Chapter 4. The decay envelope is extracted from the data by a least-squares fit to an exponential decay model.

ations in the qubit ω_{ge} transition frequency. This loss channel will be discussed in greater detail in Chapter 5. Here I will give a brief overview of how this quantity, called T_2^*, is measured in cQED systems. To measure qubit dephasing, we need to put the qubit in a state where it is sensitive to dephasing. This corresponds to a state on the equator of the Bloch sphere. In Figure 2-16, a $\pi/2$ pulse is applied to the qubit, creating the $|0\rangle + |1\rangle$ state. Note that we could also have driven around any of the other axes in the x-y plane to create a superposition of the ground and excited states. All of these would be equally susceptible to dephasing.

A second $\pi/2$ pulse is applied and this projects the qubit state onto the z-axis. As τ is increased, the probability of measuring $|1\rangle$ decreases exponentially as the state dephases. In a Ramsey fringe measurement, the drive frequency also matters. A pulse that is off-resonant with the qubit transition will create a Bloch pointer state in a rotating frame processing at the frequency difference $|\omega_{ge} - \omega_d|$, where ω_d is the drive frequency. This frequency difference leads to fringe oscillations in the measured

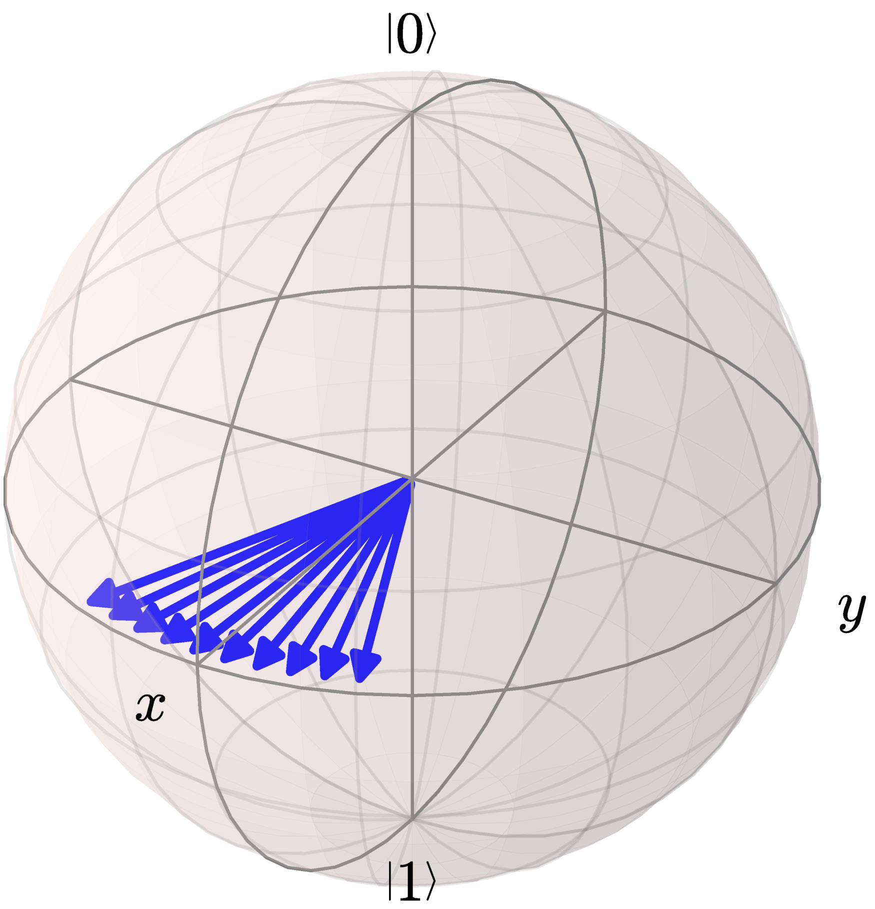

Figure 2-16: Bloch sphere dephasing. The qubit is prepared in $|0\rangle + |1\rangle$ state with a $\pi/2$ pulse. The blue arrows represent possible qubit states after some time τ in a Ramsey type experiment. Note an off resonant $\pi/2$ pulse will create states in the plane, but oscillating at a different frequency. This type of drive will induce oscillations in the measured trace at a frequency $f_{\text{Ramsey}} = |\omega_{eg} - \omega_d|$

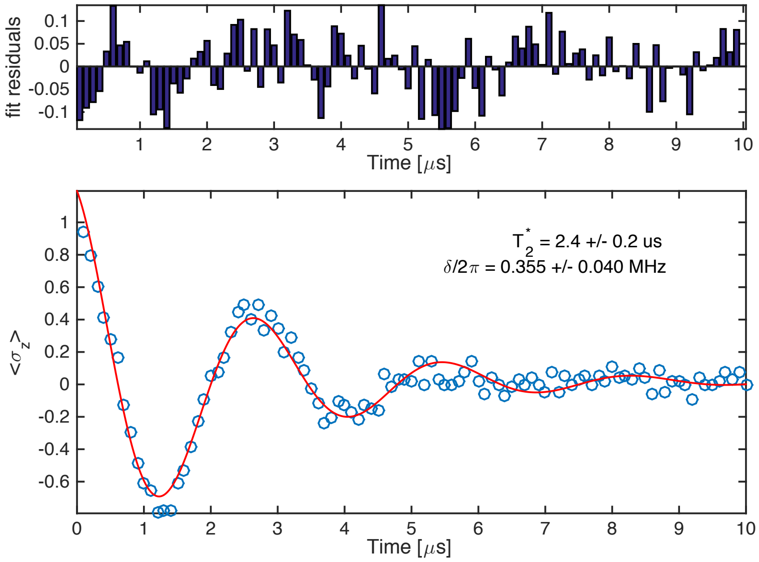

Figure 2-17: T_2^* measurement. A Ramsey fringe measurement of dephasing time for one of the qubits on the chip used in Chapter 4

traces.

Finally, the Ramsey sequence is, in general, much more sensitive to pulse calibration. In a T_1 measurement, ideal pulses drive the qubit completely into the excited state, but the state decay can be measured (in the large average limit) with any decay envelope. Therefore, as long as some percentage of the $|1\rangle$ state is populated, T_1 can be measured. In the case of T_2^*, it is important to have a well tuned $\pi/2$ which puts the Bloch vector on the equator as in Figure 2-16.

Spin echo techniques [50] can also be used in superconducting systems to measure T_2 instead of T_2^*. In an echo sequence, a π-pulse is applied to the qubit about the x or y-axis halfway through a Ramsey type experiment. This causes the winding of the Bloch vector in the equatorial plane due to low-frequency dephasing noise to be reversed precisely halfway through the measurement. This refocuses the qubit state in the equatorial plane of the Bloch sphere and only intrinsic, random variations in the qubit energy splitting, of higher frequency noise, on timescales faster than the echo time will be measured. This is the difference between a measurement of T_2 and T_2^*.

Implicit in the discussion above is the assumption that the qubit starts in the $|0\rangle$ state. There are several reasons why that might not be a safe assumption. Ideally, with $\hbar\omega_{ge} \gg k_B T$ a qubit would start in its ground state, however it is possible for a qubit to be excited by non-equilibrium processes or insufficient shielding from infrared radiation [35, 9]. Even with proper shielding and an exponentially suppressed thermal population, in practice the population can be as high [46]. This is especially the case in 3D qubit systems where at sub-Kelvin temperatures both the substrate and the microwave cavity are thermal insulators [17]. Another important issue as coherence times increase is the amount of time needed for passive thermal reset. This is the process of waiting a fixed amount of time for the qubit population to passively relax back to the ground state, and is the most standard process for qubit initialization. To reduce this time, active reset protocols have been developed [103] and are being improved [46]. Though none of these active reset techniques were used in the work of this dissertation, they are an increasingly important part of larger qubit systems.

The coherence of superconducting qubits has steadily increased in recent years. Energy relaxation and dephasing times have both improved to the tens and even one hundred microsecond range in some superconducting systems [100, 94]. A good example is the contrast between characteristic T_1 times for devices used in Chapter 3 vs. Chapter 4, where devices were measured with $T_1 \simeq 2 - 3\,\mu s$ and $T_1 \simeq 58\,\mu s$, respectively. It is likely the energy relaxation of the first device was enhanced by over-coupling to the bias lines [117], but the improvements are still impressive. Only a few years separate these transmon qubits, but a substantial amount of microwave and material engineering went into removing relaxation channels in these systems [28]. Coherence times and gate error rates have exceeded the threshold for quantum error correction [8] in superconducting systems and some basic operations have been demonstrated [61, 102].

2.6.1 Gate metrics

There are two canonical ways of quantifying the quality of qubit gate operations: quantum process tomography [129, 12] and randomized benchmarking [25]. Quantum process tomography is a descendant of standard quantum state tomography used to characterize the effect of a process on a spanning set of states. This is accomplished by preparing a spanning set of states[3] and measuring how the process changes the basis states [89, 26]. Comparing the measured data with the ideal process, a gate fidelity can be defined as

$$\mathcal{F}_{\text{state}}(\rho_{\text{ideal}}, \rho_{\text{noisy}}) = \left(\text{Tr}[\sqrt{\sqrt{\rho_{\text{noisy}}}\rho_{\text{ideal}}\sqrt{\rho_{\text{noisy}}}}\,]\right)^2, \tag{2.43}$$

[33] where ρ_{noisy} is the total state density matrix measured after the process and ρ_{ideal} represents a perfect gate implementation. Quantum process tomography suffers from two major drawbacks. The first is the exponential scaling in the number of qubits. As the number of qubits is increased the states space grows exponentially with the number of qubits making full process tomography infeasible for systems of more than a few qubits. Second, quantum process tomography is sensitive to state preparation and measurement (SPAM) errors. It is not possible to distinguish errors in the process one would like to characterize from errors in the state preparation or measurement of the system. This is particularly troublesome if the SPAM errors are of the same magnitude as the process to be characterized.

Randomized benchmarking (RB) is the process of applying a random sequence of gates[4] of length N to a qubit or mulit-qubit system [62, 25]. A final $N+1$ gate is added on to the end, which is calculated to be the inverse of all the N gates in the sequence. This process is repeated for increasing values of N, where the system

---

[3] This is d^2 where d is the dimension of the system. A two qubit system would have $d = 4$ and need 16 orthogonal states to characterize a two-qubit process. A three qubit system would require a 64x64 matrix.

[4] A set of gates much be chosen to pick from. A traditional choice is the Clifford group which makes up the 24 different rotations that take one cardinal axis to another on the Bloch sphere.

ground state $|00...0\rangle$ is chosen as a starting point. The fidelity is defined simply as the probability of finding the two qubit state in the ground state $|0\rangle \otimes |0\rangle$, measured as a function of N. An exponential fit to this data returns the *average* fidelity of qubit gates used [62, 105]. A recent modification [71, 73] to the RB protocol allows the average error per gate of a particular gate to be extracted by interleaving the gate of interest in an otherwise random sequence. This process replaces every other random gate with the gate of interest. RB is also not sensitive to SPAM errors and scales favorably (sub-exponentially) in the number of qubits. A more quantitative description of RB is given in Chapter 4, where the technique is used to benchmark a CNOT gate produced with the cross-resonance effect.

2.6.2 Scaling superconducting systems

In recent years, gate times have gone down and fidelities have increased to the point that researchers are now thinking seriously about scaling from a few qubits to many thousands of qubits. To maintain quantum coherence and control in systems that large, quantum error correction codes will be necessary [47, 97, 42]. A variety of error correcting codes exist, with the surface code being the most popular due to its relatively high tolerance to errors and only requiring nearest-neighbor interactions [42]. The requirements for building a surface code implementation with superconducting qubits are the motivation behind many of the recent experiments demonstrating low error rates [8] and parity measurements [29, 102, 34] necessary for error detection and correction.

2.7 Device fabrication

Significant work for this dissertation involved the fabrication of superconducting qubit devices. This section will quickly detail some of the processes used to make the systems measured in later chapters. The design for samples presented in this work

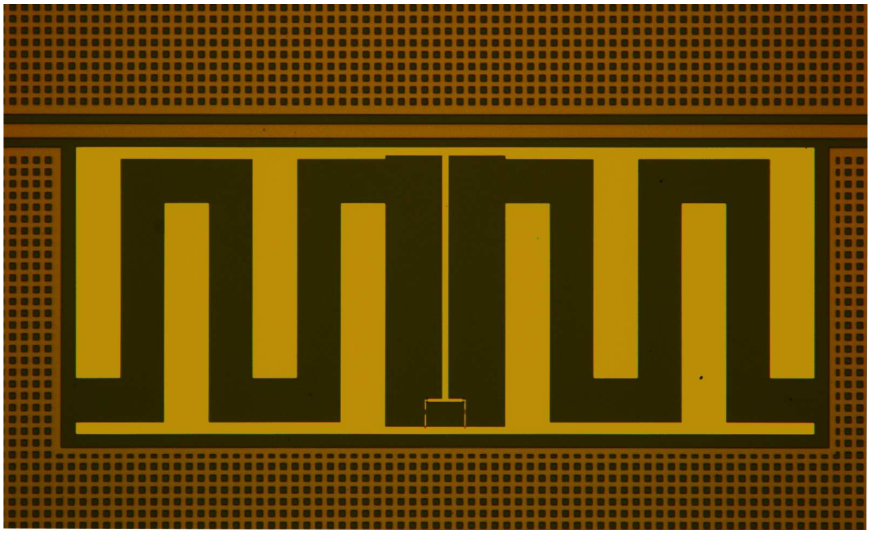

Figure 2-18: Transmon micrograph. An optical micrograph of a asymmetric transmon device. The lighter color material is aluminum, which forms the qubit capacitors and two Josephson junctions. The orange colored material is niobium, forming a resonator (line across the picture) and the ground plane (waffle textured material) surrounding the qubit. The silicon substrate is a slate grey.

was accomplished mostly at Syracuse using commercially available software layout packages such as *Cadence Virtuoso* or *K-Layout*. Simulation was carried out in a similar manner with commercial software such as *ANSYS HFSS*, *ANSYS Q3D* and *Sonnet*. All of the devices presented here, except for the chip measured in chapter 4 were designed and made here at Syracuse with critical steps of the process done in the cleanroom at the Cornell Nanoscale Facility (CNF). For a more complete description of the fabrication process, see Appendix A.

Our process starts with a clean from-factory substrate. In most cases this is a high resistivity silicon or sapphire wafer. A superconducting metal is then deposited without further processing in a UHV chamber dedicated to a particular process and chemistry. For instance, we have a dedicated sputter system for depositing niobium and niobium nitride. This is done to avoid contamination from other metals, in particular ferromagnetic metals. The first layer forms the ground planes and resonant structures of the chip. This 100-200 nm-thick layer is then patterned in a photolithography step and etched in a class 1000 cleanroom at the CNF. After cleaning, a second lithography step, this time with electron-beam lithography, is used to pattern an aluminum (and aluminum oxide) layer that makes up our qubits and Josephson junctions. The metal and oxidation processes in this final layer are carried out in a dedicated aluminum evaporation and oxidation chamber at Syracuse. The final resist layer and metal are removed in a lift-off process. See Figure 2-18 for a representative device.

Chapter 3

Sideband Interactions

As superconducting systems have advanced, so have the variety of interactions researchers have been able to explore. For single-qubit gates, resonant microwave tones with proper phase, duration, and frequency are sufficient to manipulate the qubit state (see Section 2.5). Two-qubit gates are naturally more complicated due to the doubling of the number of qubit controls and the need for engineering the couplings between qubits. In superconducting qubits, this coupling takes the form of inductive or capacitative coupling between qubits directly or through shared microwave cavities [16].

In this chapter, I will describe a parametric interaction between a superconducting qubit and a cavity that allows excitations to be quickly swapped between the two systems via red sidebands. These interactions were first explored in trapped ion systems [30, 22]. This chapter will detail their experimental observation in superconducting qubit systems. The first Section 3.1 will work through the theory of sideband interactions in trapped ions and superconducting systems. Section 3.2 will describe the experimental techniques used to study these sideband interactions in the microwave regime. In Section 3.3, data and analysis will be presented on red sideband Rabi oscillations in a superconducting qubit system. In the final Section 3.4, details will be presented on how the sideband swap can be used to build a multi-qubit entangling gate.

3.1 Theory

3.1.1 Trapped Ions

Sideband transitions for quantum information processing were first explored in trapped ion systems. First proposed in Ref. [30] and experimentally implemented in [22], these methods have become a commonly used primitive for qubit gates in trapped ion systems [49, 69]. Following the presentations in [15, 22, 89], I will present the dynamics in these systems and highlight the similarities between ion trap sidebands and the sidebands in a superconducting cQED system.

The interaction of a spin $1/2$ state in a harmonic potential can be written as [89]

$$H_{\text{int}} = -\vec{\mu}\cdot\vec{B} = \mu_m \vec{S}\cdot B_1 \hat{z}\cos(kx-\omega t+\phi), \tag{3.1}$$

where S is the traditional spin operator, μ_m is the Bohr magneton, B_1 is the magnetic field strength, k is the momentum in the x direction for the spin, ω is the motional frequency and ϕ is the motional phase. In this harmonic potential, the position of the atom is quantized and x becomes $x_0(a^\dagger + a)$, with x_0 representing the RMS or zero-point motion. Taking $\eta = kx_0$ and making the assumption the vibrational amplitude is small , the cosine term can be expanded as [89]

$$\begin{aligned} H_{\text{int}} \approx & \left[\frac{\hbar\Omega}{2}\left(S_+ e^{i(\phi-\omega t)} + S_- e^{-i(\phi-\omega t)}\right)\right] \\ & + \left[i\frac{\eta\hbar\Omega}{2}\left\{S_+ a + S_- a^\dagger + S_+ a^\dagger + S_- a\right\}\left(e^{i(\phi-\omega t)} + e^{-i(\phi-\omega t)}\right)\right], \end{aligned} \tag{3.2}$$

where $\Omega = \mu_m B_1/2\hbar$ and $S_{\{+,-\}}$[1] are the raising and lowering operators for the spin (recall $S_x = (S_+ + S_-)/2$). The spin and harmonic terms on line two represent red and blue photon transitions. The first two terms are the red sideband single-photon swaps and the last two are the higher frequency blue sideband terms. Recall that

---

[1] in following Ref. [89], the Pauli operators were redfined as $S_x = X/2$, $S_y = Y/2$, $S_z = Z/2$. So the raising and lowering operators S_+ and S_- are related to the standard ones by a factor of two.

those terms evolve under the influence of $H_0 = \hbar\omega_r a^\dagger a + \hbar\omega_{ge}\sigma_z/2$ and cause the operators to evolve as

$$\begin{aligned} S_-(t) &= S_- e^{-i\omega_{ge}t}, \\ S_+(t) &= S_+ e^{i\omega_{ge}t}, \\ a(t) &= a e^{-i\omega_r t}, \\ a^\dagger(t) &= a^\dagger e^{i\omega_r t} \end{aligned} \tag{3.3}$$

in the lab frame. The red sideband terms become [89, 22]

$$\frac{i\eta\hbar\Omega}{2}\left\{S_+ a e^{i(\omega_{ge}-\omega_r)t} + S_- a^\dagger e^{i(\omega_r-\omega_{ge})t}\right\}, \tag{3.4}$$

appearing when the system is driven with a laser at $\omega' = \omega_{ge} - \omega_r$, and the blue sideband terms become [89]

$$\frac{i\eta\hbar\Omega}{2}\left\{S_+ a^\dagger e^{i(\omega_{ge}+\omega_r)t} + S_- a e^{-i(\omega_r+\omega_{ge})t}\right\}, \tag{3.5}$$

for a drive at $\omega' = \omega_{ge} + \omega_r$. The red sideband interaction of equation (3.4) has been used to make a π-swap between a trapped ion and magnetic trap with a gate time of 190 μs (5.3 KHz) at a magnetic cavity frequency of 6.5 MHz [92]. This interaction can be driven much faster in a superconducting qubit system [117] using a fast frequency modulating drive.

3.1.2 Sideband transitions with superconducting qubits

Sideband interactions also arise naturally in systems governed by the Jaynes-Cummings Hamiltonian [56]. As we saw in the last Section 3.1.1 for trapped ions, these interactions can be be used to drive transitions between the energy state of a spin 1/2 particle and its motional modes in a magnetic trap. The rest of this chapter will show how these transitions can be driven in a superconducting system [15, 117, 10].

Recall the basic Jaynes-Cummings (JC) Hamiltonian from Chapter 2 with a qubit coupled on resonance to a harmonic oscillator in the rotating-wave approximation

$$H = \hbar\omega_r a^\dagger a + \frac{\hbar\omega_{ge}}{2}\sigma_z + \hbar g(a^\dagger\sigma_- + a\sigma_+). \tag{3.6}$$

All terms in the Hamiltonian (3.6) are even in the number of ladder operators for both the qubit and cavity. This means energy is conserved in the absence of a drive term and the last term only mixes states of the same parity [15]. In this context, parity refers to the total number of excitations in the system including the cavity and qubit. In the dispersive regime $|\Delta| = |\omega_r - \overline{\omega}_{ge}| \gg g$, the last term acts only perturbatively. This means direct qubit-resonator coupling is prohibited to order $(g/\Delta)^2$. Conversely, a voltage drive term at the qubit frequency has the form $(a^\dagger + a)$(see equation (2.16) in Section 2.3.1), and has terms with an odd number of cavity creation and annihilation operators. This implies a voltage drive can only drive transition that change the total number of excitations in the qubit-cavity system. It will not be able to drive transitions with the same excitation parity like $|0,e\rangle \rightarrow |1,g\rangle$ or vice versa where $|n,e\rangle$ would be the n-photon cavity state with the qubit in the excited. This transition can only be driven at second order in g with a two photon process where the drive term essentially acts twice [15]. For example, a standard Rabi drive is implemented using an ac voltage drive of the form $(a + a^\dagger)$ applied to the resonator and corresponds to a transition like

$$|0,g\rangle \rightarrow |0,e\rangle. \tag{3.7}$$

This type of transition changes the number parity of total system excitations from even to odd.

With a transmon qubit in a split junction arrangement, it is possible to use the flux degree of freedom for qubit drive as well as the voltage drive just described [10] In a transmon qubit operated away from the flux-insensitive sweet spot, it is possible

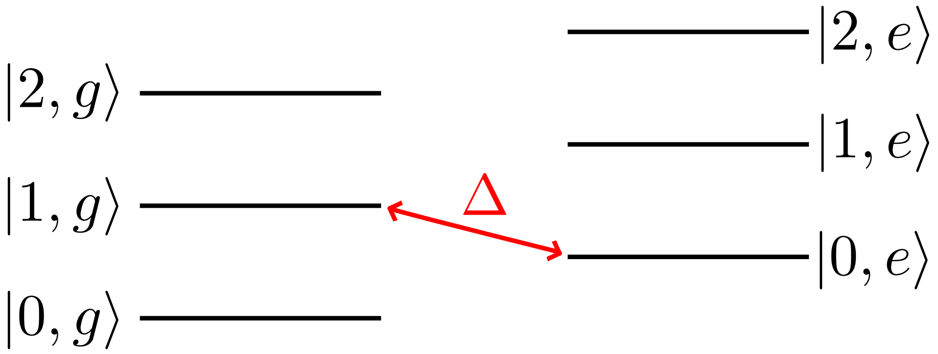

Figure 3-1: Red sideband level diagram. In the red sideband transition is highlighted. This is the energy level transition that will be driven with a time-varying flux drive. Δ represents the detuning between the qubit and cavity. Figure is adopted from Ref. [66]

to drive transitions of the same parity like

$$|0,e\rangle \rightarrow |1,g\rangle, \tag{3.8}$$

to first order in g using an ac flux coupled drive ω_{FC}. This transition is plotted in Figure 3-1. We can define the qubit energy term as

$$H_{\mathrm{FC}} = \frac{f(t)}{2}\sigma_z, \tag{3.9}$$

if an ac flux drive is allowed to modulate the qubit's transition frequency. For a sideband drive, f will have the functional form

$$f(t) = \overline{\omega}_{ge} + \frac{\epsilon}{2}\sin(\omega_{\mathrm{FC}}t), \tag{3.10}$$

where $\overline{\omega}_{ge}$ is the stationary frequency of the qubit at the static flux bias and ϵ is the amplitude of the frequency control (FC) drive [10]. Driving the qubit away from the sweet spot in this way breaks the symmetry of the JC Hamiltonian. The qubit-photon interaction can effectively be turned on by driving the flux degree of freedom with (3.10). To see this more clearly, we can make a unitary transformation using

$H' = U^\dagger H U - i U^\dagger \partial U / \partial t$ and

$$U(t) = \exp[-i(\overline{\omega}_{ge}\, t) - \frac{\epsilon}{2\omega_{\mathrm{FC}}} \cos(\omega_{\mathrm{FC}} t)\sigma_z - i\omega_r a^\dagger a\, t]. \tag{3.11}$$

The transformed effective Hamiltonian can be written as

$$H'(t) = g a^\dagger \sigma_- J_0\left(\frac{\epsilon_0}{\omega_{\mathrm{FC}}}\right) e^{-i\Delta t} + h.c. + g a^\dagger \sigma_- \sum_{m=1}^{\infty} (-i)^m J_m\left(\frac{\epsilon_0}{\omega_{\mathrm{FC}}}\right) e^{i(m\omega_{\mathrm{FC}}-\Delta)t} + h.c., \tag{3.12}$$

where $J_m(z)$ are Bessel functions of the first kind, $a^\dagger$ is the standard photon creation operator , σ_- is the standard qubit lowering operator and Δ is the qubit-resonator detuning [10, 117]. Data taken in the dispersive regime, which means the qubit-cavity detuning Δ is large. In our case $\Delta/2\pi = 400\,\mathrm{MHz}$. This means the first term of (3.12) will oscillate rapidly and average away in the dynamics. The second term in (3.12) also oscillates rapidly except for the cases where $(m\omega_{FC} - \Delta) = 0$. Crucially, this implies a static term of order $gJ_m(\epsilon/\omega_{\mathrm{FC}})$ appears when $\omega_{\mathrm{FC}} = \Delta/m$. This condition corresponds to the m-photon sideband transition. This speed of this transition is controlled by the amplitude of the magnetic flux drive. For large amplitudes, the swap interaction can be driven at a rate slightly higher than g. If we take the bare, on-resonant swap frequency $2g$ (see Figure 2-6) times $\max[J_1(\epsilon/\omega_{\mathrm{FC}})]$ a value of $1.16g$ is found for the optimal value of $\epsilon/\omega_{\mathrm{FC}} = 1.84$. Blue sidebands could also be driven with a drive at $\omega_{FC} = \omega_r + \omega_{eg}$. This type of drive was harder to realize in practice for our system since ω_{FC} needed to be roughly 16 GHz. This would have pushed the bandwidth limits of our measurement wiring.

3.2 Experimental Implementation

To measure the frequency-modulated sideband oscillations we designed a superconducting system made of two flux-tunable qubits coupled to a single CPW resonator. The device parameters were chosen so the qubits could be tuned close to the res-

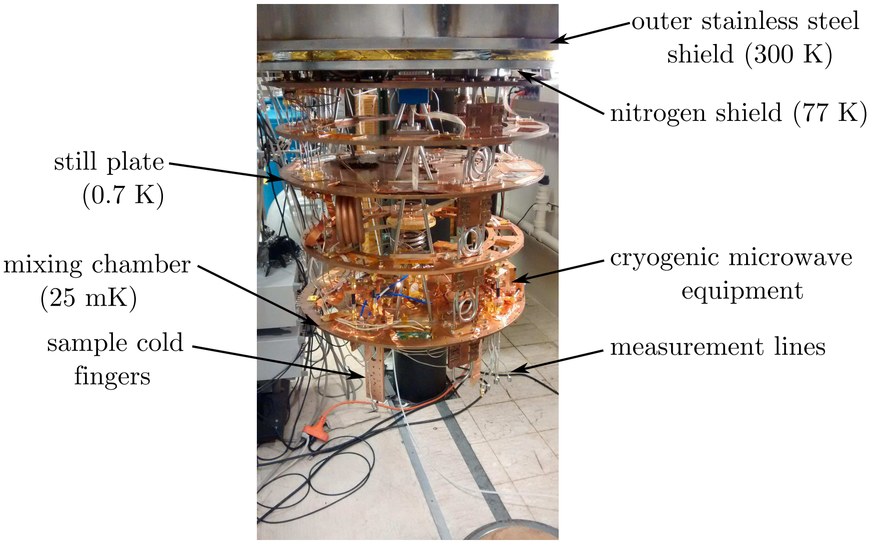

Figure 3-2: Dilution refrigerator. A picture of our ^{3}He/^{4}He dilution refrigerator. All qubit experiments done at Syracuse are conducted using this fridge. Arrows point out some of the important parts of the fridge with temperatures getting colder towards the bottom of the photograph.

onator frequency and be in a favorable part of its flux modulation curve. The device was cooled to 25mK in a custom dilution refrigerator(Figure 3-2). This is well below the transition temperatures of the superconducting metals used in the circuit and in the regime where qubit and cavity energies are large compared with thermal energies $\hbar\omega_{\{r,eg\}} \gg k_B T$. Control pulses were produced using the pulsing capabilities of commercially available microwave generators. In contrast, the sideband drive tones were digitally synthesized using a custom arbitrary pulse sequencer with no microwave electronics hardware [1]. The qubits were measured using the dispersive frequency shift of the resonator (see Section 2.4.2). The control and measurement sequence was initiated and controlled by a MATLAB program.

3.2.1 System parameters and design

To study this type of interaction, an ideal qubit system would be tunable and have long coherence times relative to the timescale of the experiment. For these reasons, we chose the transmon-style qubit made with two Josephson junctions forming a SQUID loop shunted by a capacitor. The loop formed by the junctions allows flux to be threaded through and the E_J of the qubit to be changed as in (5.1). This allows the $\Delta = |\omega_r - \omega_{ge}|$ parameter to be adjusted with a static flux bias and for fast flux pulses at ω_{FC} to be applied to the qubit. A modification is made to the traditional transmon system for this experiment. The two junctions forming the qubit are made to be identical in conventional transmon systems. Here we intentionally break this symmetry by making one junction much larger in the lithography process. We call this type of transmon an *asymmetric transmon*. This has several effects on the qubit's response to flux biasing. First, with significant asymmetry, equation (2.34) is described by (2.35) and the vanishing of E_J at odd half-odd integer flux quanta is removed. It is replaced by a second 'lower sweet-spot' where the sign of $\partial f/\partial\Phi$ changes. At this bias point the qubit is insensitive to flux noise to first order just as it is at integer multiples of Φ_0. Second, an inflection point forms between the two sweet spots. At this point, the flux-to-frequency transfer function is approximately linear. This behavior is plotted in Figure 3-4. If the qubit is statically biased with $\overline{\omega_{ge}}$ in this region, the linearity of the transfer functions means harmonics of the FC drive will not show up as harmonics in the frequency modulation. The absence of geometric distortions to the sideband frequency from the modulation curve is an appealing feature of an asymmetric transmon for a flux modulation drive. Finally, the ability to control the amount of asymmetry allows the experimenter to pick how much the qubit will modulate with flux. In this experiment, a 3:1 asymmetry was chosen to give a 3 GHz range of tunability between the upper and lower sweet spots. A more asymmetric qubit would modulate less with magnetic flux bias. This aspect of the asymmetric transmon will be discussed in further detail in Chapter 5.

For this experiment, we fabricated two asymmetric transmon qubits though sideband experiments were only carried out on one of these qubits. Both were coupled capacitively to the voltage antinodes of a CPW resonator made of niobium with a bare

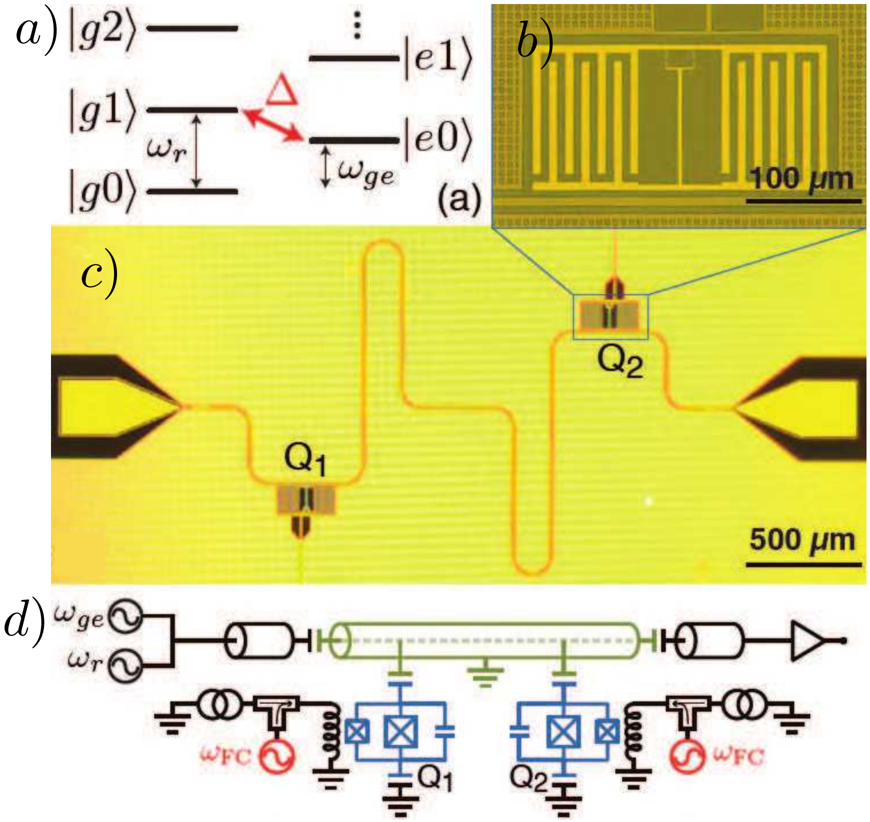

Figure 3-3: Sideband chip picture and diagram. Picture of the device showing the cavity and qubit, Q2, used in the experiment. **(a)** an energy level diagram showing the red sideband driven in the experiment. **(b)** optical micrograph of one of the asymmetric transmons on the chip. **(c)** another optical micrograph showing the chip with both qubits, microwave cavity and bias lines. **(d)** a microwave schematic of the circuit showing how the chip is driven during the experiment. Figure taken from [117].

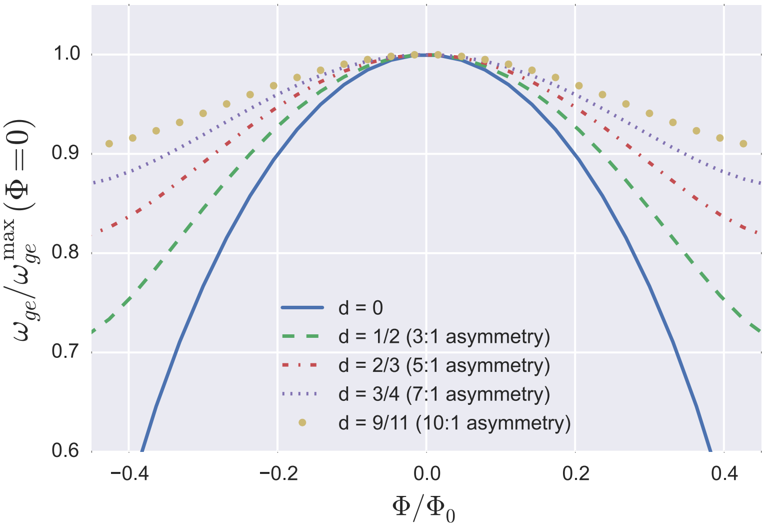

Figure 3-4: Asymmetric transmon modulation. Plot of the change in frequency vs. flux for several different asymmetries in an asymmetric transmon. This pattern is periodic in the applied magnetic flux with period Φ_0

resonance frequency of $\omega_r/2\pi = 8.102\,\text{GHz}$ and a linewidth $\kappa/2\pi = 0.37\,\text{MHz}$ [117]. The mode structure for the fundamental of the resonator was such that the voltage antinodes were at the ends of the resonator. A junction asymmetry of $d = (I_0^1 - I_0^2)/(I_0^1 + I_0^2) \approx 0.5$, where d is from equation (5.2) and $I_0^1(I_0^2)$ are the critical currents for the large (small) junctions. This led to a modulation depth of roughly 3 GHz between the upper and lower sweet spots. Figure 3-5 shows the measured frequency modulation of the qubit used in this experiment. As shown in Figure 3-3, each qubit has individual flux-bias lines. **(b)** shows the interdigitated capacitor that forms the qubit body and the SQUID loop. The lower part of Figure 3-3 shows a microwave schematic of the system, where the resonator is capacitively coupled to two both qubits and to the input and output lines. Red and blue sideband oscillations were measured on both qubits, but the data presented below is from Q2 only. Parameters measurements for Q2 yielded a charging energy $E_C = 158\,\text{MHz}$, Josephson energy $E_J = 66\,\text{GHz}$ and an asymmetry $d = 0.49$. These parameters were close to

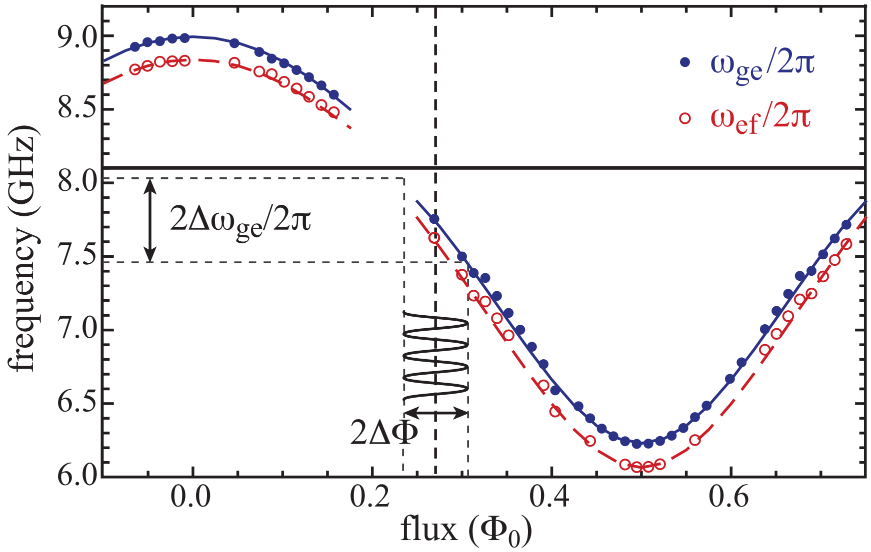

Figure 3-5: Asymmetric transmon modulation. The flux modulation of the asymmetric transmon. The solid blue dots represent the fundamental ω_{ge} transition and the red, hollow dots are transitions to the second excited state ω_{ef}. Solid and dashed lines represent numerical diagonalization of the system Hamiltonian including 4 transmon energy levels. The amplitude of the FM drive is shown as $2\Delta\Phi = 70.9\,\mathrm{m}\Phi_0$, which corresponded to an amplitude in frequency space of $2\Delta\omega_{ge}/2\pi = 572\,\mathrm{MHz}$. This drive amplitude corresponds to the strongest drive in Figure 3-6 and Figure 3-7. Figure taken from [117].

the design targets meant to place the resonator fundamental frequency within a few hundred MHz of the qubit modulation inflection point.

Time domain measurements were preformed at the lower flux sweet spot and close to the inflection point where the sideband oscillations were carried out. At the sweet spot, an energy relaxation time $T_1 = 2.7\,\mu\mathrm{s}$ and dephasing time $T_2^* = 3.0\,\mu\mathrm{s}$ were measured. At the bias point where the sideband measurements were performed, $T_1 = 1.7\,\mu\mathrm{s}$ and $T_2^* = 0.6\,\mu\mathrm{s}$ were measured [117]. The reduction in T_2^* away from the flux sweet spot will be discussed further in Chapter 5. The reduction in T_1 is most likely due to the Purcell effect as the qubit-cavity detuning is lowered. This is also discussed in Chapter 5.

3.2.2 Control electronics

The control frequencies for this experiment are in the GHz range and usual microwave measurement protocols were used to insure high fidelity control. Here all microwave pulses were created directly with microwave generators. This has the advantage of simplicity, as the generator can be programmed and triggered with relative ease. The disadvantage in this case is the lack of control over the shape of the pulse. A commercial generator in pulse mode will output a square envelope at the programmed carrier frequency, but the sharp edges of the pulse will result in higher frequency components. This introduces noise in the drive signal that could drive the qubit out of the $\{|g\rangle, |e\rangle\}$ subspace for example. This importance of the pulse rise and fall effects can be reduced by increasing the pulse length, which is the strategy we adopt in this case. Ideally, the pulse shape would be controlled by a microwave vector generator or modulated with an IQ-mixer that can independently control the phase and amplitude. For this experiment, the first approach is used and qubit π-pulses were set to 100 ns as a compromise between speed and pulse fidelity.

The sideband drive was digitally synthesized with a custom arbitrary waveform generator made at Raytheon-BBN Technologies, though any arbitrary waveform generator that could produce a sinusoidal drive signal at the qubit-resonator detuning could be used. This is one of the most appealing parts of qubit control in a sideband scheme as the control pulses do not need to be in the microwave regime and can be controlled with the qubit-resonator detuning. Instead, the necessary frequency range is set by the qubit-cavity detuning Δ. The lower limit on Δ in practical cases is set by the Purcell effect which is discussed briefly in Section 5.2. This means some of the control electronics for enacting this kind of qubit drive do not need to be microwave equipment. This lowers the cost and measurement infrastructure necessary for qubit control.

In our system, all measurements are done at the cavity frequency. This is a consequence of the circuit QED dispersive readout used. As a result, the signal we want to measure is typically on the order of several GHz. For measurement electronics to process a signal at that frequency, it first needs to be down-converted to a frequency of a few MHz so that a fast digitizing card can record the signal. Similarly, control signals at the system frequencies need to be up-converted to on or near resonant with the system. This translation is done by sending the phase and amplitude control signals to the Q and I ports of an IQ-mixer. An IQ-mixer is a four port microwave device that takes a strong signal called the local oscillator (LO) and multiplies it by signals sent to the I and Q ports. This produces a second microwave signal called the radio frequency (RF) that is a mixture of the LO and the other control channels. The RF signal could then be sent to the device under test for control and measurement. This allows microwave signals with arbitrary amplitude and phase to be synthesized. The process just described is called up-conversion and the reverse, down-conversion process is also possible where the phase and amplitude information of a signal sent to the RF port can be extracted. This is the process used to record the measurement in this chapter. By driving the LO port with a slightly different frequency (~ 1 MHz) from that of the measurement pulse, the I and Q ports produce the amplitude and phase of the cavity response encoded in the amplitude of the I and Q signals with a frequency equal to the difference between the signal and LO frequencies.

This signal is then digitized with an Agilent AP240 fast data acquisition card. The measurement traces are then numerically integrated in software to produce a data point. Typically this process is repeated many times. Measurements are identically prepared and measured thousands of times to accurately determine the energy state of the qubit. In this sideband study, the state of the qubit is probed with a 8 μs pulse near the cavity resonance. The power and frequency of this pulse were finely tuned to induce a 'bright state' readout using the inherent non-linearity of the Jaynes-Cummings interaction [98].

To begin the sideband swap experiment, the chip was allowed to thermalize with the coldest stage of a dilution refrigerator. This allows for thermal initialization of the qubit in its ground state and a minimum number of thermal photons in the cavity. Then a π-pulse of appropriate time and power is sent into the cavity at the qubit ω_{ge} frequency to drive it into the excited state. Immediately following this, the flux modulation tone is applied to the flux-bias line of the qubit at the qubit-cavity detuning Δ. This signal had a Gaussian envelope to avoid unwanted harmonic structure. At the end of each time step t of the Rabi pulse, the state of the qubit is immediately measured as described above.

3.3 Sideband oscillations

A detuning of $\Delta/2\pi = 400\,\mathrm{MHz}$ was chosen as a trade off between proximity to the linear regime of flux modulation, detuning from the cavity fundamental frequency to avoid Purcell loss, and the maximum frequency which could be digitally synthesized with the custom digital synthesizer. Plots of the red sideband oscillations are plotted in Figure 3-6 as a function of duration t and flux modulation drive pulse frequency ω_{FC} for three different drive strengths. Measured data is on the left and numerical simulation to the master equation are on the right [117]. The scale bar in Figure 3-6

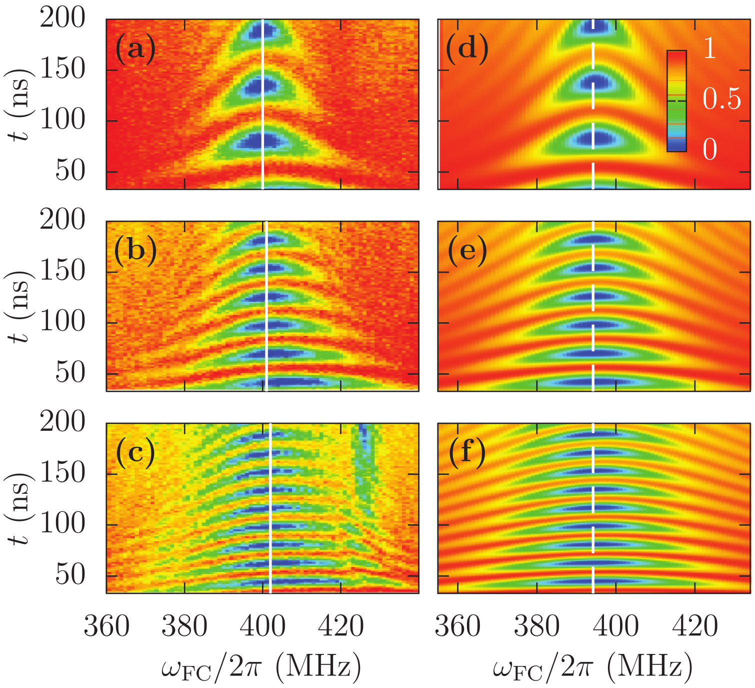

Figure 3-6: Red sideband oscillations. Rabi density plots of oscillations in and out of the cavity. **(a-c)** are experimentally measured density plots. **(a)** and **(b)** correspond to a reduction in drive amplitude of 10 and 4 dB respectively relative to **(c)**. **(d-f)** are numerical simulations produced with measured chip parameters. A solid (dashed) white line indicates the slice used in Figure 3-7. Figure taken from [117].

is calibrated using signal amplitudes from T_1 and standard Rabi oscillation measurements. The agreement between theory and data in Figure 3-6 is good and the frequency and power dependence is well captured. There are a few noticeable differences between the data and simulations. First, there is a frequency offset of 7 MHz between the center of the Rabi feature in the data and theory. As the theory plots were produced with parameters fitted from Figure 3-5, a likely source of error is the uncertainty in these numbers. There is also a small asymmetry in the Rabi 'chevron' patterns. This can be likely attributed to the frequency dependence of the waveform generator output leveling [117]. Lastly, there is a spurious feature around 430 MHz

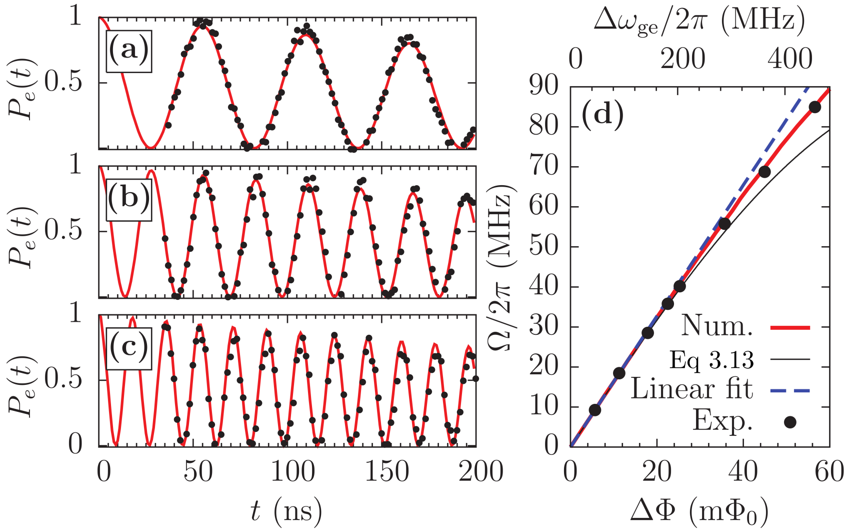

Figure 3-7: Sideband Rabi frequency vs. drive. a-c) are oscillations taken from the white cuts of Figure 3-6 where the red lines correspond to simulations on the right side of Figure 3-6 and the dots are experimental data points for the four different drive powers: 0,-4, and -10 dB. **d)** plots the oscillation rate vs. the flux drive amplitude (in flux and frequency). Figure taken from [117].

in the data at the strongest drive strengths. The feature could not be produced in the numerics, even when including the far detuned second qubit, Q1. Most likely this feature is caused by a spurious chip mode or unwanted resonance on the sample.

Figure 3-7 a-c shows individual frequency slices of Figure 3-6 for the three different drive powers. The red traces are not fits, but numeric solutions to the master equation done by our theory collaborators Félix Beaudoin and Alexandre Blais. Again, agreement between the data and simulations is excellent. The lack of data for $t <$ 20 ns is a technical limitation resulting from the minimum pulse length that could be produced by the generator. This limitation could easily be removed with more advanced pulsing capabilities. The oscillation decay observed in Figure 3-7 is fully captured by $(\kappa + \gamma_1)/2$, where κ and γ_1 are the independently measured cavity and qubit energy relaxation rates respectively. Figure 3-7 also shows the sideband rate vs. FM drive amplitude plotted in units of frequency excursion from $\overline{\omega}_{ge}$ and flux amplitude in mΦ_0. The response remains linear, even to swap rates as high as 85 MHz. Although for strong enough drives, Eq. (3.12) becomes nonlinear and the transmon frequency excursions will move into nonlinear regions of the flux-frequency curve.

Despite the large ac flux drive and frequency excursions, there was no loss of contrast in the sideband oscillations or additional decay dynamics observed that were not observed while the qubit was operated with a static flux bias. This is remarkable, as the qubit resonance frequency is passing through the cavity resonance at strong drives and should be sampling the loss channels and spurious resonances over a range of frequencies. This was the case for both the experimental data and the numerical simulations.

3.4 Sideband CNOT

The CNOT gate along with single qubit rotations is universal for quantum computing, as discussed in Section 2.5, and is a crucial part of many error correction schemes (see Section 2.6.2 and Chapter 6). The sideband interaction described above can be used to generate a CNOT gate as described in Beaudoin et al. [10]. The process involves a sequence of red sideband and traditional π-pulses [15, 16, 10]. These drive pulses exploit the higher levels of the transmon system that we neglected in the sideband oscillation experiment of this chapter. The notation in this section follows [10], where a sideband swap between the i and $i+1$ levels of the k_{th} qubit and the resonator is defined as $R^{(k)}_{i,i+1} = |i\rangle\langle i+1|^{(k)} a^\dagger + |i+1\rangle\langle i|^{(k)} a$. Similarly, a π-pulse is define for the $i \to j$ transition of k_{th} qubit as $\sigma^{(k)}_{x,i,j} = |i\rangle\langle j|^{(k)} + |j\rangle\langle i|^{(k)}$.

Using these definitions, the operation can be constructed as

$$U_{\mathrm{ent}} = R^{(1)}_{01} R^{(2)}_{12} \sigma^{(2)}_{x} R^{(2)}_{12} R^{(1)}_{01}, \tag{3.13}$$

which is equivalent to a CNOT gate modulo individual qubit phases. These phases can be removed with additional single qubit phase gates as [10]

$$\mathrm{CNOT} = U^{(1)}_{\theta_1} U_{\mathrm{ent}} U^{(2)}_{\theta_2} U^{(1)}_{\theta_3}. \tag{3.14}$$

3.5 Outlook

The speed at which photons can be swapped between each qubit and the cavity with the red sideband drive could give rise to CNOT gates on the order of 30-50 ns. This compares well with the current state of the art [8, 29] and a sideband-based gate would have the added advantage of not requiring microwave electronics for the FC drive. Moving forward, there are still a variety of studies that could be done with a sideband-driven qubit including actually implementing a CNOT gate. Work has been done in this direction [106], though practical gate implementation has proven to be rather challenging so far. Because this sideband process populates the cavity with real photons, all the qubits coupled to it have their transition frequencies ac-Stark shifted by the photon's electric field. This adds an extra layer of complexity when operating high fidelity gates since it is necessary to know the qubit resonance frequencies to high precision.

This requirement is not a complete roadblock and could in theory be circumvented. At the current date, there are there are other, more practical two-qubit gate protocols. Future work could also be done to mitigate the photon Stark effect. Tunable coupling could be implemented to isolate the qubit from the resonator while the red sideband interaction was off.

Chapter 4

Cross resonance

4.1 Introduction

Fast two-qubit gates are critical for any quantum computing scheme. Over the past decade, a variety of gates have been envisioned and implemented in superconducting qubits including controlled-phase gates [77, 8], cross-resonance [99, 27] and swap gates [39]. Most of these gates are used with other single-qubit gates to construct a controlled-NOT operation that can generate entanglement between two qubits. The CNOT gate is popular due to its heavy use in error detection and correction schemes. Along with single-qubit rotations, the CNOT is universal for quantum computing as discussed in Section 2.5. In this chapter I will describe a scheme for inducing state-dependent Rabi flopping in a two-qubit system. More specifically, we will study the cross-resonance effect (CR) [99] in detail and how the effect depends on qubit-qubit detuning.

CR arises in a two-qubit system when one qubit is driven at the frequency of a second qubit where both qubits are coupled through a common resonator. The second qubit, which is not being directly driven, Rabi oscillates at a rate that is dependent on the state of the first qubit. In a CR control scheme, the qubits will be detuned from the cavity and each other by at least a qubit linewidth to make the qubits individually addressable. In this gate setup, one qubit will be designated the 'target' qubit. This is the qubit that is not directly driven, but whose frequency is used to drive a second 'control' qubit. The control qubit is always the qubit being driven in a CR-based gate. This also means a CR control scheme requires individual drive lines to each qubit in most practical situations. Clearly a CR drive sent to a common drive line would induce strong Rabi oscillations in the target qubit with which it was on resonance regardless of the state of the control qubit, though the cross resonance effect would still be present at a much reduced relative strength.

4.2 Cross resonance in superconducting systems

Following [99, 27] and basic ideas from Chapter 2 we can write the system Hamiltonian in the lab frame as,

$$H/\hbar = \frac{1}{2}\omega_1\sigma_1^z + \frac{1}{2}\omega_2\sigma_2^z + J\sigma_1^x\sigma_2^x, \tag{4.1}$$

where $\sigma_i^{\{x,y,z\}}$ are the Pauli spin operators and the resonator energy has been neglected. Throughout this chapter, Q2 will be used as the control qubit and Q1 will always be the target. The notation in places will be $|Q2, Q1\rangle$. Similarly, Pauli operators indexed with 1 and 2 refer to operations on Q1 and Q2, respectively. J in Eq. (4.1) is the always-on resonator-mediated coupling strength between the two qubits. The analytic expression for J, neglecting higher levels of the transmon, is [74]

$$J = \frac{g_1 g_2}{2}(1/\Delta_1 + 1/\Delta_2), \tag{4.2}$$

where g_i is the coupling strength of qubit i to the resonator and Δ_i is the detuning between qubit i and the resonator frequency. This Hamiltonian can be diagonalized, resulting in a slight qubit frequency shift $\tilde{\omega}_{\{1,2\}} = \omega_{\{1,2\}} \pm J/\Delta$, where $\Delta = \omega_1 - \omega_2$ is the detuning between the qubits. The key to the cross-resonance effect is a σ_x drive on a designated target qubit with a sign dependent on the state of the other qubit,

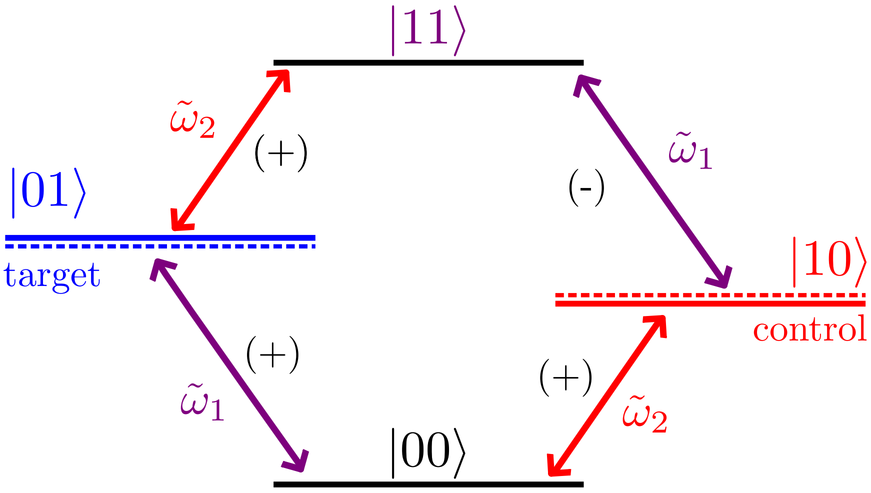

Figure 4-1: Cross-resonance energy levels. Energy level diagram for the cross resonance interaction. The undressed energy levels for $|01\rangle$ and $|10\rangle$ are represented by dashed lines and the dressed states corresponding to $\tilde{\omega} = \omega \pm J/\Delta$ are indicated by the solid lines. With the control qubit in the $|1\rangle$ state (red), a drive at $\tilde{\omega}_1$ incident on the control qubit induces rotations in the target qubit's Bloch vector in a direction opposite to rotations induced when the control is in the $|0\rangle$ state. This rate is recuded by a factor of J/Δ from a resonant dirve. Reproduced from Chow et al. [27].

as in Figure 4-1. To see this, we can write the Hamiltonian when qubit drives are present,

$$H/\hbar = \frac{1}{2}\omega_1\sigma_1^z + \Omega_1\cos(\omega_1^{rf}t + \phi)\sigma_1^x + \frac{1}{2}\omega_2\sigma_2^z + \Omega_2\cos(\omega_2^{rf}t + \phi)\sigma_2^x + J\sigma_1^x\sigma_2^x, \quad (4.3)$$

where Ω_i and $\omega_i^{rf}/2\pi$ are the amplitude and frequencies of the drives on qubit i; $\omega_i/2\pi$ are the qubit ground-to-excited transition frequencies of qubit i and $J/2\pi$ is the transverse exchange coupling strength in the absence of driving. Assuming the detuning between qubits is much larger than their linewidth and making the rotating wave approximation, this Hamiltonian can be taken through a series of unitary transformations (see [99]) to highlight the nonlocal dynamics. The remaining terms oscillate rapidly unless certain drive conditions are met. Chief among these is $\omega_1^{rf} \to \omega_2$. In a frame rotating at the qubit and drive frequencies, a static term develops [99]

$$H_{\rm DF}^{\rm eff}/\hbar = \frac{\Omega_1 J}{4\Delta}(\cos\phi_1 \sigma_1^z \sigma_2^x + \sin\phi_1 \sigma_1^z \sigma_2^y). \tag{4.4}$$

With a proper choice of phase ϕ and drive time, this term becomes a two-qubit interaction and leads to unitary evolution as $\exp(-i\pi\sigma_1^z\sigma_2^x/4)$[1]. To shorten the notation, I will make the substitution $\sigma^x = X$, $\sigma_y = Y$, $\sigma^z = Z$ along with the identity operation I for the Pauli spin operators. A group of two Pauli operators like ZX is shorthand notation for $\hat{Z}\hat{X} = \sigma^z \otimes \sigma^x$, where the first operator operates on the control qubit subspace and the second operates on the target subspace.

In the previous analysis, we have ignored some complicating factors. Given the microwave environment on the chip, a level of crosstalk is unavoidable. A strong drive resonant with the target qubit frequency will leak onto the chip and be sensed by the target qubit independent of the state of the control qubit. In practice, this value is on the order of the drive felt by the target qubit. This leads to an IX term involving Rabi rotations of the target qubit that are independant of the state of the control qubit. A second complication comes from the control qubit being driven strongly off resonance. This leads to an ac-Stark shift ZI term [33] in the drive Hamiltonian. The effective Hamiltonian when the system is driven becomes

$$H_{eff}/\hbar = \epsilon(t)(ZI + (m-\nu)IX + \mu ZX), \tag{4.5}$$

including the ac-Stark shift term, an IX crosstalk term and the CR term from (4.4). In the case of ideal two-level qubits, $\mu = J/\Delta$. In general, the crosstalk term has a quantum and classical component. The ν parameter quantifies the amount of quantum crosstalk during the drive and m quantifies the classical component. In this chapter, I will forgo any analysis on the ν or m parameter and focus instead on μ and

---

[1] More generally, the interaction can be written $\exp(-i\beta\pi\sigma_1^z\sigma_2^x/4)$ with a parameter $\beta = \Omega_1\omega_{xx}t/2\pi\Delta$ where Δ is the qubit-qubit detuning.

the effects of the higher energy states in the transmon. As noted elsewhere [33], these interactions do not degrade the conditional CR term ZX, as these terms commute.

4.3 Higher-Level Effects

The transmon qubit is not a perfect two-level system as we assumed in the last section. In reality, the transmon is a weakly anharmonic oscillator with many other eigenstates besides the computational subspace $\{|g\rangle, |e\rangle\}$. Leakage out of the computational subspace is a continual problem in transmon qubits. Luckily, this particular kind of leakage can be suppressed using a pulse-shaping technique derived from optimal control theory called DRAG, or derivative removal via adiabatic gate [85]. This technique can reduce leakage errors by an order of magnitude. Regardless, the anharmonicity of the transmon qubit sets the ultimate speed limit for gate times. As the inverse of the gate time $1/\tau$ approaches the qubit anharmonicity, the pulse develops frequency components resonant with transitions to the second excited state of the qubit.

Higher-level states can also be used to construct two-qubit gates within the computational subspace. In Ref. [8], these higher levels can be brought near resonance with each other and one qubit can acquire a phase that is dependent on the state of the other. These higher levels will appear in a quite different role in the cross-resonance gate. To model this dependence, we study the transmon with first-order perturbation theory, modeling the qubit as a Duffing oscillator [63]. The Duffing oscillator is a convenient model for an anharmonic oscillator, starting with a harmonic oscillator and adding a quartic perturbation.

The Duffing oscillator can be written in terms of creation and annihilation operators for this anharmonic oscillator [63]

$$H_{\mathrm{Duff}}/\hbar = \omega_{ge}(\hat{b}^\dagger \hat{b}) - \frac{E_C}{12}(\hat{b} + \hat{b}^\dagger), \tag{4.6}$$

where ω_{eg} is the frequency difference between the ground and first excited state and E_C is the qubit charging energy. For two qubits modeled as Duffing oscillators and coupling strength J, the Hamiltonian can be written as [2]

$$\hat{H}_{\text{sys}} = \hbar\left[\tilde{\omega}_1\hat{b}^\dagger\hat{b} + \frac{1}{2}\delta_1\hat{b}^\dagger\hat{b}(\hat{b}^\dagger\hat{b}-1)\right] + \hbar\left[\tilde{\omega}_2\hat{c}^\dagger\hat{c} + \frac{1}{2}\delta_2\hat{c}^\dagger\hat{c}(\hat{c}^\dagger\hat{c}-1)\right] + \hbar J(\hat{b}\hat{c}^\dagger + \hat{b}^\dagger\hat{c}). \quad (4.7)$$

Here δ_i is the anharmonicity of the ith qubit. $\{b, c\}$ and their conjugates represent ladder operators on the individual qubits. A drive Hamiltonian in the two-qubit case

$$\begin{aligned}\hat{H}_{\text{cont}} &= \epsilon_1(\hat{b}+\hat{b}^\dagger) + \epsilon_2(\hat{c}+\hat{c}^\dagger)\\ &= H_1 + H_2\end{aligned} \quad (4.8)$$

is added to Equation (4.7) while a cross-resonance drive is applied. In a qubit system, it is much more convenient to work in the energy eigenbasis and take this as the computation basis. Treating J as a perturbation to second order and truncating Equation (4.3) at the first excited level for each qubit, we find [126, 2]

$$\begin{aligned}\hat{H}_{\text{sys}} = &\left[\omega_2 - \frac{J^2}{\Delta}\right]|01\rangle\langle 01| + \left[\omega_1 + \frac{J^2}{\Delta}\right]|10\rangle\langle 10|\\ &+ [\omega_1+\omega_2+\zeta]\,|11\rangle\langle 11|,\end{aligned} \quad (4.9)$$

where $\zeta = \frac{2J^2(\delta_1+\delta_2)}{(\Delta+\delta_1)(\Delta-\delta_2)}$, and more importantly, the traditional drive Hamiltonians become

$$H_1 = \begin{pmatrix} 0 & -\frac{J}{\Delta} & 1 & 0 \\ -\frac{J}{\Delta} & 0 & 0 & 1 \\ 1 & 0 & 0 & J\left(\frac{1}{\Delta} - \frac{2}{\delta_1+\Delta}\right) \\ 0 & 1 & J\left(\frac{1}{\Delta} - \frac{2}{\delta_1+\Delta}\right) & 0 \end{pmatrix} \quad (4.10)$$

and

$$H_2 = \begin{pmatrix} 0 & 1 & \frac{J}{\Delta} & 0 \\ 1 & 0 & 0 & \frac{J(\delta_2+\Delta)}{\Delta(\Delta-\delta_2)} \\ \frac{J}{\Delta} & 0 & 0 & 1 \\ 0 & \frac{J(\delta_2+\Delta)}{\Delta(\Delta-\delta_2)} & 1 & 0 \end{pmatrix} \tag{4.11}$$

with the matrices ordered in the two-qubit subspace as $\{|00\rangle, |10\rangle, |01\rangle, |11\rangle\}$ [126] and the subscript corresponds to which qubit is being driven, or equivalently which qubit is being used as the control. Here we clearly see the cross-resonance effect. Looking at H_2 there are now matrix elements that drive both Q1 and Q2 with the elements on Q2 being different depending on the state of qubit 1: J/Δ and $J(\delta_2 + \Delta)/\Delta(\Delta - \delta_2)$. In the limit $\delta_2 \to \infty$, the states rotate in completely opposite directions, while as $\delta_2 \to 0$, both states rotate in the same direction giving no conditional operation [2]. Here one can see the higher qubit levels entering to first order as δ_1 and δ_2 in the elements of H_1 and H_2.

We can recover the ZX prefactor μ in Eq. (4.5) for a drive on Q2 at the Q1 transition frequency by looking at the difference in H_2 matrix elements representing the transitions we are interested in

$$\langle 10|H_2|11\rangle - \langle 00|H_2|01\rangle = 2\frac{J}{\Delta}\frac{\delta_2}{\Delta - \delta_2}, \tag{4.12}$$

which corresponds to the difference of the effective Hamiltonian acting on the system with the control qubit in the $|1\rangle$ and $|0\rangle$ states, respectively. The anharmonicity δ for a transmon is negative by definition. If the negative signs absorbed into Eq. (4.5). Half this rate difference is μ which controls the participation ratio of the CR term in the dynamics

$$\mu = \frac{J}{\Delta}\frac{-\mid \delta_2 \mid}{\mid \delta_2 \mid + \Delta}. \tag{4.13}$$

This arrangement corresponds to Q2 being used as the control qubit and Δ is the detuning between the two qubits. This is the quantity we would like to measure. The ν parameter can be calculated from this theory in a very similar way by adding the matrix elements instead of subtracting them: $\langle 10|H_2|11\rangle + \langle 00|H_2|01\rangle = 2\frac{J}{\Delta}\frac{\Delta}{\Delta-\delta_2}$.

4.4 Cross-resonance rates vs. detuning

From equation (4.13) we expect to see a divergence in the parameter μ at frequencies of $\Delta = 0$ and $\Delta = \delta_2$. In this case we have chosen to use Q2 as the control qubit throughout the rest of this chapter[2]. To measure μ vs. detuning, we need to use a tunable qubit of some kind to allow for experimental control over Δ. This is in contrast to a typical CR control scheme where typically fixed-frequency qubits are employed. While CR can definitely be driven using tunable qubits, one of the key advantages of the CR control scheme is that fixed-frequency qubits are insensitive to flux noise. These qubits are made with a single Josephson junction instead of the traditional split junction SQUID arrangement. Due to the prevalence of flux noise in superconducting qubit systems, fixed-frequency qubits can have much improved T_2 dephasing times compared to tunable qubits away from the flux-insensitive sweetspot. One of the key motivations of this chapter is to explore the parameter space of detuning to inform the fabrication of future, fixed-frequency qubit systems.

4.4.1 Experimental setup

To investigate the variation of μ with detuning, we cooled a three-transmon system in a dilution refrigerator to a temperature of 10 mK in a BlueFors dilution refrigerator. The chip is very similar to the device used in [29] with the exception that here the center qubit is a flux-tunable transmon, where the device in [29] was made with all fixed-frequency qubits. A picture of the chip is shown in Figure 4-2 along

---

[2] The dynamics are symmetric in the case the control and target are swapped

with a diagram of the measurement. The central block structures are the transmon qubits. Each qubit {Q1,Q2,Q3} is capacitively coupled to its own CPW resonator {R1,R2,R3} that is used for individual control and readout. A subsection of the chip was selected to study the CR effect vs. detuning. Q1 was fabricated as a traditional split-junction transmon and was designated as the target qubit throughout the experiment. Q2 was a fixed-frequency qubit and was designated as the control qubit. This allowed the frequency of Q1, ω_{ge}^{Q1}, to be tuned both above and below that of Q2, ω_{ge}^{Q2}. The remaining parts of the circuit were unused and unmeasured in this series of experiments. Measurements presented in this chapter were taken during an extended stay at Raytheon BBN Technologies in Cambridge, Massachusetts.

Pulsed spectroscopic measurements were made of all cavities and qubits using an autodyne scheme [107] that corrects for spurious phase jumps produced by the microwave generators. This is accomplished by splitting the microwave source used for the measurement tone and using one of the signals as the LO for signal demodulation. The demodulation scheme is described in Section 3.2. A set of custom arbitrary waveform generators allowed precise pulse shaping for both qubit manipulation and cavity measurement. In this case, both the phase and the amplitude of the pulse is under the control of the experimenter. This allows for precise single-qubit gates around arbitrary axes and was necessary for quantum process tomography and randomized benchmarking in Section 4.5. It also allows additional microwave isolation techniques like single-sideband modulation with a mixer to be used. Additionally, short pulses on the order of 10 ns could be produced, thus removing one of the experimental constraints from Chapter 3, and more sophisticated pulse shapes [85] could also be used.

Resonator fundamentals were $\omega_{R1}/2\pi = 6.5882\,\text{GHz}$, $\omega_{\text{R2}}/2\pi = 6.6905\,\text{GHz}$, $\omega_{\text{R3}}/2\pi = 6.7190\,\text{GHz}$ and linewidths $\kappa_{\text{R1}}/2\pi = 0.398\,\text{MHz}$, $\kappa_{\text{R2}}/2\pi = 0.443\,\text{MHz}$, $\kappa_{R3}/2\pi = 0.2845\,\text{MHz}$. R3 was measured initially, although it was unused in this experiment. Two bus resonators, B1 and B2, connect Q2 to Q1 and Q1 to Q3, respectively. These

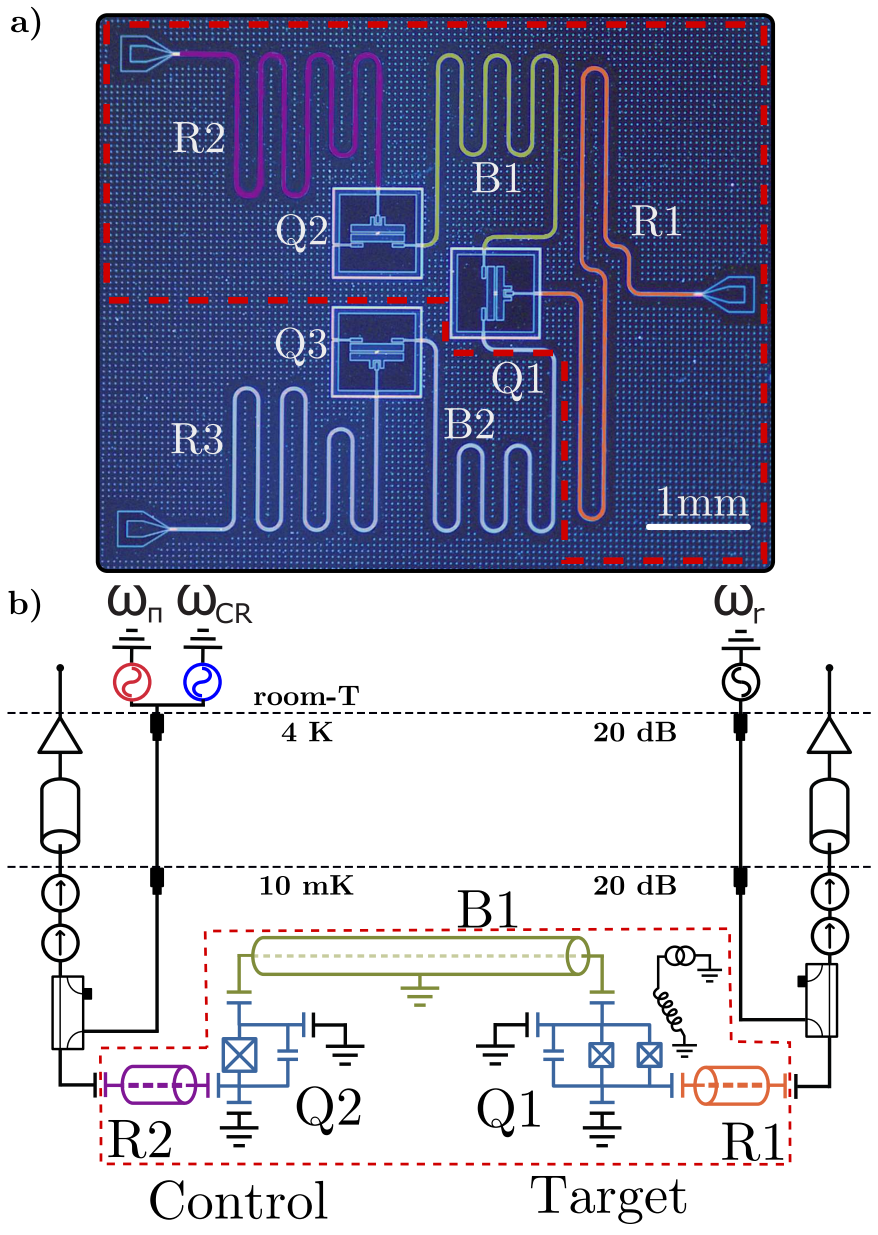

Figure 4-2: Chip and measurement diagram. **(a)** is an optical micrograph of the device with false color, highlighting the qubits and resonators used in the experiment. $Q3$ as measured but not used in the experiment. **(b)** Circuit schematic. Qubit drive and resonator measurement tones are sent to the resonators through directional couplers and back out of the system through a series of isolators before being amplified by a HEMT at the 3 K stage. A flux bias was applied to Q1 through an off-chip flux bobbin.

resonators were unmeasured on this device as there are no direct connections to them, but they were designed to resonate at $\omega_r/2\pi = 8.0\,\mathrm{GHz}$.

The states of Q1 and Q2 were read out by sweeping through a second pulsed microwave tone while probing the state of R1 and R2 near their fundamental resonant frequency. This is done in the dressed dispersive regime, as discussed in Section 2.4.2. Q2 and Q3 transition frequencies were found at $\omega_{ge}^{Q2}/2\pi = 4.349\,\mathrm{GHz}$ and $\omega_{ge}^{Q3}/2\pi = 4.3435\,\mathrm{GHz}$, with Q3 not being used in the experiment. The anharmonicity of Q2 was measured to be $\delta_2/2\pi = (\omega_{ef}^{Q2} - \omega_{ge}^{Q2})/2\pi = -360\,\mathrm{MHz}$, which will be important later as μ is a function of δ_{Q2}. When flux Φ is applied to the SQUID loop of Q1, its transition frequency follows Eq. (5.1). The frequency dependence on flux is shown in Figure 4-3. A flux-insensitive sweet spot at $\omega_{ge}^{Q1}/2\pi = 5.786\,\mathrm{GHz}$ and an anharmonicity $\delta_1/2\pi = -347\,\mathrm{MHz}$ was observed. The modulation allows ω_{ge}^{Q1} to be adjusted to various detunings around ω_{ge}^{Q2}. We extract a qubit-qubit coupling $J/2\pi = 1.08\,\mathrm{MHz} \pm 0.1\,\mathrm{MHz}$ by tuning the qubits on resonance with each other and observing their anticrossing in spectroscopy [74] (Figure 4-3).

The coherence properties of Q1 and Q2 were measured using time-domain measurements (see Section 2.6). Energy relaxation times of $T_1^{\mathrm{Q2}} = 57\,\mu\mathrm{s}$ for Q2 and $T_1^{Q1} = 50\,\mu\mathrm{s}$ on average were measured. Here the average value of T_1^{Q1} is the rough average over the frequency space of the experiment. In general, T_1 will vary slightly over time as well. Phase coherence times for the qubits were $T_2^* = 7.8\,\mu\mathrm{s}$ for Q2 and $T_2^* = 2.8\,\mu\mathrm{s}$ for Q1 on average in the parameter space where the data was taken. The phase coherence of the transmon will be a function of frequency in the same fashion as T_1 as the microwave environment will be frequency-dependent, but it will also depend on the flux bias. A steeper $\partial f/\partial\Phi$ curve implies increased sensitivity to flux noise. This process will be explored in greater detail in Chapter 5. The significantly shorter T_2^* times can be explained by a mixture of charge noise and flux noise. Q2 is a single-junction transmon and was not sensitive to flux noise, but its E_J/E_C ratio of 18.5, while still in the transmon regime, is rather close to the charge qubit regime [63].

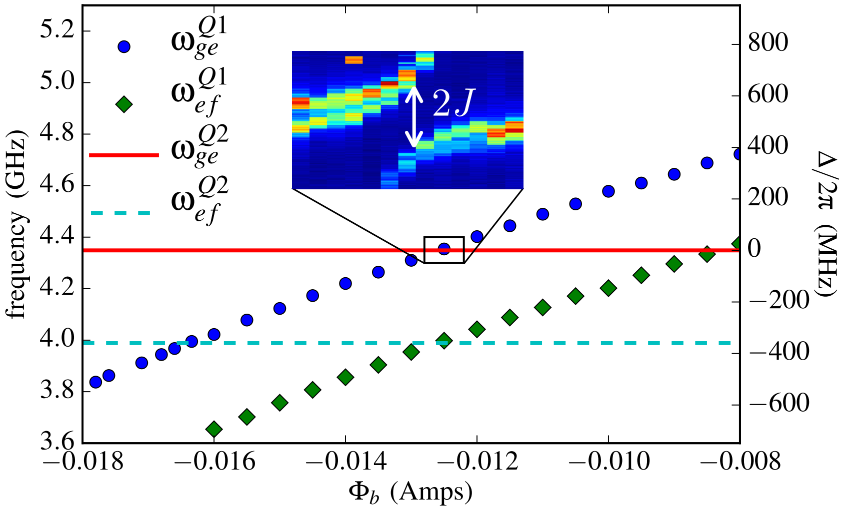

Figure 4-3: Flux spectroscopy. Spectroscopy showing the flux-modulation of the tunable qubit (Q1) above and below the fixed-frequency qubit (Q2). The inset shows the avoided crossing between the two qubits. From this we extract a $J/2\pi$ coupling of 1.08 MHz between the qubits. Blue dots and green diamonds mark the transition of the first and second excited states of Q1. Red and teal lines mark the same for Q2. The right axis shows the relative detuning between the qubits.

In addition, a charge splitting of 400 kHz was observed on the qubit peak in spectroscopy, which indicates the presence of two partially distinct charge states. For Q1, with a slightly smaller E_C and flux tunability, the most likely source of dephasing is flux noise since the qubit was operated away from its sweetspot, although this does not rule out another source of dephasing for this qubit that limited T_2^*.

4.4.2 Cross-resonance data

With the system parameters mapped out, we are in a position to begin measuring the cross resonance effect. The process begins by setting the flux bias Φ to a fixed value and finding the qubit transitions with spectroscopy. The CR effect is very sensitive to the frequency of the CR tone. This means having a good measurement of the target qubit ground-to-excited transition is important. To achieve this, further tuneup is usually necessary. Once a rough estimate of the frequency is determined, Rabi oscillation experiments might be necessary to help hone in on the true frequency. A scan for Rabi experiments vs. frequency will yield a plot similar to Figure 3-6, where the true resonance is the slowest oscillation frequency. In the data presented here, a further tuneup was used involving repeated Ramsey fringe experiments [96] vs. the Q1 drive frequency. For a drive at the true qubit transition frequency in this measurement, the Ramsey fringe will disappear and the time trace will look like an exponential decay. This comes from the fact that the fringe frequency is equal to the detuning between the drive and the transition frequency and the Bloch vector is prepared at the same point on the equatorial plane. Only slow diffusion of the vector in the plane is measured. The fringes never completely disappear due to the charge splitting of this qubit. See Section 2.6 for discussion of these types of measurements. A qubit transition frequency was found with a typical accuracy of ±200 kHz using this method.

Once all the system frequencies were determined, some additional pulse calibration and microwave calibration were completed quickly. π and $\pi/2$-pulses were tuned up via repeated application and measurement cycles. $2N$ π-pulses should produce the ground state $|0\rangle$ for all N and $4N$ $\pi/2$-pulses should do the same. This process magnifies small errors in the pulse, which can be corrected for in an automated process. The CR experiment was then carried out by applying a set of Rabi-like pulses to the control qubit. Microwave calibration involved checking and adjusting frequency-dependent tuning parameters. In particular, the microwave IQ mixers used in the creation of control pulses need to be recalibrated at different frequencies. Even temperature variations in the room can cause drift in these components.

As shown in Figure 4-4, this involves a CR pulse at the target qubit (Q1) frequency applied to the control qubit (Q2). After some time τ, the state of the target qubit is read out. Immediately following this, a second pulse sequence is created identical to the first except it is placed between two π-pulses at the control qubit frequency. This, ideally, sets the control qubit in its $|1\rangle$ state for the duration τ, and is returned to the ground state by a second π-pulse at the end of the sequence.

To extract the value of μ, we also need to vary the magnitude of the drive strength ϵ. This will quantify how the ZX term varies relative to the total drive Hamiltonian (4.4). Data from a single detuning point is plotted in Figure 4-5. Clearly the frequency of oscillations are different in both cases, but recall that the oscillations are not due only to the CR effect. The cross-talk term accounts for a significant fraction of the oscillations.

4.4.3 Analysis

For each drive power, the two different traces are individually fit to an exponentially damped sinusoid model via a least-squares method. This process is aided by a frequency estimation process to obtain starting points for the fits [119]. The fit returns the frequency for each drive power and each control-qubit state. We define

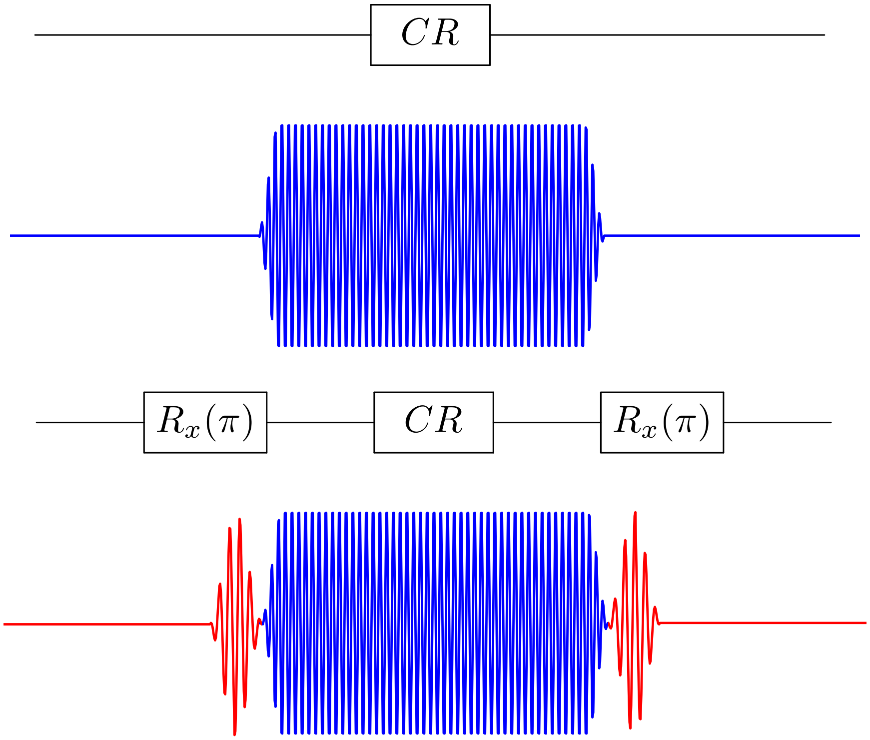

Figure 4-4: Cross resonance pulse sequence. The top pulse sequence shows the cross-resonance drive when the control qubit is not excited. The lower pulse sequence shows the cross-resonance drive gated by π pulses on the control.

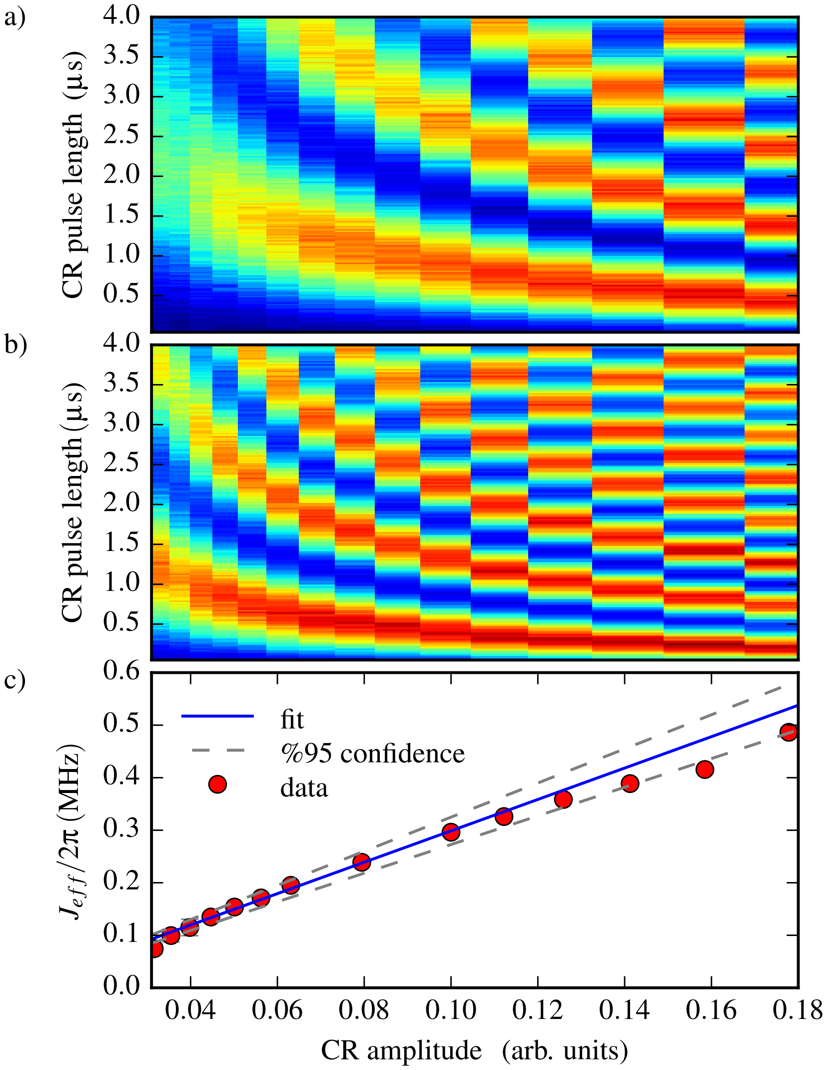

Figure 4-5: Cross-resonance density plots. **(a)** and **(b)** show the Rabi oscillations of the target qubit vs. power for the cases with no π pulses and with π pulses respectively. For this particular case, $\Delta = -78\,\mathrm{MHz}$. The x-axis is a simple linear scale for the increasing amplitude of the CR pulse. Oscillations occur at different frequencies for the two cases. **(c)** plots the frequency difference, J_{eff}, in the two cases with the no-π-case subtracted from the π-case.

the effective coupling strength J_{eff} as

$$J_{\text{eff}}/2\pi = \frac{f^{\pi}_{\text{Rabi}} - f_{\text{Rabi}}}{2}, \tag{4.14}$$

As noted earlier, J_{eff} is half of the difference in the Rabi frequency since the CR contributions to the oscillations act with different signs depending on the state of the control qubit. The values of $J_{\text{eff}}/2\pi$ are plotted vs. CR drive amplitude in (c) of Figure 4-5 for $\Delta = -78\,\text{MHz}$. Finally, the μ value is extracted by performing a linear fit to the low-power region of the trace. To help quantify the uncertainty in the extracted μ value, we calculate standard 95% confidence intervals on the fit lines for each bias point. This was accomplished in a Frequentist framework using bootstrap methods in MATLAB using the *nlparci* method. Additional J_{eff} vs. amplitude traces are plotted in Figure 4-6. The three traces illustrate the dependence of the linear slope μ on detuning. The Δ = -78 MHz case displays relatively fast CR where the Δ = -130 MHz data point is significantly slower. The Δ = 55 MHz trace also shows the change in sign of the CR effect at positive detunings. In general, the value of μ depends strongly on Δ.

Eventually, as drive power is increased, J_{eff} saturates and can not be driven faster due to leakage to higher levels of the transmon. This saturation power describes the fastest the CR interaction can be driven at a particular detuning. Another interesting feature appears after the trace saturates: the J_{eff} briefly decreases towards zero before recovering. This characteristic was observed at all detunings for which a saturation in J_{eff} was observed. Similar behavior was observed in numerical simulations by our collaborators [59] but was very sensitive to the choice of parameters, so direct comparison between simulations and experiment is not possible. At this point, this feature is unexplained, though given the level structure of the transmon, its plausible that dynamics are happening between the levels outside the computational subspace. To compare the theory Eq. (4.13), we need to scale the linear fit values by a value that captures the susceptibility of the control qubit to a drive at a given amplitude.

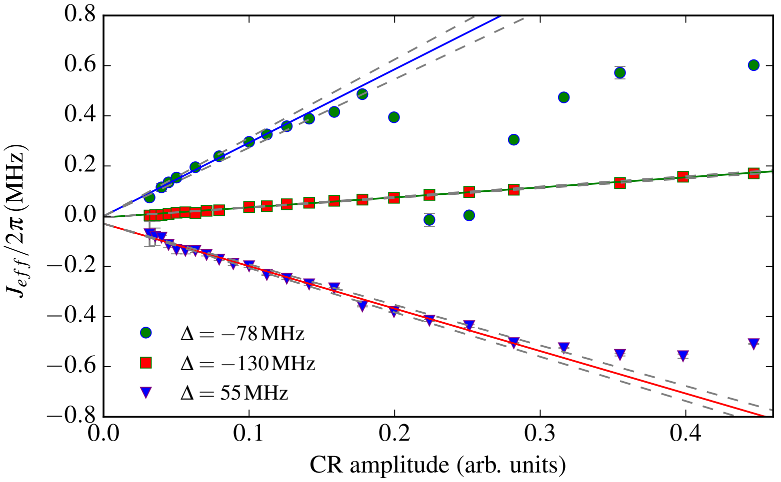

Figure 4-6: J_{eff} vs. drive strength. Plots of J_{eff} vs. amplitude for three selected detunings with fast, slow, and negative CR. Error bars for the points indicate uncertainty in the frequency difference while the dash grey lines indicate 95% confidence intervals.

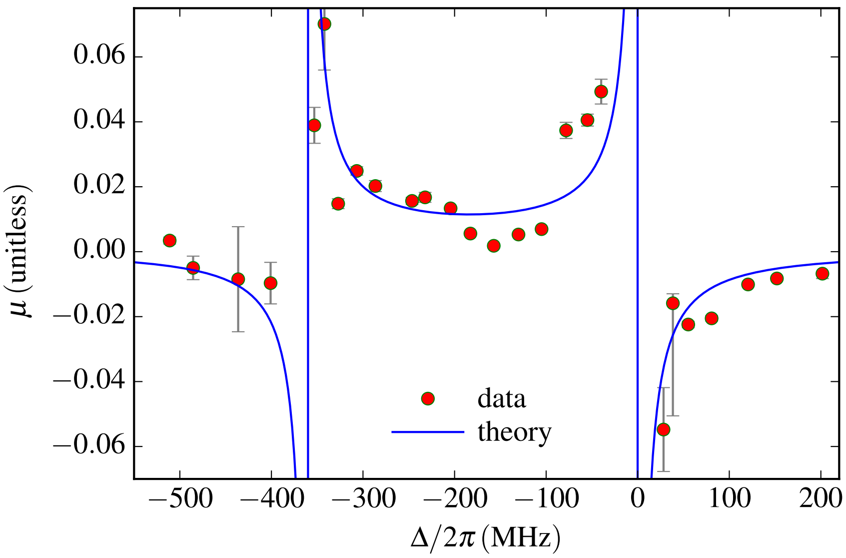

Figure 4-7: CR μ parameter. Plot of the extracted μ values. Error bars are the confidence intervals from Figure 4-6. The theory curve for μ is (4.13) with data scaled by a factor as described in the text.

This could be accomplished by measuring Rabi oscillations on the control qubit when driven with the same microwave drive line and over the same power range. Unfortunately, with the experimental setup this wasn't possible as such a strong drive on resonance with the control quibt's frequency drove Rabi oscillations that were too fast for the down-converting electronics to digitize.

To allow a comparison of Eq. (4.13) with the data, a least-squares analysis was used to fit the data to the theory curve. This process returned a value of 75 MHz/amp to translate the measured μ slopes to unitless data points that can be directly compared to theory. To help justify this fit process and confirm that it returns sensible numbers, we perform a circuit analysis of the drive-line. The analysis models the drive line, amplifiers, on-chip couplings and resonator linewidths. By performing this calculation for the known drive powers used in the π-Rabi experiments, we calculate what the slope of the drive-power/Rabi-rate curve should have been. This process yielded a value of $\sim$100 MHz/amp, within 30% of the fit value.

The measured μ values for each detuning are shown in Figure 4-7, where each data point corresponds to a linear slope extracted from a set of pi-Rabi experiments at that Δ. The data matches the theory reasonably, capturing the expected divergences at $\Delta = 0$ and $\Delta = \delta_2$ as well as the sign changes in the CR rate at the divergences (see Figure 4-7). While the theory captures the qualitative behavior of the data, there are significant deviations in certain areas. These deviations could be explained by spurious, unwanted couplings to microwave chip and slot line modes which form on the chip or in the sample holder. A second source of deviation could come from frequency drift of the tunable qubit. As the target qubit was a symmetric transmon flux-biased on the side of its modulation curve, small drift in the magnetic flux threading the loop could lead to significant shifts in the target qubit frequency. This shift would suppress the CR effect since the resonant drive condition on the control qubit would no longer be met.

Finally, the saturation level of J_{eff} for each data point was extracted and plotted

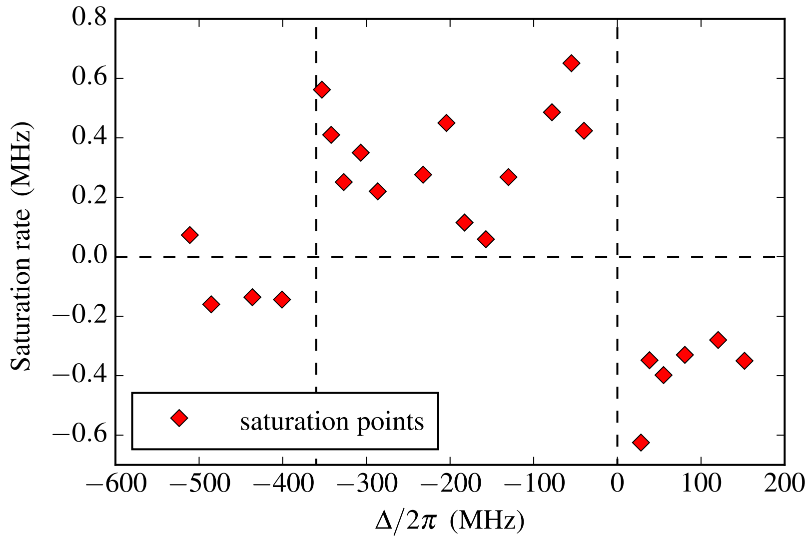

Figure 4-8: CR saturation rate vs. Δ. Dashed lines mark the zero detuning point, the anharmonicity of Q2, and a CR rate of zero.

in Figure 4-8. The values were taken as the highest J_{eff} value before the characteristic decrease in J_{eff} for the J_{eff} vs. amplitude trace at each Δ. Regions near the control qubit 0-1 transition and anharmonicity tend to saturate at the highest rates. In contrast to μ, there is no analytic expression for the saturation rate. This makes quantitative statements about the saturation rate difficult.

4.5 Two-qubit gates with the $ZX_{\pi/2}$

So far in the analysis, we have only been concerned with the speed of the CR interaction. In this section we'll briefly describe how a gate can be made from CR in practice. In addition, we will used one of the gate metrics described in Section 2.6.1 to examine the quality of the gate.

The extra terms in Eq. (4.4) are unwanted in an actual gate implementation. They could be cancelled after the fact by a set of calibrated single-qubit pulses. This would be a brute force approach requiring accurate phase stability between all the microwave electronics. A second tactic involves the spin-echo techniques in the CR sequence [33]. This is the same type of spin-echo technique for measuring T_2 in Section 2.6, the CR gate can be broken in half and the polarity of the unwanted terms flipped in the middle of the sequence. This process is diagrammed in Figure 4-9. The IX term, representing the crosstalk in a CR sequence (see Eq. (4.5)), can be cancelled by flipping the phase of the CR pulse by 180 degrees. This causes any leakage of the CR signal to the target qubit in the first half of the gate to be driven in the opposite direction for the second half of the gate. Ideally, this cancels the contribution from the IX term. In a similar fashion, a π-pulse is applied to the control qubit at the halfway point. This has the effect of flipping the state of the control qubit and the sign of the ZI term for the second half of the gate. Again, this ideally cancels the contributions from this term.

4.5.1 Interleaved randomized benchmarking

The two standard tools for assessing the quality of a gate are quantum process tomography [12, 129, 25] and interleaved randomized benchmarking [62, 25]. These were briefly outlined in Section 2.6.1. Here data of interleaved randomized benchmarking for a CR-based two-qubit gate is presented [35, 71, 73, 45] for this sample using the Q2 as the control and Q1 as the target just as in the previous sections of this chapter. Randomized benchmarking is accomplished by creating random strings of gates from a gate set to be characterized. This random string is applied to the qubit followed by a final gate which is calculated to be the inverse of the entire random string of gates preceding it. The ground state of the system is typically chosen as the starting point for a benchmarking sequence. This process ideally leaves the system unchanged as the whole process should be equal to an identity operation, which does nothing to the system. Strings with different numbers of gates are applied and the fidelity F of the identity operation is measured. Because the gates are not perfect, errors will accumulate over time, leading to an exponential decay of the overlap between the

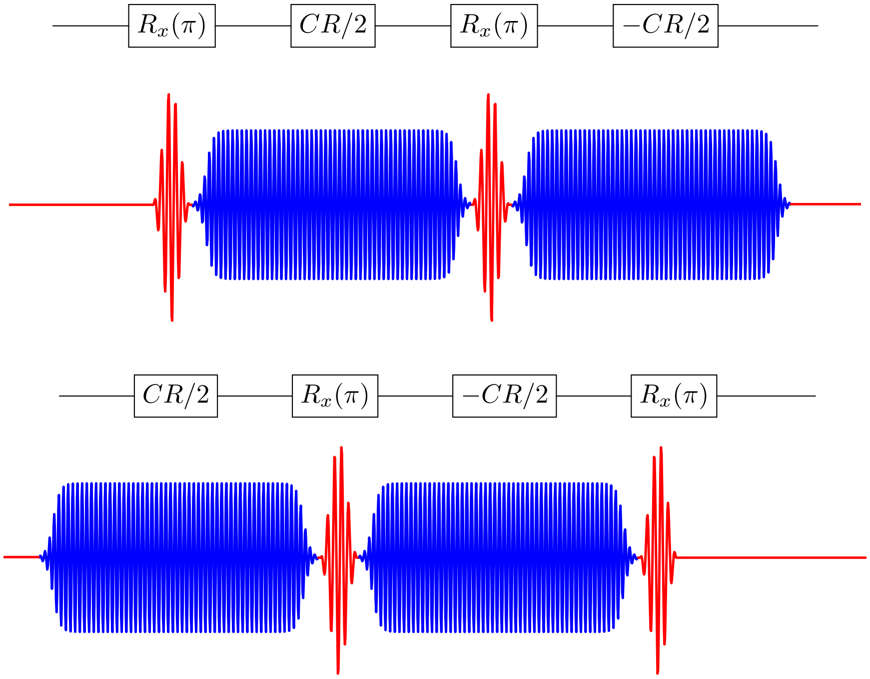

Figure 4-9: Echo cross resonance pulse sequence. The top sequence corresponds to exciting the control qubit and executing an echo CR sequence. The lower sequence starts with the control in its ground state. Here the CR pulse is broken into two parts with a control qubit π-pulse in the middle. By flipping the state of the control qubit and the phase of the CR drive, the unwanted single-qubit terms in the effective drive Hamiltonian are echoed away.

initial and final state. As the errors accumulate, the state is driven further from the ground state. This envelope can be fit with a model [33]:

$$F(i, |00\rangle) = A\alpha^i + B, \tag{4.15}$$

where A and B are constants are related to state-preparation and measurement errors, F is the sequence fidelity, i is the length of the sequence and α is related to the average error per gate r for *all* gates in the set by the relation $r = 1 - \alpha - (1 - \alpha)/2^n$ for n qubits [33].

This process only measures the average error per gate over the entire gate set. To measure the error on a particular gate, the process has to be modified, as described in Ref. [73, 45], by interleaving the gate to be measured inside the random series of gates. That is, every other gate is the gate of interest. This will produce a decay curve similar to the traditional randomized benchmarking, but with a different decay constant. Figure 4-10 shows a randomized benchmarking experiment with the $ZX_{\pi/2}$ gate interleaved in the sequence. This data was taken at a qubit-qubit detuning of $\Delta =$ 80 MHz. An average of 0.120 errors per gate was measured for the whole interleaved sequence. Figure 4-10 shows data from the interleaved RB experiment. Here only an interleaved sequence was extracted and it was not compared against a standard RB measurement over the Clifford group with out the $ZX_{\pi/2}$ gate. Therefore it is not possible to extract the gate fidelity of the $ZX_{\pi/2}$ gate in particular. Here the Clifford group was chosen because it describes transitions between all the cardinal directions of the Bloch sphere and should sample the noise in all directions. Choosing a random Clifford in a multi-qubit Clifford group scales polynomially [33] and would scale favorably in a multi qubit system.

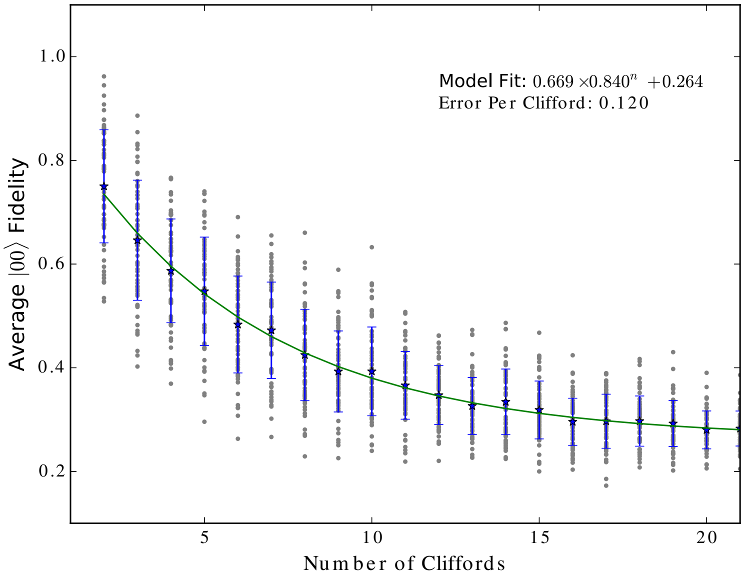

Figure 4-10: Two qubit randomized benchmarking of the $ZX_{\pi/2}$ gate. Interleaved Randomized benchmarking of the $ZX_{\pi/2}$ gate composed using the cross-resonance effect using Q2 as the control and Q1 and the target.[a] The fidelity of the ground state is plotted on the y-axis and the total length of the sequence of gates. The grey dots correspond to individual fidelity measurements and stars noting the average value. The green line is the extracted fit and the error bars are the standard deviation of the measurements for each sequence length.

---

[a] Code generating this plot was generously provided by Colm Ryan.

Chapter 5

Decoherence in asymmetric transmons

5.1 Introduction

In Chapter 2 we presented some state-of-the-art coherence numbers without considering the microscopic and macroscopic sources of dissipation in superconducting systems. Energy relaxation and dephasing are an immensely important topic in superconducting systems. In this chapter we will present an analysis and preliminary data on flux noise as it affects tunable transmons, with different levels of junction asymmetry. In Chapter 3, we saw an asymmetric transmon made of two junctions with significantly different junction critical currents. In both the symmetric and asymmetric case, the two Josephson junctions form a SQUID loop through which magnetic flux can be threaded. This loop makes the transmon sensitive to magnetic flux noise coupled to the loop and translates into variations in the qubit's Josephson energy E_J. This noise in E_J leads to variation in the qubit frequency $\delta\omega_{eg}(t)$, which leads to dephasing of the qubit.

To see the magnetic field's effect on frequency, recall equations (5.1) and (5.2) from Chapter 2 were

$$E_J(\Phi) = E_J^{\Sigma}\cos\left(\frac{\pi\Phi}{\Phi_0}\right) \tag{5.1}$$

for the symmetric case and

$$E_J \to E_J^{\Sigma}\cos\left(\frac{\pi\Phi}{\Phi_0}\right)\sqrt{1 + d^2\tan^2\left(\frac{\pi\Phi}{\Phi_0}\right)} \tag{5.2}$$

for the asymmetric case. Here E_J^{Σ} is the sum of the two Josephson energies and $d = \frac{E_J1 - E_J2}{E_J1 + E_J2}$. Variation in Φ appears in the transmon qubit transition frequency as $\delta\omega_{eg} = \sqrt{8E_C E_J(\delta\Phi, d)}$. The slope of the E_J modulation depends on the static magnetic flux bias. At the sweet spots ,where the derivative of E_J vanishes, the qubit is insensitive to variations in Φ to first order. Away from these points, the $\delta\omega_{eg}$ will depend on the slope of E_J at a particular bias ϕ

$$\delta\omega_{eg} \propto \left.\frac{\partial E_J}{\partial\Phi}\right|_{\Phi=\phi}. \tag{5.3}$$

The slope of the frequency vs. flux curve can be controlled by intentionally varying the d parameter as shown in Figure 5-1. This junction asymmetry can be set at fabrication time by making the area of one junction x times larger than the second junction. The inverse relationship between critical current and junction resistance insures the proper difference in the junction energies E_J. This type of asymmetric transmon was used in Chapter 3 to implement fast photon swaps between a qubit and a cavity. In this chapter we will examine the asymmetric transmon system comparing it more carefully to the traditional transmon system. We'll discuss how increasing d should decrease susceptibility to flux noise. This could be ideal for qubit systems that need some flux tunability, but not as much as the traditional symmetric transmon.

In a Ramsey fringe type experiment, the characteristic decay rate can be written as

$$\frac{1}{T_2^*} = \frac{1}{T_\phi} + \frac{1}{2T_1}, \tag{5.4}$$

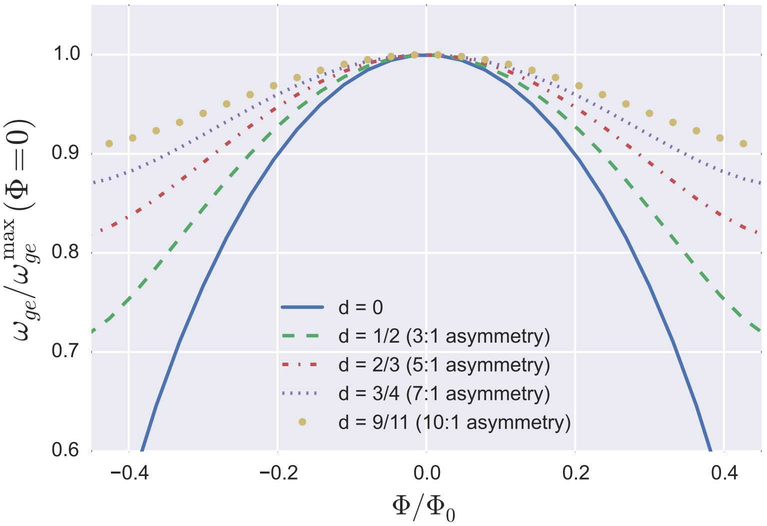

Figure 5-1: Asymmetric frequency modulation. Plot showing the variation of ω_{eg} vs. flux. The x-axis is in units of Φ_0 and y-axis is in units relative to maximum value of $\omega_{eg}^{\max}$ at integer values of Φ_0. The modulation curves fan out as the zeros in E_J seen for the symmetric transmon are removed and replaced by a second flux-insensitive sweet spot at odd half integers of Φ_0. This pattern is periodic in the applied magnetic flux with period Φ_0

where T_1 is the energy relaxation time and T_ϕ is the pure dephasing time. This pure dephasing time is set by variation in the qubit frequency, as noted above. To highlight the role of the dephasing noise, the Hamiltonian describing the qubit can be rewritten as

$$H(t)/\hbar = [\omega_{eg} + \delta\omega(t)]\sigma_z. \tag{5.5}$$

In this chapter, we will focus on magnetic flux noise, though this is not the only source of dephasing in superconducting transmon qubits. One of the qubits in Chapter 4 displayed a small amount (∼400 kHz) of charge noise [101]. Even though this type of noise is exponentially suppressed in a transmon (see Section 2.4.1), as E_J/E_C is reduced, the transmon continuously transitions back to the charge regime for small E_J/E_C [63]. Quasiparticle tunneling describes the process of an unpaired electron (quasiparticle excitation out of the superconducting BCS ground state) tunneling through the junction. This can also lead to qubit dephasing [21]. Unlike Cooper-pairs, normal electron tunneling is also dissipative [94] (energy relaxation). Junction critical current fluctuations due to defect dynamics in the amorphous oxide layer of the junction tunnel-barrier are yet another source of dephasing. Fortunately, the levels of this type of noise have recently been shown [87] to be quite low relative to other sources for state-of-the-art qubits.

The microscopic source of flux noise in these systems is still an intensively researched topic [13, 112]. A characteristic level of flux noise was first measured thirty years ago in dc SQUIDs. At low temperatures, this magnetic flux noise was found to be roughly independent of SQUID loop size [128]. This independence of loop area persisted over a wide range and hinted that the noise source was not a global background field, but some locally produced noise on or around the superconducting electrodes. In recent years, this same level of flux noise has been observed in superconducting qubit systems [131, 13, 80]. This noise is characterized by a roughly $1/f$ spectrum yielding a characteristic noise spectral density of 1 $\mu\Phi_0/\sqrt{\text{Hz}}$ at 1 Hz. Recent experimental studies [112, 113] have pointed to coherent clusters of unpaired magnetic spins on the superconducting surface as a likely source for this magnetic flux noise. Precision measurements of flux noise continue to improve [131, 132, 6], hopefully providing new insight into the microscopic origins flux noise.

As this noise is ubiquitous in superconducting qubit systems and there is currently no known way of mitigating it, some groups have removed flux tunability entirely [27, 29] and focused on systems using two-qubit gates with fixed-frequency qubits [99]. A second approach, taken here, is to reduce the susceptibility of qubit frequency to flux $\partial\omega_{eg}/\partial\Phi$ without removing flux-tunability completely. By increasing the d parameter, the tunability of the system would decrease, but this should also reduce the susceptibility to magnetic flux noise. Ideally this would offer a promising trade off between flux noise versus tunability. Below we will examine this track and show some preliminary results in addition to planned experiments and those currently under way in our lab.

5.2 Future work

As described above, be varying the junction asymmetry in a transmon qubit we should see a reduced susceptibility to flux noise as the modulation curves flatten out (see Figure 5-1). To study this, experiments are underway in our lab to fabricate several transmon qubits with different levels of asymmetry on the same sample. Fabricating a variety of qubit asymmetries on the same chip will help remove any question of variability between measurement runs and samples. We expect to see the magnetic flux noise sensitivity vary in a similar way as the derivative of qubit frequency with respect to flux. This relation is plotted in Figure 5-2. The line of $d = 0$ corresponds to a symmetric transmon with zeros in transition frequency at odd half-integer values of Φ_0. At these points, an asymmetric transmon returns to a point where its derivative vanishes. Clearly as d is increased the slope of the modulations decreases. Figure 5-3 show the relative change in lower sweet spot transition frequency as d is increased.

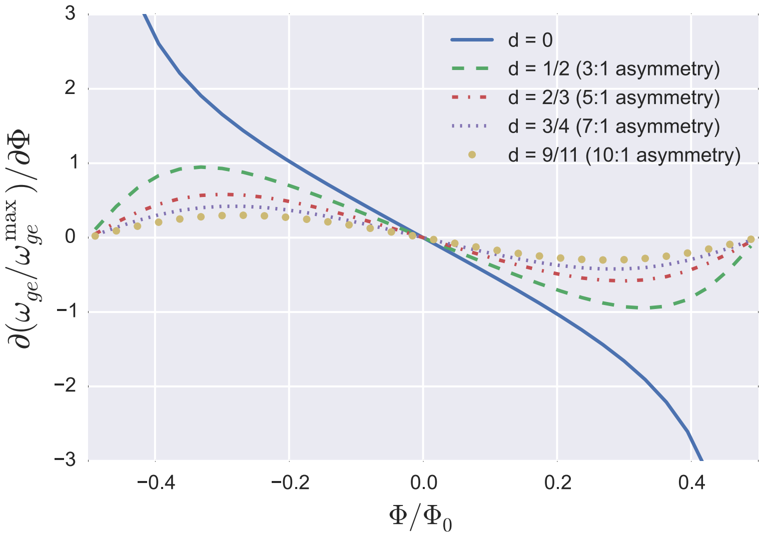

Figure 5-2: Derivative frequency modulation. Plot of the derivative with respect to flux of $\omega_{eg}/\omega_{eg}^{\max}$ for different values of asymmetry. Excursions further from the zero line indicate a higher flux sensitivity.

This plot helps to quantify the loss of tunability as d is increased.

I order to motivate and inform future experiments, we analyze some preliminary data from a chip similar to the sample of Chapter 3. This sample had two asymmetric transmon qubits coupled to a common drive and readout cavity. Coherence data was extracted and is plotted in Figure 5-5. The asymmetry of the qubit was 3:1, giving a modulation depth of close to 3 GHz. A plot of frequency vs. flux is show in Figure 5-4. Here we can see the asymmetric transmon lower sweet spots at multiples of $\Phi_0/2$. These points also corresponds to a significant increase in T_1 and T_2^* shown in Figure 5-5. A similar increase in coherence is not seen at the upper sweet spots of integer Φ_0. This is most likely due to the upper sweet spot's proximity to the cavity resonance frequency $\omega_r/2\pi$, resulting in a limited T_1 due to the Purcell effect. The Purcell effect is observed when a two-level system is placed in a resonant structure nearby in frequency space. If the detuning is small, the structure provides a decay channel for the qubit, enhancing the relaxation rate of the qubit [63]. The

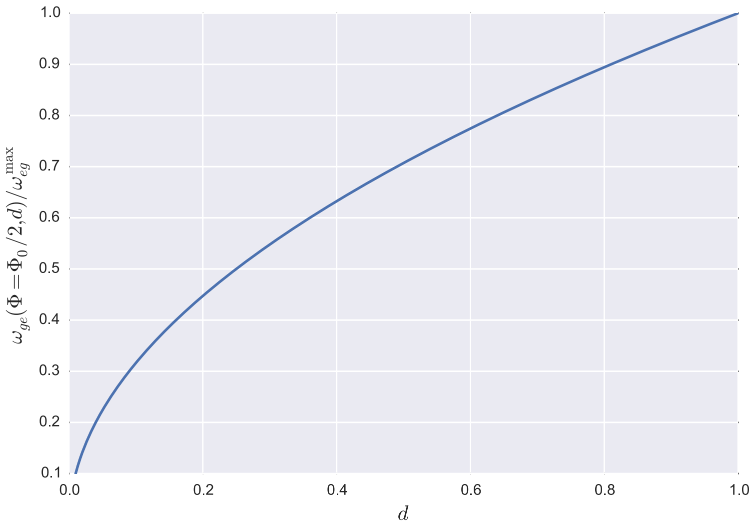

Figure 5-3: Modulation depth of an asymmetric transmon. The normalized qubit frequency at the lower sweet spot ($\Phi = \Phi_0/2$) vs. d. $\omega_{ge}^{\max}$ is undefined at $d = 0$ since the transmon transition frequency diverges. At $d = 1$, the transmon is essentially a single junction transmon with a fixed frequency.

$|1\rangle \rightarrow |0\rangle$ decay rate will have a Purcell contribution of

$$\gamma_{\kappa}^{g,e} = \kappa \frac{g_{ge}^2}{\Delta_0^2}. \tag{5.6}$$

Δ_0 for this sample is close to 1 GHz which is likely limiting the energy relaxation time. It is also possible that higher order Purcell transitions are playing a role in suppressing the T_1 times of the sample. A short T_1 can limit the accuracy for extracting T_ϕ, particularly when pure dephasing is weak. Near the $\Phi/\Phi_0 = 0$ point, T_2^* is essentially T_1-limited, as the upper limit for T_2^* is $2T_1$.

Figure 5-6 shows T_ϕ times for the this chip plotted vs. flux bias. The T_ϕ values are calculated using Equation (5.4) using the measured values for $T1$ and T_2^*. To compare this data to the expected flux noise observed in other studies [128], we can follow the analysis in Yoshihara et al. [130] using extracted parameters from our chip. The qubit energy band can be estimated by interpolating the data in Figure 5-4.

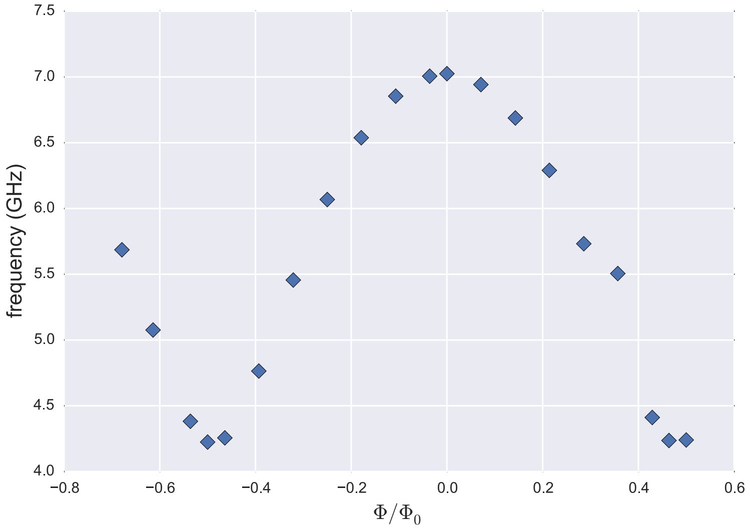

Figure 5-4: Sideband frequency modulation. Plot showing the qubit ω_{ge} vs flux. Flux-insensitive sweet spots appear at integer and odd half-integer values of Φ_0.

The derivative of this function can be calculated and combined with the scheme in Yoshihara et al. [131] to produce the curve in Figure 5-6, assuming a flux noise density of 2 $\mu\Phi_0/\sqrt{\mathrm{Hz}}$. The match is not perfect, but the curve follows the T_ϕ data at least qualitatively. the discrepancy could be due to limitations in applying the flux noise model of Yoshihara et al. to our system or to the rather low T_1 values on this chip.

5.2.1 Coherence study

We have begun designing and testing a new chip design with four transmon qubits all coupled to a common feedline through an individual CPW resonator. This type of design allows for increased isolation for each qubit, as no two qubits are coupled to the same cavity. Additionally, all qubits will be designed to avoid Purcell loss by keeping Δ large and κ small. Flux bias lines will be removed to have avoid over-coupling to the qubit, leading to reduced T_1 times. To accomplish this, new qubit designs used in Chapter 4 and in [29] were adapted for the design. These qubits have

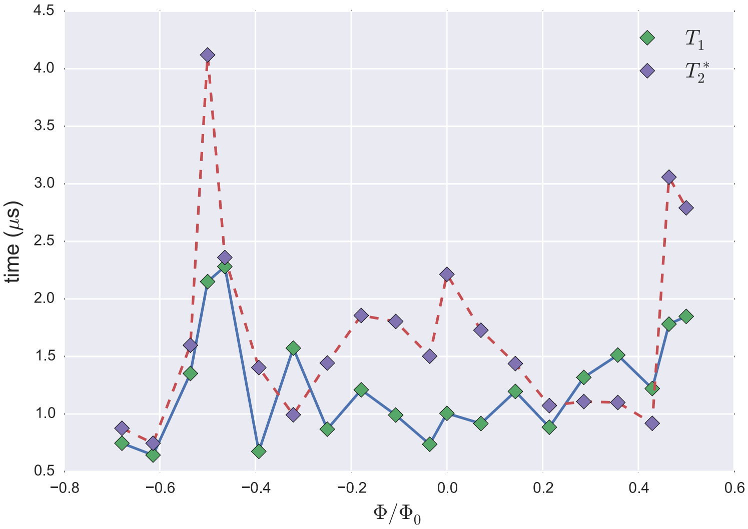

Figure 5-5: Sideband coherence data. Coherence times T_1 and T_2^* for a qubit from the sideband sample from Chapter 3. A sharp increase in coherence is seen near $-\Phi_0/2$ corresponding to a lower flux sweet spot. T_1 and T_2^* times should similarly increase at $\Phi/\Phi_0 = 0$, but is likely suppressed at this upper sweet spot due to Purcell loss into the cavity. At this point, T_2^* is limited by the short T_1 times.

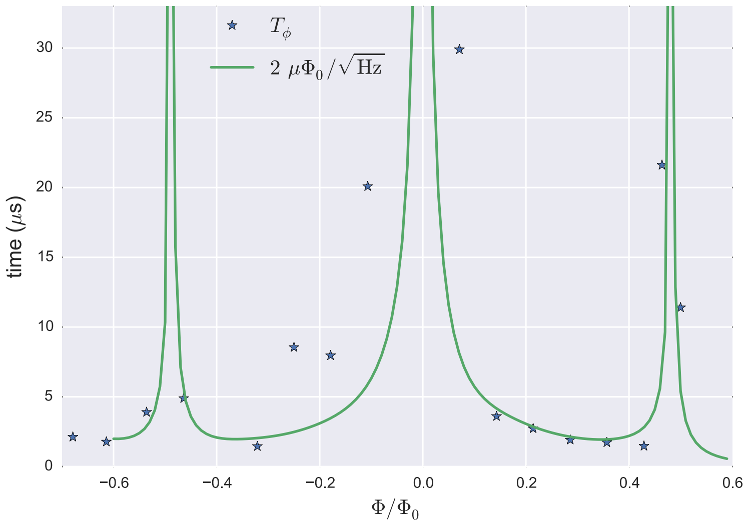

Figure 5-6: Sideband T_ϕ. Calculated T_ϕ times using Equation (5.4) plotted vs. flux bias. A calculated limit set by a flux noise of $2\ \mu\Phi_0/\sqrt{\text{Hz}}$ is also plotted with the data [130], as described in the text. The noise level indicated by this T_ϕ data is consistent with other flux noise measurements [128].

been shown to have long T_1 relaxation times. A picture of the basic device is shown in Figure 5-7. Each cavity is designed to have a slightly different resonant frequency, which allows individual drive and readout. Additionally, this design is compatible with frequency-multiplexed readout [57]. This system will allow direct comparison between qubits with different or no asymmetry.

Measurements on this new chip design will involve measurements of T_1 and T_2^* over the full range of tunability for each qubit. A systematic sweep of T_1 vs. frequency would highlight radiative loss and coupling to other unwanted sources of loss throughout frequency space. This could potentially help identify unknown sources of loss for a particular sample design. The data-taking process for these types of measurements is laborious as there is no robust way to automate sensitive steps in the tune up process. An even more interesting data set would involve a map of T_2^* vs. flux for a variety of transmon asymmetries. Ideally the dephasing time would increase

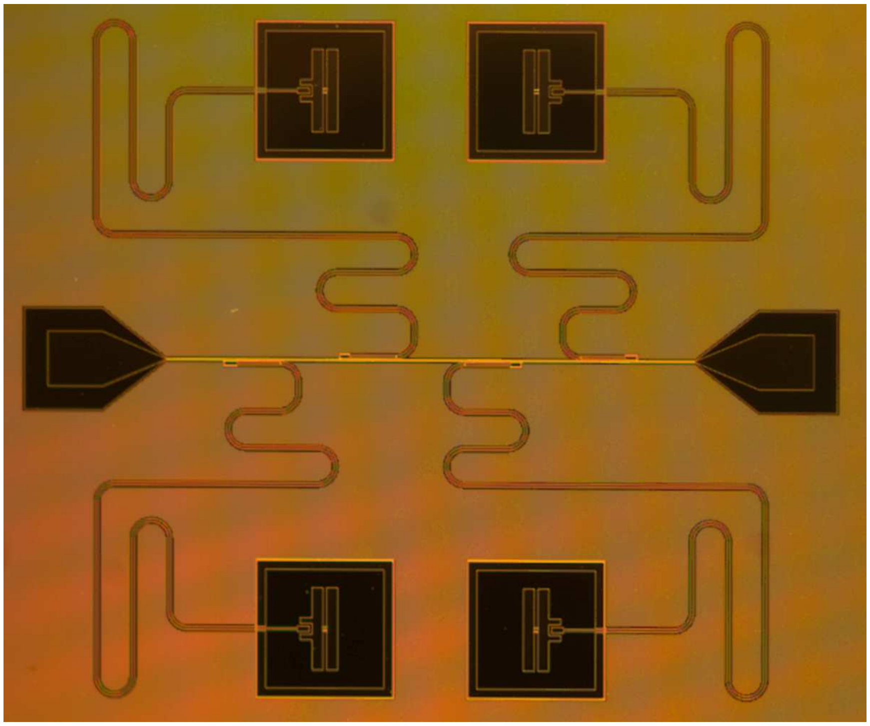

Figure 5-7: Quad asymmetric transmon. Picture of a four transmon device with each qubit coupled through a readout resonator to a common feedline. The new qubit capacitor and coupling design is taken from the chip of Chapter 4. Different amounts of asymmetry are designed to be different for each qubit. Flux will be coupled into each qubit through an external flux bobbin in the device holder. The central line in the device is not a resonator and has no intentional mode structure. Each cavity is designed to have a slightly different resonant frequency which allows individual drive and readout.

by an amount proportional to the decrease in modulation slope (see Figure 5-3) and this could be observed for multiple asymmetries.

This amount of data would likely require automation. This will prove challenging, as Ramsey fringe experiments typically require copious amounts of human intervention to fine tune pulse and system parameters.

Chapter 6

Conclusions

6.1 Outlook

In this dissertation I have presented work using superconducting transmon qubits to study two-qubit interactions. I have shown the flux modulation degree of freedom allows fast swapping of photon excitations between a CPW resonator and a qubit. A flux-tunable transmon was also used to explore parameter space and improve the cross resonance effect for a new round of fixed frequency multi-qubit devices. Finally, we outlined an ongoing experiment to study the coherence properties of asymmetric transmons for different junction asymmetries. Further exploration of sideband interactions could produce fast two qubit gates or fast Fock state creation inside a resonator. A deeper understanding of the cross-resonance effect could lead to faster gate times, higher fidelity gates or new types of qubit gates using higher energy levels for example. Asymmetric transmon qubits could lead to more coherent qubits and more interesting flux-driven dynamics.

Future work will involve carrying out the experiments outlined in Chapter 5 and continuing to study two-qubit interactions. Transmons are currently an appealing style of superconducting qubit for quantum information processing. This may change in the future as work continues to improve multiple realizations of superconducting quantum circuits. The CNOT gate, which can be built using the flux-modulation drive form Chapter 3 and the cross resonance effect from Chapter 4, will continue to be researched heavily due to its importance in scaling qubit systems and controlling the inevitable errors that will occur in these systems. Researchers are now working to implement the basic operations of quantum error detection/correction schemes[29, 34, 8, 102, 72] that use the CNOT gate extensively.

Quantum error correction (QEC) is a process of identifying and correcting errors in qubit systems [42]. QEC borrows many ideas from classical error correction, but must be modified to work with qubits. To work in quantum systems, extra qubits, called ancillary qubits, must be used to detect errors by measuring the state of a qubit used in a computation that would otherwise destroy an arbitrary quantum state and project it onto an eigenstate. Using a CNOT gate between data qubits and measure (ancillary) qubits, it is possible to measure the parity state of a group of qubits to indicate whether a bit-flip error has occurred. This is one of the simplest possible cases of QEC, but the idea scales to general qubit errors and larger systems. The CNOT gate is important in most QEC schemes to help entangle data and ancilla qubits. This includes the surface code [42] which is currently the most experimentally appealing due to its relative high tolerance for gate errors and the requirement for only nearest-neighbor two-qubit interactions. An outstanding goal for scaling qubit systems is to build a logical qubit which is resistant to general errors over an arbitrary amount of time. A logical qubit will be made of many physical qubits using a QEC scheme working to preserve the logical qubit coherence. Many engineering challenges need to be overcome before that device is built, but significant and steady progress is being made on multiple fronts to meet those challenges [34, 61].

For now, in the year 2014, the future for superconducting qubit and superconducting quantum information processing devices is bright indeed. Companies like Google, IBM and numerous defense department contractors are investing heavily in the future of this technology. Recently, a Canadian company, D-Wave, has begun producing and selling a many-qubit device for the purpose of quantum computation. The chips produced by D-Wave also use superconducting qubits, though the computational approach is quite different from the gate-based model that is discussed in this dissertation. The D-Wave device uses a process called quantum annealing to find the ground state configurations of complex Hamiltonians in particular spin models. This model of quantum computation is fundamentally different than gate-based universal quantum computation. It does not allow for the execution of Grover's algorithm or Shor's algorithm.

A quantum annealing process can be used to solve a variety of computationally difficult optimization and machine-learning problems that can be mapped isomorphically onto a two-dimensional lattice of spins. The device works by finding the ground state configuration of the spin system. The current topology of the D-Wave device spins, the so-called Chimera graph, is set at the time the chip is made. Here the Chimera graph describes the arrangement of possible qubit-qubit couplings. This limits the types of problems which can be solved. A more severe limitation is the short coherence times in the current generation of devices. Given the amount of decoherence in the system, there is some skepticism in the research community about the proper model for computation in D-wave devices [114] and how much classical or quantum effects play a role in the observed dynamics. With all this in mind, there has been interesting research accomplished with the D-Wave devices [122]. Future work could be done to lower the noise in these devices allowing the system to exhibit quantum characteristics clearly or to search for a quantum speedup in computational tasks.

Beyond the computational aspect of these projects and proposals, new areas of basic science are being explored with superconducting systems. They have allowed the basics tenets of quantum mechanics to be tested in artificial systems. The decoherence barrier that separates our classical experience and the quantum world is being pulled back, at least in artificial quantum systems. Physicist John Preskill has optimistically hailed the coming "quantum supremacy" [95], which will hopefully prove to be an exciting time for everyone in quantum information science.

Appendices

Appendix A

Device fabrication

A rough outline of the fabrication methods used in our lab at Syracuse was given in the Chapter 1. Here I will fill in the specific details used to make the samples presented in this thesis.

A.1 Circuit Design

Systems built with quantum information processing in mind have several, almost opposing design constraints. We would like the systems to be easily controllable with our classical instruments. To this end, we want to have precise control in the form of microwave drives. These drives are further abstracted to quantum logic gates which are used to build actual algorithms. Ideally we could also measure the state at anytime with perfect fidelity, projecting the system onto one of it's eigen states in whatever basis we happen to measure. At the same time we would like our information processing system to be well isolated from it's environment (and measurement apparatus) so it can remain as coherent as possible. Quantum mechanics precludes a perfect realization of anyone of these three goals. Further, being able to control and discriminate the state well is antithetical to having it well isolated from control and readout devices.

Therefore choosing circuit parameters becomes a task of balancing trade offs between these competing goals. For high fidelity measurement we want to be able to get information out of the system quickly. So we might want couple more strongly to our measurement apparatus. The same argument could be made for the drive side coupling. You might want to change design parameters depending on the goals of any one particular experiment.

A.1.1 Design and Layout

A.1.2 Simulation

Modeling superconducting circuits can save valuable measurement time when it can take a few days to a week to cool these systems to 30 mK. It also typically takes a week or more to iterate on a chip layout. If you can partially hone a design before making and cooling a sample, copious amounts of time can be saved. Though you should keep in mind it it typically difficult to get highly accurate results. This stems from the large parameter space and large number of nuisance parameters such as mesh details, material parameters and boundary conditions that are necessarily part of any realistic electromagnetic simulation.

For simulating capacitance, we typically used *Ansys Q3D* for pulling out a rough number of pF. This value tends to be within 20% the measured value. A frequency domain simulation can be accomplished using *Sonnet* or *Ansys HFSS* though these tend to be tricky to get right as noted above.

A.2 Circuit Fabrication

All devices in this thesis were made in a similar fashion with a two step lithographic process. All metal layers were deposited in dedicated chambers in our lab. This was done to avoid any contaminants or unwanted materials likely to be present in shared metal deposition chamber. All the device layers were patterned and etched at the Cornell Nanoscale Facility on Cornell's campus. The fabrication process was intentionally and consciously kept as simple as possible. All devices were made in two lithographic steps. The first was used to pattern a ground plain, resonators, flux trapping mesh, etc. in a Niobium film. A second layer consisted of the qubit capacitors, resonator coupling capacitors and most importantly Josephson Junctions were written in an electron-beam lithography step. In some ways this final step is the most critical and hardest to reproduce. More details can be found in Section A.2.3. Below is on outline of the fabrication process in the order which the process steps are carried out.

A.2.1 Metal deposition

The fabrication process began with an high resistivity ($> 10{,}000\ \Omega/\mathrm{cm}^2$) 4 inch wafer of Si. This wafer forms the flat substrate for all subsequent processing. Near intrinsic Silicon is used to reduce the ion concentration as the semiconducting properties of doped Si are not necessary in our superconducting circuits. The substrate is loaded into a ultra high vacuum system equipped with multiple RF magnetron sputter guns. The film deposited is set by the target material and the gas chemistry in the chamber. For example, a Niobium target sputtered with Argon will produce a Niobium film (assuming you have a working recipe!). On the other hand, sputtering a Niobium target with Argon and Nitrogen will produce a Niobium nitride film. Clearly I'm glossing over some finer details, but the broad ideas should be clear. A typical deposition process is accomplished with the following steps:

- Pump the chamber to $\approx$ 1e-8 Torr
- To minimize the throw distance, position the substrate 1-2 mm above the lowest possible vertical position. If the wafer holder gets lowered too low, it can rub against the shutter and cause it to become misaligned.
- flow of 60 sccms of Ar is allowed in the chamber and the total pressure is adjusted by throttling the gate valve on the system's cryopump. Set a total

pressure of $6.5e^{-3}$ Torr in the chamber.

- once the pressure has stabilized, turn on the sputter gun power supply and set the power to 250 Watts.
- Set the sputter time based on your calibrated target film thickness. In most cases a rule of thumb is 70 sec measured on the system clock corresponds to a film of 110 nm ($\approx$ 1.5 nm/s). Typically one would like to 'pre-sputter' for a minute or two to make sure any contaminants have been cleaned off the target's surface.
- Strike the plasma by turning the selected gun to on using the power supply.
- Open and close the gun shutter at the appropriate times based on your desired film thickness. Once the deposition clock on the power supply reaches zero, the gun will automatically ramp the power back down to zero and the power can them be shut off.

At the end of the deposition, the gas is turned off and pumped out of the chamber by the cryopump. The wafer can them be loaded back into the loadlock and removed from the system.

A.2.2 Photolithography

Photolithography is the process of imprinting a pattern on a substrate, based on a template design. In our context photolithography will correspond to shaping 2D layers of metal. Broadly speaking there are two processes we typically use to pattern superconducting metals, namely etching and liftoff. The major difference is the order in which the resist layer coated on the wafer. In an etch process, the metal is deposited first and the resist is patterned on top. The opposite is done in a liftoff process where a resist layer is deposited and patterned before metal is evaporated. Both can accomplish the same thing in theory though in practice one approach might be better suited for a particular process.

Once a metal layer is deposited on the wafer the next step is to pattern the ground plane and resonator structures with photolithography. This is accomplished at the Cornell Nanoscale Facility using an ASML 300C deep UV photo stepper. Before the image can be printed on the substrate, a photosensitive polymer must be put on the surface, exposed and developed. These are the standard photolithography steps used throughout the semiconductor industry and there are a large number of specific processes that can be realized in general photolithography.

- Spin DS-K101 (Brewer Science) @ 5000 rpm with a 10000 rpm/s ramp for 60 sec. This layer functions as a anti-reflecting coating (ARC) which keeps UV light from reflecting off the surface causing standingwave patterns and double exposing the resist. When coated with the right thickness the ARC caused destructive interference of the incident light inside it's layer.
- Bake the ARC at 185 C for 90 sec.
- Spin UV©-210-0.6 (Electronic Materials) @ 3000 rpm with an 8000 rpm/s ramp for 60 sec.
- Bake the resist @ 135 C for 60 sec.
- Expose the wafer (Ideally wait a minute or two for water to diffuse into the resist to complete the reaction.)
- Bake the resist @ 135 C for 90 sec. This post exposure bake will harden the rearrangement of the polymers.
- Develop the resist in MIF-726. I typically use a 90 sec, double puddle program on one of the Hamitech automated developers. Sometimes the pattern you're developing may need a little more time, but modern resist are typically very resilient to over developing.

In our case we'll be using a positive tone resist that will dissolve away in areas exposed with light from the stepper. The first step in this process coats the wafer in an anti-reflective coating (ARC). This keeps UV light from reflecting off the surface and double exposing the resist and distorting lithographic the lithographic pattern. These layers function by using light absorbing materials and, when coated in the right thickness, forming destructive interference patterns in inside the ARC layer. In our case we used DS-K101 (Brewer Science) spun at 5000 rpm with a 10000 rpm/s ramp rate to accomplish this task. After coating the wafer is baked at 185 C for 90 sec. This leaves a layer of ARC nominally 70 nm thick. Once the ARC layer is baked in place, photoresist is coated on the wafer in the same spinning process as the ARC. The photoresist is a suspension of photosensitive polymers that change chemical properties when exposed to light at a certain wavelength. For all the devices reported in this paper a deep UV resist UV$^{©}$-210-0.6 (Electronic Materials).

A.2.3 Electron beam lithography

At Syracuse, we are lucky to be located close to Cornell's Nanoscale Facility. It houses one of the most advanced electron beam lithography tools available to academic researchers. Over the years, our group has made extensive use of these tools manufactured by JEOL in Japan. These systems use 10 keV beams of electrons to write sub 10 nm features. Here I'll describe our process of patterning Josephson Junctions, our most critical circuit element, and other superconducting devices using this equipment. The Josephson Junction is formed by a small insulating barrier in an otherwise continuous superconductor. These junctions can be formed in other ways such as SC-normal metal-SC barriers and even tight constrictions implanted in a continuous piece of superconductor. The qubit inductance is formed by the junction. Critically, this inductance is nonlinear which gives the qubit it's anharmonic level spacing. Without this nonlinearity, the superconducting qubit would not have distinguishable energy eigen states thus precluding a two-level system. There would only be an thermal distribution of states through out the energy levels all with equal spacing.

The entire electron beam patterning step is critical for producing qubits. To reach an acceptable parameter regime for making qubits, we need to have the ability to write 100 nm lines. These form the superconducting electrodes on either side of a Josephson Junction.

In general, e-beam lithography is typically more complicated to execute and reproduce than standard optical lithography. Patterns we would like to imprint in the e-beam resist must first be converted from plutonic, solid shapes into a grid of point exposures in a process called fracturing. The shapes are essentially turned into a large number of point exposures where the electron beam, which is always on while exposing, moves to a given coordinates and waits for an amount of time called a 'dwell' time. The dose received by the resist at the point is directly proportional to this dwell time. To accomplish fracturing, our group uses a program called *LayoutBeamer* from GenISys-GmbH to convert design files into files the e-beam tools can understand.

Another layer of complexity appears when large shapes need to be exposed close to each other. Due to the particle nature of the electron beam exposure, areas designed to experience zero electron dose will still be slightly exposed due to forward and back scattering electrons in the resist. These effect can depend on resist chemistry, substrate and beam current/accelerating voltage. To help correct this, we use a process called proximity correction to scale the electron dose of a small region based on its proximity to near by exposed regions. This is accomplished by a Monte Carlo simulation of electron scattering events. These simulations are produced using a program called *Sceleton* which is also commercially avaliable from GenISys-GmbH. The program takes into account material properties, accelerating voltage, etc... to produce a homogeneous effective dose across the pattern and a minimal stray dose to the rest of the resist. I will detail how to use this program below.

A.2.3.1 Substrate preparation

The process begins in a similar fashion to traditional photolithography. Except in the e-beam case we coat the wafer in an electron sensitive polymer. These polymers can function as resist in two ways. In the positive resist case, the high energy electrons break the backbone chain of the molecule, increasing it's sensitivity to solvents. In the negative case, the electrons cross link the polymers causing the opposite effect, increasing their resistance to chemical solvents. For all but one of the samples in this thesis, a multi layer stack of positive resist polymers was used.

- Ash the wafer in a light oxygen plasma to clean the surface of any resist residues that might be left from a previous round of lithography. 2-3 minutes @ 100 Watts in a pure O^2 plasma.
- spin Methyl Methacrylate (MMA), in %11 Ethyl Lactate MicroChem© at 2300 rpms, 1000 rpm/s ramp to form a 600 nm thick layer
- bake the wafer at 170 C for 10 minutes
- spin Poly Methyl Methacrylate (PMMA), in %2 Anisole MicroChem© at 2500 rpms, 1000 rpm/s ramp to form a 70 nm thick layer
- bake the wafer at 170 C for 10 minutes

An additional complication arises we the process requires using an insulating substrate such as Sapphire. This was not necessary for any of the devices in this thesis it is the substrate of choice in other groups and for 3D qubits [93]. With these substrates, electrons incident on the wafer have nowhere to go and charge begins to build up inside the substrate and resist. This causes distortions in the pattern and overlay errors when the stage has to move while stitching larger shapes together. To combat this, a conducting layer is placed on top of the resist stack to serve as a charge dispersion layer. It can be spun on with a conducting polymer called *ESPACER* though this approach tends to yield inconsistent results most likely due to anisotropy in the spacer coating. In our group, we prefer to thermally evaporate conducting metals, typically 10nm of aluminum, in a UHV chamber just before exposure. This thin metal layer is essentially transparent to the high energy electrons but allows a path to ground so that charge doesn't build up.

A.2.3.2 File preparation and proximity correction

The path from drawing to exposure in an electron bean process can be a long and convoluted one. There are large variety of systems which can function as e-beam writers. This typically means a plethora of different proprietary programs and file formats. Fortunately, the electron beam systems at Cornell are among the best in the world and relatively easy to use.

Preparing files for the JEOL 9500 ebeam writer involves three major step: drawing the pattern, fracturing the pattern and compiling the job into a magazine file the tool can understand. your pattern can be drawn with any of your favorite layout programs such as *K-Layout*. When shooting aligned exposures, it's usually a good idea to draw one, large box around everything in your pattern. It should be a square and centered on the center of the die you want to shoot. This is called a bounding box and holds the center of the pattern to the same location throughout the fracturing process. It is typical for your pattern to not be completely symmetric an would be shifted by some offset when the pattern in rejustified based on its minimum extent.

With your pattern drawn and surrounded by a bounding box, you are now ready to fracture your pattern. This process will turn your drawing into the electron beam 'spots' alluded to earlier. At Syracuse and Cornell we use *Layout-Beamer* for this part of the process. The CNF has other commandline tools available for simple patterns, but I will only talk about fracturing with *Layout-Beamer*.

Bibliography

[1] http://quantum.bbn.com/tools/aps.

[2] Jay M. Gambetta, unpublished.

[3] Mit thesis template. http://web.mit.edu/thesis/tex/. Accessed: 2014-11-10.

[4] A. Aassime, G. Johansson, G. Wendin, R. Schoelkopf, and P. Delsing. Radio-frequency single-electron transistor as readout device for qubits: Charge sensitivity and backaction. *Phys. Rev. Lett.*, 86:3376–3379, Apr 2001.

[5] Vinay Ambegaokar and Alexis Baratoff. Tunneling between superconductors. *Phys. Rev. Lett.*, 10:486–489, Jun 1963.

[6] S. M. Anton, J. S. Birenbaum, S. R. O'Kelley, V. Bolkhovsky, D. A. Braje, G. Fitch, M. Neeley, G. C. Hilton, H.-M. Cho, K. D. Irwin, F. C. Wellstood, W. D. Oliver, A. Shnirman, and John Clarke. Magnetic flux noise in dc squids: Temperature and geometry dependence. *Phys. Rev. Lett.*, 110:147002, Apr 2013.

[7] J. Bardeen, L. N. Cooper, and J. R. Schrieffer. Theory of superconductivity. *Phys. Rev.*, 108:1175–1204, Dec 1957.

[8] R. Barends, J. Kelly, A. Megrant, A. Veitia, D. Sank, E. Jeffrey, T. C. White, J. Mutus, A. G. Fowler, B. Campbell, Y. Chen, Z. Chen, B. Chiaro, A. Dunsworth, C. Neill, P. O'Malley, P. Roushan, A. Vainsencher, J. Wenner, A. N. Korotkov, A. N. Cleland, and John M. Martinis. Superconducting quantum circuits at the surface code threshold for fault tolerance. *Nature*, 508(7497):500–503, apr 2014.

[9] R. Barends, J. Wenner, M. Lenander, Y. Chen, R. C. Bialczak, J. Kelly, E. Lucero, P. OâĂŹMalley, M. Mariantoni, D. Sank, H. Wang, T. C. White, Y. Yin, J. Zhao, A. N. Cleland, John M. Martinis, and J. J. A. Baselmans. Minimizing quasiparticle generation from stray infrared light in superconducting quantum circuits. *Applied Physics Letters*, 99(11):–, 2011.

[10] Félix Beaudoin, Marcus P. da Silva, Zachary Dutton, and Alexandre Blais. First-order sidebands in circuit qed using qubit frequency modulation. *Phys. Rev. A*, 86:022305, Aug 2012.

[11] N. Bergeal, F. Schackert, M. Metcalfe, R. Vijay, V. E. Manucharyan, L. Frunzio, D. E. Prober, R. J. Schoelkopf, S. M. Girvin, and M. H. Devoret. Phase-preserving amplification near the quantum limit with a josephson ring modulator. *Nature*, 465(7294):64–68, May 2010.

[12] R. C. Bialczak, M. Ansmann, M. Hofheinz, E. Lucero, M. Neeley, A. D. O/'Connell, D. Sank, H. Wang, J. Wenner, M. Steffen, A. N. Cleland, and J. M. Martinis. Quantum process tomography of a universal entangling gate implemented with josephson phase qubits. *Nat Phys*, 6(6):409–413, June 2010.

[13] Radoslaw C. Bialczak, R. McDermott, M. Ansmann, M. Hofheinz, N. Katz, Erik Lucero, Matthew Neeley, A. D. O'Connell, H. Wang, A. N. Cleland, and John M. Martinis. $1/f$ flux noise in josephson phase qubits. *Phys. Rev. Lett.*, 99:187006, Nov 2007.

[14] Lev Bishop. Lev bishop's latex source code. http://www.levbishop.org/thesis/source/. Accessed: 2014-11-10.

[15] Alexandre Blais, Jay Gambetta, A. Wallraff, D. I. Schuster, S. M. Girvin, M. H. Devoret, and R. J. Schoelkopf. Quantum-information processing with circuit quantum electrodynamics. *Phys. Rev. A*, 75:032329, Mar 2007.

[16] Alexandre Blais, Ren-Shou Huang, Andreas Wallraff, S. M. Girvin, and R. J. Schoelkopf. Cavity quantum electrodynamics for superconducting electrical circuits: An architecture for quantum computation. *Phys. Rev. A*, 69:062320, Jun 2004.

[17] D.F. Bogorin, D.T. McClure, M. Ware, and B.L.T. Plourde. Copper waveguide cavities with reduced surface loss for coupling to superconducting qubits. *Applied Superconductivity, IEEE Transactions on*, 24(4):1–7, Aug 2014.

[18] V Bouchiat, D Vion, P Joyez, D Esteve, and M H Devoret. Quantum coherence with a single cooper pair. *Physica Scripta*, 1998(T76):165, 1998.

[19] Darren K Brock. Rsfq technology: Circuits and systems. *International journal of high speed electronics and systems*, 11(01):307–362, 2001.

[20] M. Brune, E. Hagley, J. Dreyer, X. Maître, A. Maali, C. Wunderlich, J. M. Raimond, and S. Haroche. Observing the progressive decoherence of the "meter" in a quantum measurement. *Phys. Rev. Lett.*, 77:4887–4890, Dec 1996.

[21] G. Catelani, S. E. Nigg, S. M. Girvin, R. J. Schoelkopf, and L. I. Glazman. Decoherence of superconducting qubits caused by quasiparticle tunneling. *Phys. Rev. B*, 86:184514, Nov 2012.

[22] Andrew M. Childs and Isaac L. Chuang. Universal quantum computation with two-level trapped ions. *Phys. Rev. A*, 63:012306, Dec 2000.

[23] I. Chiorescu, P. Bertet, K. Semba, Y. Nakamura, C. Harmans, and JE Mooij. Coherent dynamics of a flux qubit coupled to a harmonic oscillator. *Nature*, 431(7005):159–162, 2004.

[24] I. Chiorescu, Y. Nakamura, C. J. P. M. Harmans, and J. E. Mooij. Coherent quantum dynamics of a superconducting flux qubit. *Science*, 299(5614):1869–1871, 2003.

[25] J. Chow, J. Gambetta, L. Tornberg, Jens Koch, Lev Bishop, A. Houck, B. Johnson, L. Frunzio, S. Girvin, and R. Schoelkopf. Randomized benchmarking and process tomography for gate errors in a solid-state qubit. *Phys. Rev. Lett.*, 102:090502, Mar 2009.

[26] Jerry Chow, Jay Gambetta, A. Córcoles, Seth Merkel, John Smolin, Chad Rigetti, S. Poletto, George Keefe, Mary Rothwell, J. Rozen, Mark Ketchen, and M. Steffen. Universal quantum gate set approaching fault-tolerant thresholds with superconducting qubits. *Phys. Rev. Lett.*, 109:060501, Aug 2012.

[27] Jerry M. Chow, A. D. Córcoles, Jay M. Gambetta, Chad Rigetti, B. R. Johnson, John A. Smolin, J. R. Rozen, George A. Keefe, Mary B. Rothwell, Mark B. Ketchen, and M. Steffen. Simple all-microwave entangling gate for fixed-frequency superconducting qubits. *Phys. Rev. Lett.*, 107:080502, Aug 2011.

[28] Jerry M. Chow, Jay M. Gambetta, Andrew W. Cross, Seth T. Merkel, Chad Rigetti, and M. Steffen. Microwave-activated conditional-phase gate for superconducting qubits. *New Journal of Physics*, 15(11):115012, 2013.

[29] Jerry M. Chow, Jay M. Gambetta, Easwar Magesan, David W. Abraham, Andrew W. Cross, B R Johnson, Nicholas A. Masluk, Colm A. Ryan, John A. Smolin, Srikanth J. Srinivasan, and M Steffen. Implementing a strand of a scalable fault-tolerant quantum computing fabric. *Nat Commun*, 5:4015(40415), June 2014.

[30] J. I. Cirac and P. Zoller. Quantum computations with cold trapped ions. *Phys. Rev. Lett.*, 74:4091–4094, May 1995.

[31] John Clarke and Frank K. Wilhelm. Superconducting quantum bits. *Nature*, 453(7198):1031–1042, June 2008.

[32] J. N. L. Connor, T. Uzer, R. A. Marcus, and A. D. Smith. Eigenvalues of the schrÃűdinger equation for a periodic potential with nonperiodic boundary conditions: A uniform semiclassical analysis. *The Journal of Chemical Physics*, 80(10), 1984.

[33] A. D. Córcoles, Jay M. Gambetta, Jerry M. Chow, John A. Smolin, Matthew Ware, Joel Strand, B. L. T. Plourde, and M. Steffen. Process verification of two-qubit quantum gates by randomized benchmarking. *Phys. Rev. A*, 87:030301, Mar 2013.

[34] A. D. Córcoles, Easwar Magesan, Srikanth J. Srinivasan, Andrew W. Cross, M. Steffen, Jay M. Gambetta, and Jerry M. Chow. Detecting arbitrary quantum errors via stabilizer measurements on a sublattice of the surface code. *Preprint at http://arxiv.org/abs/1410.6419*, 2014.

[35] Antonio D. Córcoles, Jerry M. Chow, Jay M. Gambetta, Chad Rigetti, J. R. Rozen, George A. Keefe, Mary Beth Rothwell, Mark B. Ketchen, and M. Steffen. Protecting superconducting qubits from radiation. *Appl. Phys. Lett.*, 99(18):181906, 2011.

[36] Samuel Deleglise, Igor Dotsenko, Clement Sayrin, Julien Bernu, Michel Brune, Jean-Michel Raimond, and Serge Haroche. Reconstruction of non-classical cavity field states with snapshots of their decoherence. *Nature*, 455(7212):510–514, September 2008.

[37] Michel H Devoret. Quantum fluctuations in electrical circuits. *Les Houches, Session LXIII*, 1995.

[38] Ted Van Duzer and Charles W. Turner. *Principles of Superconductive Devices and Circuits, (Second Ed.)*. Prentice Hall PTR, Upper Saddle River, NJ, USA, 1999.

[39] A. Fedorov, L. Steffen, M. Baur, M. P. da Silva, and A. Wallraff. Implementation of a toffoli gate with superconducting circuits. *Nature*, 481(7380):170–172, January 2012.

[40] Richard Phillips Feyman. *QED: The strange theory of light and matter*. Universities Press, 1985.

[41] R. P. Feynman. Space-time approach to quantum electrodynamics. *Phys. Rev.*, 76:769–789, Sep 1949.

[42] Austin G. Fowler, Matteo Mariantoni, John M. Martinis, and Andrew N. Cleland. Surface codes: Towards practical large-scale quantum computation. *Phys. Rev. A*, 86:032324, Sep 2012.

[43] A. Fragner, M. Göppl, J. M. Fink, M. Baur, R. Bianchetti, P. J. Leek, A. Blais, and A. Wallraff. Resolving vacuum fluctuations in an electrical circuit by measuring the lamb shift. *Science*, 322(5906):1357–1360, 2008.

[44] Jay Gambetta, WA Braff, A Wallraff, SM Girvin, and RJ Schoelkopf. Protocols for optimal readout of qubits using a continuous quantum nondemolition measurement. *Physical Review A*, 76(1):012325, 2007.

[45] Jay M. Gambetta, A. D. Córcoles, S. T. Merkel, B. R. Johnson, John A. Smolin, Jerry M. Chow, Colm A. Ryan, Chad Rigetti, S. Poletto, Thomas A. Ohki, Mark B. Ketchen, and M. Steffen. Characterization of addressability by simultaneous randomized benchmarking. *Phys. Rev. Lett.*, 109:240504, Dec 2012.

[46] K. Geerlings, Z. Leghtas, I. M. Pop, S. Shankar, L. Frunzio, R. J. Schoelkopf, M. Mirrahimi, and M. H. Devoret. Demonstrating a driven reset protocol for a superconducting qubit. *Phys. Rev. Lett.*, 110:120501, Mar 2013.

[47] Daniel Gottesman. *Stabilizer codes and quantum error correction,âĂİ 1997, Caltech Ph. D.* PhD thesis, dissertation, eprint: quant-ph/9705052, 1997.

[48] Lov K. Grover. A fast quantum mechanical algorithm for database search. *Preprint at http://arxiv.org/abs/quant-ph/9605043v3*, 1996.

[49] H. Haffner, W. Hansel, C. F. Roos, J. Benhelm, D. Chek-al kar, M. Chwalla, T. Korber, U. D. Rapol, M. Riebe, P. O. Schmidt, C. Becher, O. Guhne, W. Dur, and R. Blatt. Scalable multiparticle entanglement of trapped ions. *Nature*, 438(7068):643–646, Dec 2005.

[50] E. L. Hahn. Spin echoes. *Phys. Rev.*, 80:580–594, Nov 1950.

[51] S. Haroche, J. Dalibard, J.M. Raimond, and J. Zinn-Justin. Fundamental systems in quantum optics. *Les Houches Summar School Session*, 53, 1992.

[52] Serge Haroche and Jean-Michel Raimond. *Exploring the quantum: atoms, cavities, and photons (oxford graduate texts).* Oxford University Press, USA, 2006.

[53] Quentin P. Herr, Anna Y. Herr, Oliver T. Oberg, and Alexander G. Ioannidis. Ultra-low-power superconductor logic. *Journal of Applied Physics*, 109(10):–, 2011.

[54] Max Hofheinz, H. Wang, M. Ansmann, Radoslaw C. Bialczak, Erik Lucero, M. Neeley, A. D. O'Connell, D. Sank, J. Wenner, John M. Martinis, and A. N. Cleland. Synthesizing arbitrary quantum states in a superconducting resonator. *Nature*, 459(7246):546–549, May 2009.

[55] D. Hover, Y.-F. Chen, G. J. Ribeill, S. Zhu, S. Sendelbach, and R. McDermott. Superconducting low-inductance undulatory galvanometer microwave amplifier. *Applied Physics Letters*, 100(6):–, 2012.

[56] Edwin T Jaynes and Frederick W Cummings. Comparison of quantum and semiclassical radiation theories with application to the beam maser. *Proceedings of the IEEE*, 51(1):89–109, 1963.

[57] Evan Jeffrey, Daniel Sank, J. Y. Mutus, T. C. White, J. Kelly, R. Barends, Y. Chen, Z. Chen, B. Chiaro, A. Dunsworth, A. Megrant, P. J. J. O'Malley, C. Neill, P. Roushan, A. Vainsencher, J. Wenner, A. N. Cleland, and John M. Martinis. Fast accurate state measurement with superconducting qubits. *Phys. Rev. Lett.*, 112:190504, May 2014.

[58] J.R. Johansson, P.D. Nation, and Franco Nori. Qutip 2: A python framework for the dynamics of open quantum systems. *Computer Physics Communications*, 184(4):1234 – 1240, 2013.

[59] Blake R. Johnson and Jay M. Gambetta. private communication 2014.

[60] B. D. Josephson. Possible new effects in superconductive tunnelling. *Physics Letters*, 1:251–253, July 1962.

[61] J. Kelly, R. Barends, A. G. Fowler, A. Megrant, E. Jeffrey, T. C. White, D. Sank, J. Y. Mutus, B. Campbell, Yu Chen, Z. Chen, B. Chiaro, A. Dunsworth, I.-C. Hoi, C. Neill, P. J. J. O'Malley, C. Quintana, P. Roushan, A. ainsencher, J. Wenner, A. N. Cleland, and John M. Matinis. State preservation by repetitve error detection in a superconducting quantum circuit. *Preprint at http://arxiv.org/abs/1411.7403*, 2014.

[62] E. Knill, D. Leibfried, R. Reichle, J. Britton, R. B. Blakestad, J. D. Jost, C. Langer, R. Ozeri, S. Seidelin, and D. J. Wineland. Randomized benchmarking of quantum gates. *Phys. Rev. A*, 77:012307, Jan 2008.

[63] Jens Koch, Terri M. Yu, Jay Gambetta, A. A. Houck, D. I. Schuster, J. Majer, Alexandre Blais, M. H. Devoret, S. M. Girvin, and R. J. Schoelkopf. Charge-insensitive qubit design derived from the cooper pair box. *Phys. Rev. A*, 76:042319, Oct 2007.

[64] Alexander N. Korotkov. Continuous quantum measurement of a double dot. *Phys. Rev. B*, 60:5737–5742, Aug 1999.

[65] Kenneth S Krane. Modern physics. *Modern Physics, 2nd Edition, by Kenneth S. Krane, pp. 608. ISBN 0-471-82872-6. Wiley-VCH, August 1995.*, 1, 1995.

[66] P. Leek, S. Filipp, P. Maurer, M. Baur, R. Bianchetti, J. Fink, M. Göppl, L. Steffen, and A. Wallraff. Using sideband transitions for two-qubit operations in superconducting circuits. *Phys. Rev. B*, 79:180511, May 2009.

[67] AJ Leggett. Chance and matter, proceedings, 1986 les houches summer school. 1987.

[68] K. Lehnert, K. Bladh, L. Spietz, D. Gunnarsson, D. Schuster, P. Delsing, and R. Schoelkopf. Measurement of the excited-state lifetime of a microelectronic circuit. *Phys. Rev. Lett.*, 90:027002, Jan 2003.

[69] D. Leibfried, E. Knill, S. Seidelin, J. Britton, R. B. Blakestad, J. Chiaverini, D. B. Hume, W. M. Itano, J. D. Jost, C. Langer, R. Ozeri, R. Reichle, and D. J. Wineland. Creation of a six-atom /'schrodinger cat/' state. *Nature*, 438(7068):639–642, Dec 2005.

[70] K. K. Likharev. Superconducting weak links. *Rev. Mod. Phys.*, 51:101–159, Jan 1979.

[71] Easwar Magesan, J. M. Gambetta, and Joseph Emerson. Scalable and robust randomized benchmarking of quantum processes. *Phys. Rev. Lett.*, 106:180504, May 2011.

[72] Easwar Magesan, Jay M. Gambetta, A. D. Córcoles, and Jerry M. Chow. Machine learning for descriminating quantum measurement trajectories and improving readout. *Preprint at http://arxiv.org/abs/1411.4994*, 2014.

[73] Easwar Magesan, Jay M. Gambetta, B. R. Johnson, Colm A. Ryan, Jerry M. Chow, Seth T. Merkel, Marcus P. da Silva, George A. Keefe, Mary B. Rothwell, Thomas A. Ohki, Mark B. Ketchen, and M. Steffen. Efficient measurement of quantum gate error by interleaved randomized benchmarking. *Phys. Rev. Lett.*, 109:080505, Aug 2012.

[74] J. Majer, JM Chow, JM Gambetta, J. Koch, BR Johnson, JA Schreier, L. Frunzio, DI Schuster, AA Houck, A. Wallraff, et al. Coupling superconducting qubits via a cavity bus. *Nature*, 449(7161):443–447, 2007.

[75] John M. Martinis, Michel H. Devoret, and John Clarke. Energy-level quantization in the zero-voltage state of a current-biased josephson junction. *Phys. Rev. Lett.*, 55:1543–1546, Oct 1985.

[76] John M. Martinis, Michel H. Devoret, and John Clarke. Energy-level quantization in the zero-voltage state of a current-biased josephson junction. *Phys. Rev. Lett.*, 55:1543–1546, Oct 1985.

[77] John M. Martinis and Michael R. Geller. Fast adiabatic qubit gates using only σ_z control. *Phys. Rev. A*, 90:022307, Aug 2014.

[78] John M. Martinis, S. Nam, J. Aumentado, and C. Urbina. Rabi oscillations in a large josephson-junction qubit. *Phys. Rev. Lett.*, 89:117901, Aug 2002.

[79] Benjamin A. Mazin. *Microwave kinetic inductance detectors.* PhD thesis, Caltech, 2005.

[80] R. McDermott. Materials origins of decoherence in superconducting qubits. *Applied Superconductivity, IEEE Transactions on*, 19(1):2–13, Feb 2009.

[81] R. Meservey and P. M. Tedrow. Measurements of the kinetic inductance of superconducting linear structures. *Journal of Applied Physics*, 40(5), 1969.

[82] C. Monroe, D. M. Meekhof, B. E. King, W. M. Itano, and D. J. Wineland. Demonstration of a fundamental quantum logic gate. *Phys. Rev. Lett.*, 75:4714–4717, Dec 1995.

[83] C. Monroe, D. M. Meekhof, B. E. King, and D. J. Wineland. A schrödinger cat superposition state of an atom. *Science*, 272(5265):1131–1136, 1996.

[84] J. E. Mooij, T. P. Orlando, L. Levitov, Lin Tian, Caspar H. van der Wal, and Seth Lloyd. Josephson persistent-current qubit. *Science*, 285(5430):1036–1039, 1999.

[85] F. Motzoi, J. M. Gambetta, P. Rebentrost, and F. K. Wilhelm. Simple pulses for elimination of leakage in weakly nonlinear qubits. *Phys. Rev. Lett.*, 103:110501, Sep 2009.

[86] K. W. Murch, S. J. Weber, C. Macklin, and I. Siddiqi. Observing single quantum trajectories of a superconducting quantum bit. *Nature*, 502(7470):211–214, October 2013.

[87] KW Murch, SJ Weber, EM Levenson-Falk, R Vijay, and I Siddiqi. 1/f noise of josephson-junction-embedded microwave resonators at single photon energies and millikelvin temperatures. *Applied Physics Letters*, 100(14):142601, 2012.

[88] Y. Nakamura, Yu. A. Pashkin, and J. S. Tsai. Coherent control of macroscopic quantum states in a single-cooper-pair box. *Nature*, 398(6730):786–788, April 1999.

[89] Michael A Nielsen and Isaac L Chuang. *Quantum computation and quantum information.* Cambridge university press, 2010.

[90] I. Nsanzineza and B. L. T. Plourde. Trapping a single vortex and reducing quasiparticles in a superconducting resonator. *Phys. Rev. Lett.*, 113:117002, Sep 2014.

[91] A. D. O'Connell, M. Hofheinz, M. Ansmann, Radoslaw C. Bialczak, M. Lenander, Erik Lucero, M. Neeley, D. Sank, H. Wang, M. Weides, J. Wenner, John M. Martinis, and A. N. Cleland. Quantum ground state and single-phonon control of a mechanical resonator. *Nature*, 464(7289):697–703, April 2010.

[92] C. Ospelkaus, U. Warring, Y. Colombe, K. R. Brown, J. M. Amini, D. Leibfried, and D. J. Wineland. Microwave quantum logic gates for trapped ions. *Nature*, 476(7359):181–184, August 2011.

[93] Hanhee Paik, D. I. Schuster, Lev S. Bishop, G. Kirchmair, G. Catelani, A. P. Sears, B. R. Johnson, M. J. Reagor, L. Frunzio, L. I. Glazman, S. M. Girvin, M. H. Devoret, and R. J. Schoelkopf. Observation of high coherence in josephson junction qubits measured in a three-dimensional circuit qed architecture. *Phys. Rev. Lett.*, 107:240501, Dec 2011.

[94] Ioan M. Pop, Kurtis Geerlings, Gianluigi Catelani, Robert J. Schoelkopf, Leonid I. Glazman, and Michel H. Devoret. Coherent suppression of electromagnetic dissipation due to superconducting quasiparticles. *Nature*, 508(7496):369–372, April 2014.

[95] John Preskill. Quantum computing and the entanglement frontier. *Preprint at http://arxiv.org/abs/1203.5813v3*, 2012.

[96] Norman Ramsey. A molecular beam resonance method with separated oscillating fields. *Phys. Rev.*, 78:695–699, Jun 1950.

[97] Robert Raussendorf and Jim Harrington. Fault-tolerant quantum computation with high threshold in two dimensions. *Phys. Rev. Lett.*, 98:190504, May 2007.

[98] M. D. Reed, L. DiCarlo, B. R. Johnson, L. Sun, D. I. Schuster, L. Frunzio, and R. J. Schoelkopf. High-fidelity readout in circuit quantum electrodynamics using the jaynes-cummings nonlinearity. *Phys. Rev. Lett.*, 105:173601, Oct 2010.

[99] Chad Rigetti, Alexandre Blais, and Michel Devoret. Protocol for universal gates in optimally biased superconducting qubits. *Phys. Rev. Lett.*, 94:240502, Jun 2005.

[100] Chad Rigetti and Michel Devoret. Fully microwave-tunable universal gates in superconducting qubits with linear couplings and fixed transition frequencies. *Phys. Rev. B*, 81:134507, Apr 2010.

[101] D Ristè, CC Bultink, MJ Tiggelman, RN Schouten, KW Lehnert, and L DiCarlo. Millisecond charge-parity fluctuations and induced decoherence in a superconducting transmon qubit. *Nature communications*, 4:1913, 2013.

[102] D. Ristè, S. Poletto, M.-Z. Huang, A. Bruno, V. Vesterinen, Saira O.-P., and L. DiCarlo. Detecting bit-flip errors in a logical qubit using stabilizer measurements. *Preprint at http://arxiv.org/abs/1411.5542*, 2014.

[103] D. Ristè, J. van Leeuwen, H.-S. Ku, K. Lehnert, and L. DiCarlo. Initialization by measurement of a superconducting quantum bit circuit. *Phys. Rev. Lett.*, 109:050507, Aug 2012.

[104] R. L. Rivest, A. Shamir, and L. Adleman. A method for obtaining digital signatures and public-key cryptosystems. *Commun. ACM*, 21(2):120–126, February 1978.

[105] C A Ryan, M Laforest, and R Laflamme. Randomized benchmarking of single- and multi-qubit control in liquid-state nmr quantum information processing. *New Journal of Physics*, 11(1):013034, 2009.

[106] Colm A. Ryan. Frequency modulating entangling gates. APS March Meeting 2014, Denver, CO, 2014.

[107] Colm A Ryan, Blake R Johnson, Jay M Gambetta, Jerry M Chow, Marcus da Silva, Oliver E Dial, and Thomas A Ohki. Tomography via correlation of noisy measurement records. *Preprint at http://arxiv.org/abs/1310.6448*, 2013.

[108] J. A. Schreier, A. A. Houck, Jens Koch, D. I. Schuster, B. R. Johnson, J. M. Chow, J. M. Gambetta, J. Majer, L. Frunzio, M. H. Devoret, S. M. Girvin, and R. J. Schoelkopf. Suppressing charge noise decoherence in superconducting charge qubits. *Phys. Rev. B*, 77:180502, May 2008.

[109] D. Schuster, A. Wallraff, A. Blais, L. Frunzio, R.-S. Huang, J. Majer, S. Girvin, and R. Schoelkopf. ac stark shift and dephasing of a superconducting qubit strongly coupled to a cavity field. *Phys. Rev. Lett.*, 94:123602, Mar 2005.

[110] D. I. Schuster, A. A. Houck, J. A. Schreier, A. Wallraff, J. M. Gambetta, A. Blais, L. Frunzio, J. Majer, B. Johnson, M. H. Devoret, S. M. Girvin, and R. J. Schoelkopf. Resolving photon number states in a superconducting circuit. *Nature*, 445(7127):515–518, February 2007.

[111] D.I. Schuter. *Cavity Quantum Electrodynamics*. PhD thesis, Yale, 2007.

[112] S. Sendelbach, D. Hover, A. Kittel, M. Mück, John M. Martinis, and R. McDermott. Magnetism in squids at millikelvin temperatures. *Phys. Rev. Lett.*, 100:227006, Jun 2008.

[113] S. Sendelbach, D. Hover, M. Mück, and R. McDermott. Complex inductance, excess noise, and surface magnetism in dc squids. *Phys. Rev. Lett.*, 103:117001, Sep 2009.

[114] Seung Woo Shin, Graeme Smith, John A. Smolin, and Umesh Vazirani. How "quantum" is the d-wave machine? *Preprint at http://arxiv.org/abs/1404.7087*, 2014.

[115] P. Shor. Polynomial-time algorithms for prime factorization and discrete logarithms on a quantum computer. *SIAM Journal on Computing*, 26(5):1484–1509, 1997.

[116] I. Siddiqi, R. Vijay, F. Pierre, C. M. Wilson, M. Metcalfe, C. Rigetti, L. Frunzio, and M. H. Devoret. Rf-driven josephson bifurcation amplifier for quantum measurement. *Phys. Rev. Lett.*, 93:207002, Nov 2004.

[117] J. D. Strand, Matthew Ware, Félix Beaudoin, T. A. Ohki, B. R. Johnson, Alexandre Blais, and B. L. T. Plourde. First-order sideband transitions with flux-driven asymmetric transmon qubits. *Phys. Rev. B*, 87:220505, Jun 2013.

[118] Michael Tinkham. *Introduction to superconductivity.* Courier Dover Publications, 2012.

[119] Sabine Van Huffel. Enhanced resolution based on minimum variance estimation and exponential data modeling. *Signal Process.*, 33(3):333–355, September 1993.

[120] Lieven M. K. Vandersypen, Matthias Steffen, Gregory Breyta, Costantino S. Yannoni, Mark H. Sherwood, and Isaac L. Chuang. Experimental realization of shor's quantum factoring algorithm using nuclear magnetic resonance. *Nature*, 414(6866):883–887, December 2001.

[121] R. Vijay, M. H. Devoret, and I. Siddiqi. Invited review article: The josephson bifurcation amplifier. *Review of Scientific Instruments*, 80(11):–, 2009.

[122] Walter Vinci, Tameen Albash, Anurag Mishra, Paul A. Warburton, and Daniel A. Lidar. Distinguishing classical and quantum models for the d-wave device. *Preprint at http://arxiv.org/abs/1403.4228v3*, 2014.

[123] A. Wallraff, D. I. Schuster, A. Blais, J. M. Gambetta, J. Schreier, L. Frunzio, M. H. Devoret, S. M. Girvin, and R. J. Schoelkopf. Sideband transitions and two-tone spectroscopy of a superconducting qubit strongly coupled to an on-chip cavity. *Phys. Rev. Lett.*, 99:050501, Jul 2007.

[124] A. Wallraff, DI Schuster, A. Blais, L. Frunzio, R.S. Huang, J. Majer, S. Kumar, SM Girvin, and RJ Schoelkopf. Strong coupling of a single photon to a superconducting qubit using circuit quantum electrodynamics. *Nature*, 431(7005):162–167, 2004.

[125] Daniel F Walls and Gerard J Milburn. *Quantum optics*. Springer, 2007.

[126] Matthew Ware, Blake R. Johnson, Jay M. Gambetta, Thomas A. Ohki, Jerry M. Chow, and B. L. T. Plourde. manuscript in preparation.

[127] S. J. Weber, A. Chantasri, J. Dressel, A. N. Jordan, K. W. Murch, and I. Siddiqi. Mapping the optimal route between two quantum states. *Nature*, 511(7511):570–573, July 2014.

[128] Frederick C. Wellstood, Cristian Urbina, and John Clarke. LowâĂŘfrequency noise in dc superconducting quantum interference devices below 1 k. *Applied Physics Letters*, 50(12), 1987.

[129] T. Yamamoto, M. Neeley, E. Lucero, R. Bialczak, J. Kelly, M. Lenander, Matteo Mariantoni, A. O'Connell, D. Sank, H. Wang, M. Weides, J. Wenner, Y. Yin, A. Cleland, and John Martinis. Quantum process tomography of two-qubit controlled-z and controlled-not gates using superconducting phase qubits. *Phys. Rev. B*, 82:184515, Nov 2010.

[130] F. Yoshihara, K. Harrabi, A. Niskanen, Y. Nakamura, and J. Tsai. Decoherence of flux qubits due to $1/f$ flux noise. *Phys. Rev. Lett.*, 97:167001, Oct 2006.

[131] F. Yoshihara, K. Harrabi, A. O. Niskanen, Y. Nakamura, and J. S. Tsai. Decoherence of flux qubits due to $1/f$ flux noise. *Phys. Rev. Lett.*, 97:167001, Oct 2006.

[132] Fumiki Yoshihara, Yasunobu Nakamura, Fei Yan, Simon Gustavsson, Jonas Bylander, William D. Oliver, and Jaw-Shen Tsai. Flux qubit noise spectroscopy using rabi oscillations under strong driving conditions. *Phys. Rev. B*, 89:020503, Jan 2014.

[133] J. Q. You and Franco Nori. Atomic physics and quantum optics using superconducting circuits. *Nature*, 474(7353):589–597, June 2011.

Vita

Matthew E. Ware

---

201 Physics Building
Department of Physics
Syracuse University
Syracuse, NY 13244 USA

Voice: (205) 410-8570
Fax: (315) 443-9103
E-mail: meware@syr.edu

ACADEMIC PREPARATION

Syracuse University, Syracuse, New York USA

M.S., Physics **May 2011**

University of Alabama, Tuscaloosa, Alabama USA

B.S., Physics and Applied Mathematics, Summa Cum Laude **May 2009**

HONORS AND AWARDS

University Fellow, Syracuse University **2009 - 2011**

Phi Beta Kappa, University of Alabama **2009**

ACADEMIC EXPERIENCE

Syracuse University, Syracuse, New York USA

Graduate Student **July 2009 - present**
Includes current Ph.D. research, Ph.D. and Masters level coursework

University of Alabama, Tuscaloosa, Alabama USA

Undergraduate Research **Fall 2008 - May 2009**
Thin film deposition for giant magnetoresistance research in the groups of Patrick LeClair and Gary Mankey

Ludwig-Maximilians-Universität, Munich, Germany

DAAD R.I.S.E Intern **May - August 2007**
Lab/Research experience fabricating and measuring pentacene thin film transistors in the group of Bert Nickle

PUBLICATIONS

Daniela F. Bogorin, D. T. McClure, Matthew Ware, and B. L. T. Plourde. ”Copper waveguide cavities with reduced surface loss for coupling to superconducting qubits.” *IEEE Transactions on Applied Superconductivity*, 24(4), 1700207, June 2014.

A. D. Córcoles, Jay M. Gambetta, Jerry M. Chow, John A. Smolin, Matthew Ware, Joel Strand, B. L. T. Plourde, and M. Steffen. ”Process verification of two-qubit quantum gates by randomized benchmarking.” *Phys. Rev. A*, 87:030301, Mar 2013.

J. D. Strand, Matthew Ware, Félix Beaudoin, T. A. Ohki, B. R. Johnson, Alexandre Blais, and B. L. T. Plourde. ”First-order sideband transitions with flux-driven asymmetric transmon qubits.” *Phys. Rev. B*, 87:220505, Jun 2013.

CONFERENCE TALKS/POSTERS

Poster session **March 2014**
Matthew Ware, Blake Johnson, Jay M. Gambetta, Colm Ryan, Thomas Ohki, Jerry Chow, B. L. T. Plourde. Aspen Center for Physics winter conference” Advances in quantum algorithms and computation”. ”Cross-resonance interactions between superconducting qubits with variable detuning”

APS March meeting talk **March 2014**
Matthew Ware, Blake Johnson, Jay M. Gambetta, Colm Ryan, Thomas Ohki, Jerry Chow, B. L. T. Plourde. ”Cross-resonance interactions between superconducting qubits with variable detuning”

14th ISEC conference poster session **July 2013**
14th International Superconducting Electronics Conference Boston, Mass. Matthew Ware, Daniela Bogorin, Britton L. T. Plourde. ”Asymmetric transmons for controllable multi-qubit interactions”

APS March meeting talk **March 2013**
Matthew Ware, Daniela Bogorin, J. D. Strand, B. L. T. Plourde. ”Tuning qubit interactions with asymmetric transmons”

Student conference talk **June 2012**
9th Canadian Student Conference on Quantum Information, and the 2nd AQuA Student Congress on Quantum Information, Institute for Quantum Computing, University of Waterloo, Ontario Canada. ”Material and geometric effects in 3D transmon qubits”

APS March meeting talk **March 2012**
Matthew Ware, M.P. Defeo, J.D. Strand, B. Xiao, B.L.T. Plourde, Stefano Poletto, Chad Rigetti. ”Material and geometric effects in 3D transmon qubits”

PROFESSIONAL EXPERIENCE

Advances in quantum algorithms and computation **March 2014**
Aspen Center for Physics, Aspen Colorado

12th Canadian summer school on quantum information **June 2012**
Institute for Quantum Computing, University of Waterloo, Ontario Canada

TECHNICAL SKILLS

Fabrication experience: 3+ years of user experience at Cornell Universities Nanoscale Science and Technology Facility (CNF) including electron-beam lithography, photolithography, wet/dry etching, thin film deposition, Josephson junction processing, imaging/metrology, device design and layout
Simulation/Design: HFSS, Sonnet, Cadence
Code: C/C++,MATLAB,Python
Measurement: 4+ years of low temperature (< 300mK) microwave measurement. 3+ years experience at (< 30mK)

PHD ADVISOR

Prof. Britton L. T. Plourde, Syracuse University